



2.1 Charge Carrier Transport in Single-Crystal Organic Field-Effect Transistors

Vitaly Podzorov

CONTENTS

2.1.1	Introduction: the Field Effect in Small-Molecule Organic Semiconductors	28
2.1.2	Fabrication of Single-Crystal OFETs.....	30
2.1.3	Charge Transport on the Surface of Organic Single Crystals	38
2.1.3.1	Basic FET Operation.....	38
2.1.3.2	The Multiple Trap-and-Release Model.....	46
2.1.3.3	Anisotropy of the Mobility	48
2.1.3.4	Longitudinal and Hall Conductivity in Rubrene OFETs.....	50
2.1.3.5	Comparison with the Holstein–Peierls Model and Transport Measurements in the Bulk of Organic Crystals.....	54
2.1.3.6	Tuning the Intermolecular Distance.....	55
2.1.3.7	Surface versus Bulk Transport.....	56
2.1.3.8	Photoinduced Processes in Single-Crystal OFETs.....	58
2.1.4	Defects at the Surface of Organic Crystals	59
2.1.4.1	Bulk and Surface Electronic Defects in Organic Crystals	61
2.1.4.2	Density of Defects in Single-Crystal OFETs	63
2.1.4.3	Single-Crystal OFETs as Tools to Study of Surface Defects	64
2.1.5	Conclusion	65
	Acknowledgments.....	67
	References.....	67



2.1.1 INTRODUCTION: THE FIELD EFFECT IN SMALL-MOLECULE ORGANIC SEMICONDUCTORS

Organic semiconductors represent a large class of solids consisting of organic oligomers or polymers. This chapter focuses on crystals of small organic molecules (mostly, polyacenes containing typically 2–10 benzene rings) held together in a solid by van der Waals forces. These small-molecule organic semiconductors, together with polymers, represent the material basis for the rapidly developing field of organic electronics [1–5].

Because of the weak van der Waals bonding, many electronic properties of these materials (e.g., the energy gap between the highest occupied and lowest unoccupied molecular orbitals — HOMO and LUMO, respectively) are determined by the structure of an isolated molecule [6–8]. Weak intermolecular overlap of electronic orbitals results in narrow electronic bands (a typical bandwidth, $W \sim 0.1$ eV, is two orders of magnitude smaller than that in silicon) and a low mobility of carriers ($\mu \sim 1\text{--}10$ cm²/Vs at room temperature) and strong electron-lattice coupling. The anisotropy of the transfer integrals between the adjacent molecules reflects the low symmetry of the molecular packing in *organic molecular crystals* (OMCs). It is believed that the most adequate description of the charge transport in these semiconductors is based on the concept of *small polarons* — the electronic states resulting from interaction of charge with lattice polarization at a length scale comparable to the lattice constant [6,7,9,10].

After several decades of intensive research, our basic understanding of charge transport in small-molecule organic semiconductors remains limited. The complexity of transport phenomena in these systems is due to the polaronic nature of charge carriers and strong interaction of small polarons with defects [6]. An especially challenging task is to develop an adequate model of high-temperature polaronic transport. At room temperature, which is typically comparable to or even higher than the characteristic phonon energies, the lattice vibrations might become sufficiently strong to destroy the translational symmetry of the lattice. In this regime, the fluctuation amplitude of the transfer integral becomes of the same order of magnitude as its average value [11], the band description breaks down, and a crossover from the band-like transport in delocalized states to the incoherent hopping between localized states is predicted with increasing temperature. At low enough temperatures (T), when the band description is still valid, the polaronic bandwidth, W , “shrinks” as T increases, leading to a decrease of the carrier mobility μ with T [12–18].

The benchmark for the study of charge transport in organic semiconductors was established by time-of-flight (TOF) experiments with ultrapure polyacene crystals, such as naphthalene and anthracene [19]. These experiments have demonstrated that the intrinsic (not limited by static disorder) charge transport can be realized in the bulk of these crystals. This transport regime is characterized with a rapid growth of the carrier mobility with decreasing temperature and a pronounced anisotropy of the mobility, which reflects the anisotropy of the intermolecular transfer integrals [12,13]. Numerous applications, however, are dependent on the charge transport on

Charge Carrier Transport in Single-Crystal Organic Field-Effect Transistors 29

the surface of organic semiconductors. The most important example is the organic field-effect transistor, in which field-induced charges move along the interface between an organic semiconductor and a gate dielectric. In these devices, conduction truly occurs at the surface because the thickness of the conducting channel does not exceed a few molecular layers [20–22].

The transport of field-induced carriers on organic surfaces may differ from the bulk transport in many respects. For instance, the density of carriers in the field-effect experiments can exceed that in the bulk TOF measurements by many orders of magnitude, approaching the regime when the intercharge distance becomes comparable with the size of small polarons [23,24]. Interactions between the polaronic carriers may become important in this regime. Also, the motion of charge carriers in the field-induced conduction channel might be affected by the polarization of the gate dielectric [25]. Finally, molecular packing at organic surfaces could be different from that in the bulk.

Exploration of the polaronic transport on organic surfaces is crucial for better understanding of the fundamental processes that determine operation and ultimate performance of organic electronic devices. This is an important issue. On the one hand, the first all-organic devices (e.g., the active matrix displays based on organic light-emitted diodes and organic transistors) are expected to be commercialized within a few years. On the other hand, our knowledge of transport properties of organic semiconductors is much more limited than it is for their inorganic counterparts. This paradoxical situation contrasts sharply to the situation in inorganic electronics in the mid-1960s, when the first Si metal-oxide semiconductor field-effect transistors (MOSFETs) were developed [26].

Difficulties in fundamental research have been caused by the lack of a proper tool for exploring the polaronic transport on surfaces of organic semiconductors. The most common organic electronic device, whose operation relies on surface transport, is the organic thin-film transistor (TFT). Over the past two decades a large effort in the development of TFTs has resulted in an impressive improvement of the characteristics of these devices [27] so that, currently, the best organic TFTs outperform the widely used amorphous silicon (α -Si:H) transistors. However, even in the best organic TFTs, charge transport is still dominated by the presence of structural defects and chemical impurities. As a result, it has been concluded that TFTs cannot be reliably used for the studies of basic transport mechanisms in organic materials [28].

The recently developed *single-crystal* organic transistors with significantly reduced disorder [29–37] provide unique opportunities to explore fundamental processes that determine operation and reliability of organic electronic devices. For the first time, these single-crystal organic field-effect transistors (OFETs) have enabled the observation of the intrinsic (not limited by static disorder) transport of field-induced charges at organic surfaces [35,38,39]. The carrier mobility in these devices is an order of magnitude greater than that in the best organic TFTs [32]. Equally important, the single-crystal OFETs are characterized by a very good reproducibility: Devices fabricated in different laboratories exhibit similar characteristics. This reproducibility, which is crucial for the fundamental investigations of electronic properties of organic semiconductors, has never been achieved with thin-film devices, whose

electrical characteristics are strongly dependent on the details of fabrication processes and handling environment.

In this chapter, we present a brief overview of the experimental results obtained with single-crystal OFETs over the last four years. In Section 2.1.2, we briefly describe the crystal growth and OFET fabrication techniques that preserve the high quality of pristine surfaces of as-grown crystals. Section 2.1.3 focuses on the intrinsic transport characteristics of surfaces and interfaces of organic crystalline devices. Electronic defects at organic surfaces and mechanisms of their formation are discussed in Section 2.1.4. Section 2.1.5 outlines several basic issues that can be experimentally addressed in the near future owing to the availability of single-crystal OFETs.

2.1.2 FABRICATION OF SINGLE-CRYSTAL OFETs

The first step in the fabrication of single-crystal OFETs is the growth of ultrapure organic crystals. The best results to date have been obtained with *physical vapor transport* (PVT) growth in a stream of ultrahigh purity argon, helium, or hydrogen gases, similar to the method suggested by Laudise et al. [40]. A PVT furnace consists of a quartz tube with a stabilized temperature profile created along the tube by external heaters (Figure 2.1.1). The temperature gradient can be achieved by resistively heated wire unevenly wound on the quartz tube or, more conveniently, by coaxially enclosing the quartz tube in a metal tube (copper, brass, or stainless steel) with two regions of stabilized temperature: high T on the left and low T on the right (Figure 2.1.1).

In such design, good thermal conductivity of the metal allows one to achieve a linear temperature distribution between the heated and cooled regions, with the

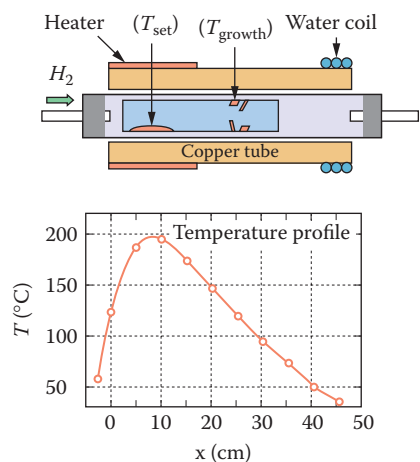


FIGURE 2.1.1 A sketch of the physical vapor transport (PVT) growth furnace (top) and an example of the temperature profile along the axis of the quartz tube (bottom).

Charge Carrier Transport in Single-Crystal Organic Field-Effect Transistors 31

temperature gradient inversely proportional to the length of the metal tube. This helps to create a smooth temperature profile along the growth reactor. In addition, the outer metal tube reduces the access of ambient light to the organic material, which might be important in the case of photosensitive organic compounds.

Starting material is loaded into the high-temperature zone and maintained at temperature T_{set} , where sublimation takes place, and molecules are carried by the gas stream into the region of lower temperature. At any certain concentration of evaporated molecules, defined by the temperature T_{set} , there is a point located downstream at a lower temperature, T_{growth} , where crystallization occurs. At this point, crystallization rate (proportional to the density of molecular vapor) becomes slightly greater than the rate of sublimation from crystal facets kept at temperature T_{growth} . Although both crystallization and sublimation occur at a facet simultaneously, the growth prevails and free-standing crystals grow. In the region to the left from the growth zone (upstream), sublimation prevails and no growth occurs; in the region to the right (downstream), the density of molecular vapor decreases and crystallization also does not occur. In this region, only smaller molecular weight impurities condense.

If the temperature T_{set} is maintained very low (near the sublimation threshold of the material), heavier molecular impurities do not sublime and are retained in the load zone. This creates a 2- to 3-cm wide crystallization region that is typically well separated from the original material and from the impurities. Therefore, PVT process results in the crystal growth and material purification at the same time. For better separation of the crystals from the impurities, the temperature gradient along the tube should be maintained sufficiently small (e.g., $\sim 5\text{--}10^\circ\text{C}/\text{cm}$).

Several factors affect the morphology and the quality of the grown crystals. Important parameters are, for instance, temperature of the sublimation zone, T_{set} , and the carrier gas. For each material and each furnace, the optimal set of parameters has to be determined empirically. At least one common tendency has been observed for the common compounds, such as 7,7',8,8'-tetracyanoquinodimethane (TCNQ), tetracene, and rubrene: The slower the growth process is, the higher the field-effect mobilities obtained in the resultant OFETs are. For this reason, T_{set} should be adjusted close to the sublimation threshold of the material. Typical T_{set} resulting in very slow growth of bulky crystals with large and flat facets is: 200, 210, and 300°C for the growth of TCNQ, tetracene, and rubrene, respectively. At such conditions, typical growth duration is 40–70 hours for 100–300 mg loaded material and H_2 gas flow rate ~ 100 cc/min.

Large, high-purity organic crystals can be obtained by the PVT technique (Figure 2.1.2). Most of the organic crystals are shaped as thin platelets or needles. The crystal shape is controlled by the anisotropy of intermolecular interactions: For many materials, the largest crystal dimension corresponds to the direction of the strongest interactions and, presumably, the strongest overlap of π -orbitals of adjacent molecules. For this reason, the direction of the fastest growth of elongated rubrene crystals (b axis) coincides with the direction of the highest mobility of field-induced carriers (see Section 2.1.3). In platelet-like crystals, the largest natural facet typically corresponds to the a - b plane. In-plane dimensions range from a few square millimeters

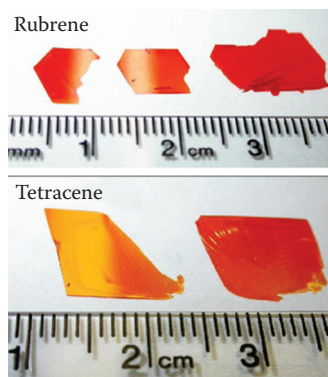


FIGURE 2.1.2 Single crystals of rubrene and tetracene grown from the vapor phase.

to a square centimeter. The crystal thickness also varies over a wide range and, in most cases, can be controlled by stopping the growth process at an early stage.

For example, the thickness of the tetracene crystals grown for 24 hours ranges between ~ 10 and ~ 200 μm [41]; however, it is possible to produce crystals of submicron thickness by interrupting the growth after ~ 10 min. According to the atomic force microscopy (AFM) studies (Figure 2.1.3) [42], the slow crystal growth proceeds by the *flow of steps* at a very low growth rate (≤ 10 $\mu\text{m}/\text{hour}$ in the direction perpendicular to the *a-b* facet) and results in molecularly flat facets with a low density of molecular steps, separated by relatively wide (0.5 – 1 μm) terraces.

Several ultrahigh-purity gases have been used as a carrier agent. In de Boer, Klapwijk, and Morpurgo [31], the highest mobility of tetracene-based devices, $\mu = 0.4$ cm^2/Vs , was realized with argon, whereas other groups reported slightly higher mobilities in tetracene grown in hydrogen (0.8 – 1.3 cm^2/Vs) [36,43]. The best reported mobilities in rubrene have been measured in the crystals grown in ultrahigh-

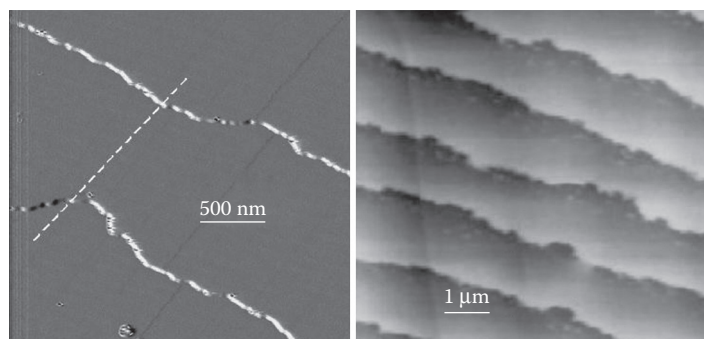


FIGURE 2.1.3 AFM images of the surface of uncleaved vapor-grown rubrene (left) and TCNQ (right) crystals, showing the molecular growth steps. The height of the steps is consistent with the lattice parameter along the *c* axis in these crystals. (From Menard, E. et al., unpublished.)

purity (UHP) H_2 . The carrier gas might also influence the size and morphology of the crystals. For instance, growth of tetracene in helium gas yields very thin and wide crystals, inappropriate for fabrication of free-standing OFETs, though useful for lamination on hard substrates.

On the other hand, slow growth in H_2 or Ar yields much thicker (bulkier) and robust tetracene crystals that can be used to create free-standing devices using parylene gate dielectric with mobilities up to $\sim 1 \text{ cm}^2/\text{Vs}$ [43]. Similar tendencies in morphology with the carrier gas have been observed for rubrene. At present, it is still unclear how, exactly, the transport gas affects the crystal quality, and more systematic studies are required. Poorly controlled factors such as parts per million (ppm) levels of water, oxygen, and other impurities in UHP gases that might create charge traps in organic material could complicate such studies.

Another poorly controlled parameter is the purity of the starting material. Empirically, different grades of material with the same nominal purity might result in crystals of quite different quality (in terms of the field-effect mobility). Normally, the density of impurities can be greatly reduced by performing several regrowth cycles, in which previously grown crystals are used as a load for the subsequent growths. However, after a gradual increase of μ with the number of purifications, the mobility saturates already after two or three cycles. This indicates that some of the impurities cannot be effectively removed from the material or new defects might be forming during the growth process. Clearly, the higher the purity of the starting material is, the fewer regrowth cycles are required. In Podzorov et al. [30], the rubrene OFETs with $\mu > 5 \text{ cm}^2/\text{Vs}$ have been fabricated from the “sublimed grade” rubrene (Sigma–Aldrich) after only one or two growth cycles.

Besides the growth from a vapor phase, other techniques, such as Bridgman growth from a melt or crystallization from a solution, can be used to produce organic crystals. For instance, vapor-Bridgman growth from a saturated vapor in a sealed ampoule has been used to grow large tetracene crystals for TOF studies (Figure 2.1.4) [44]. Crystallization from a solution usually results in mobilities substantially lower than those obtained in vapor-grown crystals. A clear demonstration of this has been recently obtained with OFETs based on single crystals of halogenated tetracene derivatives that are soluble in common organic solvents and can also be sublimed without decomposition [45]. OFET mobilities in the vapor-grown crystals were as high as $1.6 \text{ cm}^2/\text{Vs}$, while the solution growth resulted in devices with $\mu \sim 10^{-3} \text{ cm}^2/\text{Vs}$. A rare example of a high-mobility solution-grown crystalline system is dithiophene-tetrathiafulvalene (DT-TTF), with field-effect mobilities of up to $1.4 \text{ cm}^2/\text{Vs}$ [46].

It is worth noting that the mobility in single-crystal devices might be substantially improved if a zone refining process is used for prepurification of the starting material. Indeed, in the time-of-flight studies of organic crystals, the highest mobilities have been obtained after multiple cycles of zone-refinement purification. This process enabled reduction of impurity concentration in the bulk down to the part-per-billion level. It has to be noted that zone refinement cannot be applied to all organic materials, since this technique requires the existence of a coherent liquid phase (i.e., the melting temperature of a substance has to be lower than the temperature of decomposition of its molecules).



FIGURE 2.1.4 A tetracene crystal grown by the vapor-Bridgman technique and used for the time-of-flight studies. (From Niemax, J. et al., *Appl. Phys. Lett.*, 86, 122105, 2005.)

X-ray diffraction studies show that most of the PVT-grown crystals are of excellent structural quality; they are characterized by a very small mosaic spread, typically, less than 0.05° [47] (in rubrene this value has been found to be even smaller, $\sim 0.016^\circ$) [48]. Rubrene crystallizes in an orthorhombic structure with four molecules per unit cell and the lattice parameters $a = 14.44 \text{ \AA}$, $b = 7.18 \text{ \AA}$, and $c = 26.97 \text{ \AA}$ [49] (crystallographic data for several other polyacenes have been reported in Campbell et al. [50]). The crystals are usually elongated along the b axis; the largest flat facet of the crystal corresponds to the (a,b) -plane. The possibility of surface restructuring or existence of a “surface phase” on free facets of organic crystals has not been addressed yet and remains to be studied experimentally. Deviations of the surface structure from the bulk phase that might be important for the charge transport in OFETs might occur similarly to the thin-film phase in monolayer-thick pentacene films studied by grazing incidence x-ray diffraction [51,52].

Recently, it has been demonstrated that scanning tunneling microscopy (STM) could be used to study the molecular organization at the surfaces of bulk crystals in certain cases of high-mobility systems, such as rubrene [53]. Figure 2.1.5 shows the first molecular-resolution STM image of the surface of a bulk organic crystal (rubrene) at room temperature. The common problem of charging of an insulating surface with the tunneling electrons is avoided here because the high mobility of carriers in rubrene facilitates fast removal of the tunneled electrons through the crystal into the conducting substrate. The surface quality of these crystals is unprecedented; the density of surface defects is very low, resulting in a low-noise image and the opportunity to resolve individual molecules at the surface. The packing motif observed with an STM at the surface is consistent with the bulk packing obtained by crystallography. It is a “herringbone” type of structure with a stack forming along the b axis.

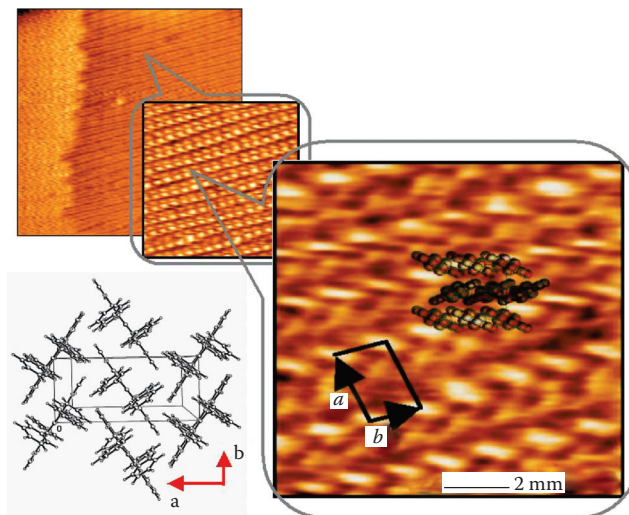


FIGURE 2.1.5 Scanning tunneling microscope images of a - b facet of a thick, as-grown rubrene crystal. The herringbone molecular organization at the surface, consistent with the bulk structure (shown in the lower left corner), is evident. (From Menard, E. et al., to appear in *Adv. Mater.*, 2006.)

AU: update?

Fabrication of field-effect structures on the surface of organic crystals is a challenge because the conventional processes of thin-film technology (such as sputtering, photolithography, etc.) introduce a high density of defects on vulnerable organic surfaces. For this reason, the first single-crystal OFETs have been realized only recently, after development of the two innovative fabrication techniques briefly described next.

The first technique is based on the use of an unconventional gate dielectric: thin polymeric film of *pyralene*, which can be deposited from a vapor phase on the surface of organic crystals at room temperature, producing a defect-free semiconductor–dielectric interface [29]. Conformal parylene coating is a well developed technology used commercially in electronic packaging applications [54]. A home-built setup for parylene deposition is depicted in Figure 2.1.6 (commercially available parylene coaters are not recommended for this research purpose because of their large volume and high cost).

The reactor consists of a 20-mm ID quartz tube blocked at one end and a two-zone furnace for sublimation and pyrolysis of the commercially available parylene dimers. The quartz tube extends from the high- T (700°C) section of the furnace by about 40 cm to the right; the sample(s) with prefabricated contacts and leads are placed in this portion of the tube, which is then connected to the mechanical pump through a liquid N_2 trap. After evacuating the reactor to approximately 10^{-2} torr, the temperatures in the sublimation and pyrolysis zones are set to 100 and 700°C, correspondingly. Parylene dimers, sublimed at 100°C, split into monomers at 700°C and polymerize as they enter the room temperature section of the tube, producing a clear pinhole-free insulating coating on the sample's surface.

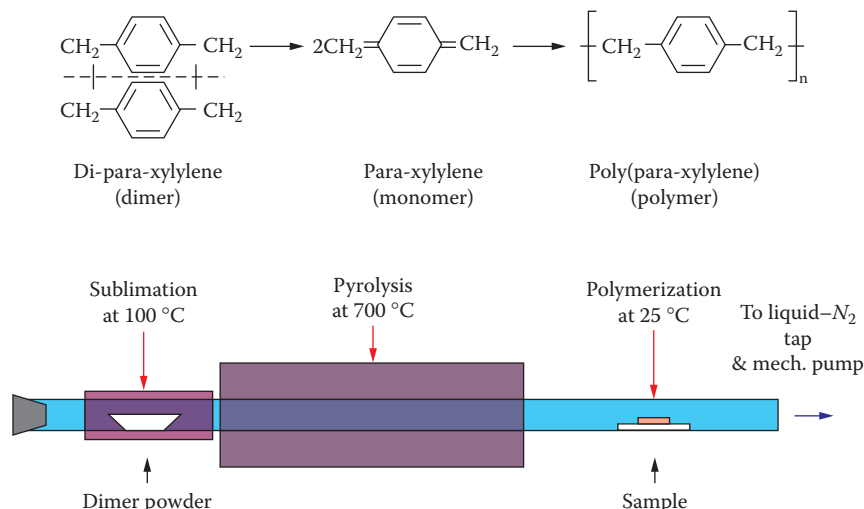


FIGURE 2.1.6 Reactions involved in parylene deposition process (top): sublimation of dimers at $\sim 100^\circ\text{C}$, splitting into monomers at $\sim 700^\circ\text{C}$, and polymerization at room temperature. Inexpensive system for parylene deposition (bottom) consists of a two-zone tube furnace and a 20-mm ID quartz tube containing parylene and dimer powder and connected to a one-stage mechanical pump through a liquid nitrogen trap. A sample with prefabricated contacts and attached wire leads is placed in the tube at about 30 cm from the furnace.

The advantages of this technique are the following:

High-energy charged particles, inherent to plasma-based deposition techniques (e.g., sputtering) and detrimental for the organic surfaces, are avoided.

The sample is maintained at room temperature throughout the entire process. A high vacuum is not required, which, in a combination with cheap parylene precursors, makes this technique of a very low cost.

The deposition process is fast: Growth of a 1- μm thick film lasts ~ 20 min.

The physical properties of parylene films are remarkable: Parylene is a very good insulator with the electrical breakdown strength of up to 10 MV/cm, superior chemical stability, and high optical clarity.

The coating is truly conformal, which allows working with crystals that have sharp features on their surfaces (e.g., steps, edges, etc.), without having problems with shorts.

The conformal properties of parylene coating are especially important in devices with colloidal graphite contacts that have rough surfaces. The parylene coating is the only technique available to date for the fabrication of *free-standing* single crystal OFETs. In comparison with the laminated devices, this has several advantages, such as elimination of substrate-related strains and a possibility to perform studies of photoinduced effects in OFETs by illuminating conduction channels through the transparent parylene dielectric and a (semi)transparent gate electrode [55]. The

Charge Carrier Transport in Single-Crystal Organic Field-Effect Transistors 37

OFETs with parylene dielectric are very stable. For example, the characteristics of rubrene/parylene transistors remained unchanged after storing the devices for more than two years in air and in the dark.

Note that for the free-standing devices, deposition of metal contacts directly on the surface of organic crystal is necessary. While painting colloidal graphite contacts (e.g., Aquadag Colloidal Graphite, Ted Pella, Inc.) on the crystal surface works well and results in low contact resistance, it is difficult to create complex contact geometries and well-defined features with this simple technique. An alternative high-vacuum thermal evaporation of metals through a shadow mask is challenging due to several factors related to generation of defects at the organic surfaces as a result of (1) infrared radiation from evaporation sources; (2) contamination of the channel area with metal atoms able to penetrate under the shadow mask; and (3) interaction of organic surfaces with free radicals produced by hot filaments and high-vacuum gauges (the *gauge effect*) [56]. Nevertheless, devices with evaporated contacts have been successfully fabricated in Podzorov et al. [30] by using an optimized deposition chamber — a technique that might be useful for more complex contact geometries in OFETs, such as four-probe or Hall geometry.

In the second technique of single-crystal OFET fabrication, the transistor circuitry is prefabricated by conventional microfabrication (lithography) methods on a substrate (this structure can be called a “stamp”), and organic single crystal is subsequently laminated to it. This technique eliminates the need for deposition of metal contacts and dielectrics directly onto organic crystals. Hard inorganic (e.g., Si) and flexible elastomeric (polydimethylsiloxane = PDMS) stamps have been used for this purpose. In the first case, a heavily doped Si wafer with a thermal SiO₂ plays the role of an insulated gate electrode [31,33]. After the deposition of gold contacts, a thin organic crystal can be laminated to such a stamp owing to van der Waals attraction forces. Similarly, field-effect transistor (FET) structure can be fabricated using PDMS substrates and spin-coated PDMS films [35].

The elastomeric stamps compare favorably with the Si stamps in two respects. First, slightly conformal properties of PDMS enable establishing a good contact even with crystals that are not perfectly flat. Conversely, the use of hard Si stamps is restricted to perfectly flat crystals or to very thin and “bendable” crystals that could conform to hard substrate. Second, for the robust and bulky crystals such as rubrene, the PDMS stamps provide a unique opportunity to re-establish the contact many times without breaking the crystal and without degradation of the crystal’s surface. However, the achievable density of field-induced charges is typically greater in the Si-based stamps, especially if these stamps utilize high- ϵ gate insulators [23,57]. This is important for the exploration of the regime of high carrier densities, in which novel electronic phases might emerge (see Section 2.1.3.7).

Even though the lamination of crystals on prefabricated substrates enables a “low-impact” probing of charge transport on organic surfaces, this impact may still be too strong for chemically reactive organic materials (e.g., a strong electron acceptor TCNQ). To minimize these effects and to preserve the pristine surface of organic crystals, modification of the PDMS stamping technique has been recently introduced that allows avoiding these complications simply by eliminating the direct contact between the crystal and the gate dielectric [39]. The idea of these so-called

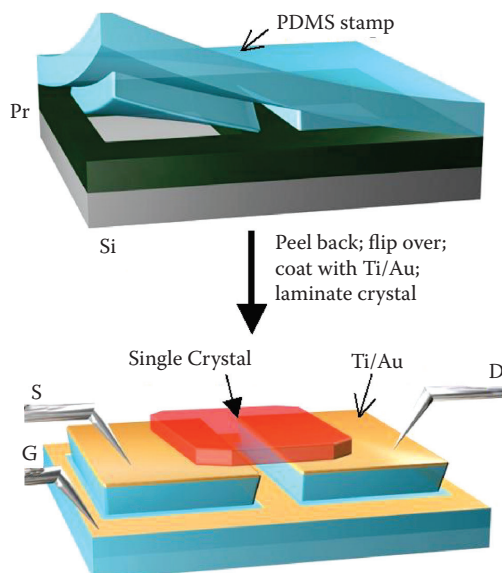


FIGURE 2.1.7 Casting and curing procedures for fabrication of the “air-gap” transistor stamps. The recessed gate electrode is separated from the conductive channel by a micron-size gap. (From Menard, E. et al., *Adv. Mater.*, 16, 2097, 2004.)

vacuum-gap stamps is illustrated in Figure 2.1.7. In these devices, the conventional dielectric is replaced by a micron-size gap between the gate electrode and the surface of organic semiconductor. A thin layer of a gas (e.g., air) or vacuum between the bottom surface of the crystal and the recessed gate electrode plays the role of the gate dielectric. This approach eliminates surface defects introduced in the process of lamination and enables studies of the effect of different gases and other environmental agents on the conduction channel in OFETs [56].

2.1.3 CHARGE TRANSPORT ON THE SURFACE OF ORGANIC SINGLE CRYSTALS

In this section, after a brief introduction of the OFET operation principles, we outline the main signatures of the intrinsic polaronic transport observed in the experiments with single-crystal OFETs. We compare them to the results of TOF and space-charge limited current (SCLC) experiments that probe the charge transport in the bulk.

2.1.3.1 BASIC FET OPERATION

Contemporary OFETs are based on undoped organic semiconductors, and mobile charges in these devices must be injected from the metallic contacts. These devices can potentially operate in the *electron*- and the *hole*-accumulation modes, depending on the polarity of the gate voltage (the so-called ambipolar operation). Often, however, the injection barrier at the contact or the field-effect threshold for either *n*- or

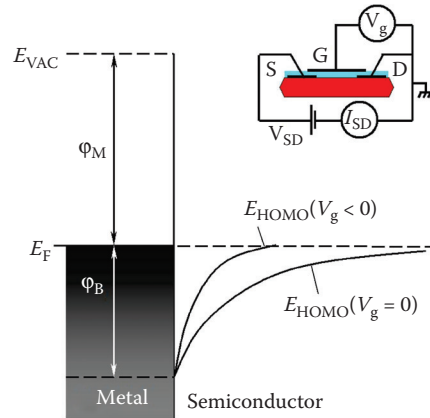


FIGURE 2.1.8 Schematic energy diagram of a metal–organic interface: the contact. E_{vac} is the vacuum energy level, E_{F} is the Fermi energy of metal, E_{HOMO} is the energy of the band edge of the semiconductor. The inset shows a two-probe OFET circuitry: S and D are the source and drain contacts, G is the gate electrode; V_{g} and V_{SD} are the gate and source-drain voltages, respectively, and I_{SD} is the source-drain current.

p -type conductivity is so large that an FET operates in a unipolar mode. For this reason, we will mainly discuss the p -type conductivity, which is more commonly observed in OFETs.

We will start the discussion with charge injection from contacts. An energy diagram of a hole injecting metal–semiconductor contact and a generic field-effect transistor circuit are schematically shown in Figure 2.1.8. The hole injection occurs through the interfacial Schottky barrier of height ϕ_{B} ; the formation of the barrier is a complex process that depends on the metal work function ϕ_{M} , ionization energy of the semiconductor, and interfacial dipole moment formed due to a charge transfer at the interface. For a comprehensive review of energetics of metal–organic interfaces, see, for example, the paper by Cahen et al. [58]. While the maximum height of the barrier, ϕ_{B} , remains fixed due to the pinning of energy levels at the interface, its width can be modified by an external electric field associated with either V_{SD} or V_{g} .

Figure 2.1.8 shows that when a negative V_{g} is applied, the effective width of the Schottky barrier for hole injection decreases. This results in a decrease of the contact resistance (R_{C}), which depends on the barrier height ϕ_{B} , its effective thickness, and temperature. The triangular shape of the Schottky barrier allows the carrier injection via thermally activated excitation above the barrier and via tunneling under the barrier (the latter process does not require thermal excitation, but it is limited by V_{g} -dependent barrier width). Both processes are possible, and the resultant injection mechanism, called *thermionic emission*, typically causes an exponentially fast increase of the contact resistance R_{C} with lowering T and a strong dependence of R_{C} on the gate voltage.

The contact resistance enters the equations of OFET operation because the source-drain circuit is represented by two resistors connected in series — the contact resistance, R_{C} , and the channel resistance, R_{CH} — so that the total source-drain

resistance is $R_{SD} \equiv V_{SD}/I_{SD} = R_C + R_{CH}$. The Schottky contact resistance in OFETs is typically high; in many cases, $R_C \geq R_{CH}$, especially in short-channel TFTs, and the operation of such devices is contact limited. This is also the case for short-channel single-crystal OFETs. However, if the channel is long enough (0.2–5 mm), rubrene and tetracene devices with either graphite or laminated gold/PDMS contacts are not contact limited at room temperature. The devices with evaporated silver or gold contacts generally have higher contact resistances. Nevertheless, R_C typically decreases with V_{SD} , and at large enough V_{SD} and $V_g < 0$, even the devices with evaporated contacts are not dominated by contacts. However, because of a strong T -dependence of the contact resistance, it is important to be able to directly measure R_C and R_{CH} independently in each individual OFET in the entire temperature range of interest.

In the prior studies, contact resistance was estimated by measurements of two-probe OFETs and fitting the data with the Schottky model at different T and V_g [59] and by performing the channel length scaling analysis [60,61]. While these methods provide useful information about the contacts of a particular system, they do not allow for the direct and model-independent measurement of the contact resistance in each individual device. Recently introduced OFETs with four-probe contact geometry (source, drain, and two voltage probes in the channel) can be used to address this problem [29,30]. Before describing the four-probe measurements, let us introduce the operation of a conventional two-probe OFET, assuming that the contact resistance is negligible compared to the channel resistance. (This is practically valid for some cases of single-crystal OFETs with long channels at room temperature.)

With an increase of the gate voltage $|V_g|$ towards the threshold value $|V_g^{th}|$, the carriers injected from the metallic contacts fill localized in-gap states of the organic semiconductor, associated with impurities and defects in the channel, whose energy is separated from the edge of the HOMO band by more than a few $k_B T$ (the deep traps; see Figure 2.1.9) (this simplified model assumes the existence of the HOMO band; this assumption may be violated at high temperatures) [12,62]. As the result, the Fermi level at the organic surface, E_F , initially positioned within the HOMO–LUMO gap, approaches the edge of the HOMO band, E_{HOMO} , which corresponds to the zero energy in Figure 2.1.9.

As soon as $E_F - E_{HOMO}$ becomes smaller than $\sim k_B T$, the OFET's conductance increases by several orders of magnitude due to the thermal excitation of the carriers from the localized states into the HOMO band. As the result, a conduction channel is formed at the interface between the semiconductor and the gate dielectric. Overall device operation depends, to a large extent, on the energetics of the semiconductor bands and metal contacts, and therefore studies of the electronic structure of molecular interfaces are important [58].

Figure 2.1.10 shows the transconductance characteristics (i.e., the dependence of the source-drain current on the gate voltage, $I_{SD}(V_g)$, measured at a constant source-drain voltage, V_{SD}) and $I_{SD}(V_{SD})$ characteristics typical for the p -type rubrene single-crystal OFETs [29,30,39]. The channel conductance per square,

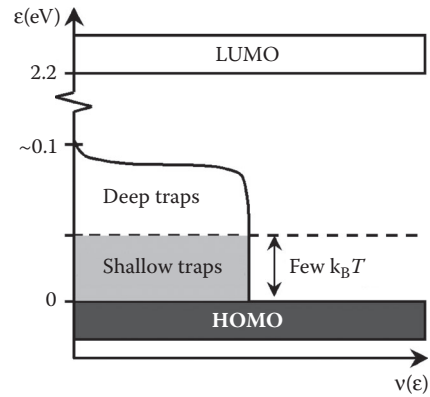


FIGURE 2.1.9 The schematic diagram of the energy distribution of localized electronic states in the energy gap between the HOMO and LUMO bands in the rubrene single-crystal OFETs. (From Podzorov, V. et al., *Phys. Rev. Lett.*, 93, 086602, 2004.)

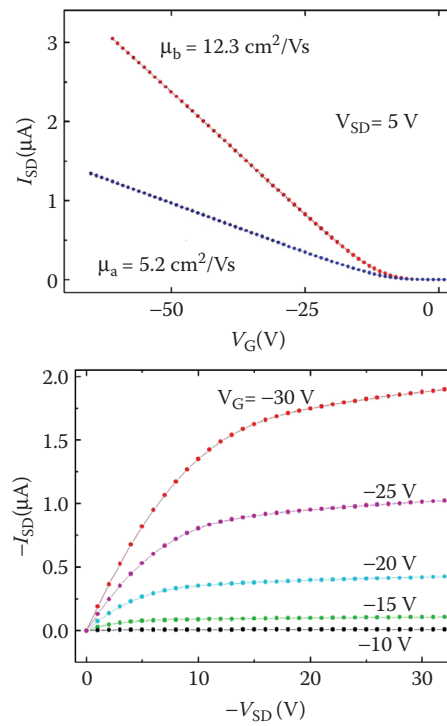


FIGURE 2.1.10 The transconductance $I_{SD}(V_g)$ (the upper panel) and $I_{SD}(V_{SD})$ (the lower panel) characteristics of rubrene single-crystal OFET (see, for example, Podzorov et al. [30] and Menard et al. [39]).

$$\sigma \equiv \frac{I_{SD}}{V_{SD}} \frac{L}{W},$$

increases linearly with V_g at $|V_g| > |V_g^{th}|$. (Here, L and W are the length and width of the conduction channel, respectively.) This indicates that the carrier mobility [63]

$$\mu \equiv \frac{\sigma}{en} = \left(\frac{1}{C_i V_{SD}} \right) \left(\frac{dI_{SD}}{dV_g} \right) \frac{L}{W} \quad (2.1.1)$$

does not depend on the density of carriers field-induced above the threshold

$$n = C_i (V_g - V_g^{th}) / e \quad (2.1.2)$$

Here, C_i is the capacitance per unit area between the gate electrode and the conduction channel.

A *density-independent* μ has been observed in devices based on single crystals of rubrene [30,35,36], pentacene [33,34], tetracene [31], and TCNQ [39]. This important characteristic of single-crystal OFETs contrasts sharply with a strongly V_g -dependent mobility observed in organic TFTs [64] and α -Si:H FETs [65]. In the latter case, the density of localized states within the gap is so high that the Fermi level remains in the gap even at high $|V_g|$ values.

The observation of V_g -independent mobility in single-crystal OFETs suggests that the charge transport in these structures does not require thermal activation to the mobility edge and the mobile field-induced carriers occupy energy states within the HOMO band. This is consistent with an increase of the mobility with cooling observed in high-quality single-crystal OFETs (see Section 2.1.3.4). (For comparison, μ decreases exponentially with lowering temperature in organic and α -Si:H TFTs.) The pronounced difference in the V_g - and T -dependences of the mobility in these two types of devices clearly indicates that the theoretical models developed for the charge transport in α -Si:H and organic TFTs [65] are not applicable to single-crystal OFETs.

In the cases when contact resistance is not negligible, four-probe OFETs are used to measure the channel and the contact resistances independently. In the four-probe OFET geometry (Figure 2.1.11), in addition to I_{SD} , voltage between a couple of extra probes located in the middle of the channel, V_{4w} , can be measured as a function of V_g , V_{SD} , and T . Gate voltage dependences of I_{SD} and V_{4w} for a typical four-probe OFET are shown in the upper panel of Figure 2.1.12. In the four-probe geometry, conductivity of the section of the channel between the voltage probes per square is:

$$\sigma \equiv \frac{I_{SD}}{V_{4w}} \frac{D}{W}$$

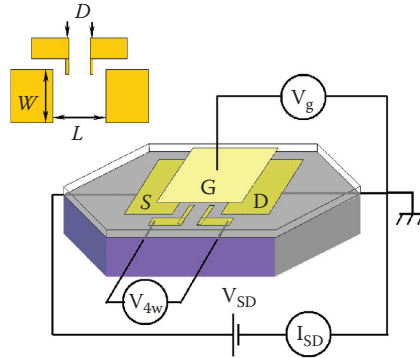


FIGURE 2.1.11 Four-probe field-effect transistor with measurement circuitry: V_{4w} is the voltage measured between the two voltage probes located in the middle of the channel. The inset shows the channel geometry: L and W are the channel length and width; D is the distance between the voltage probes.

Note that the voltage V_{4w} does not necessarily remain constant when V_g or T is varied because the total V_{SD} voltage applied to the device is distributed between the channel resistance, R_{CH} , and the contact resistance, R_C , both of which vary with V_g and T . Using the relationship $\sigma = en\mu$, and n from (2), we obtain for the contact-resistance-corrected channel mobility, μ_{4w} :

$$\mu_{4w} = \left(\frac{1}{C_i} \right) \left(\frac{d(I_{SD}/V_{4w})}{dV_g} \right) \frac{D}{W} \quad (2.1.3)$$

and for the contact resistance R_C :

$$R_C = \frac{V_{SD}}{I_{SD}} - \frac{L}{D} \frac{V_{4w}}{I_{SD}} \quad (2.1.4)$$

Typical V_g - and V_{SD} -dependences of the contact resistance, normalized to the channel width, $R_C W$, are shown in the lower panel of Figure 2.1.12. In agreement with the Schottky model, R_C for a p -type device decreases with a positive V_{SD} applied to the hole-injecting source contact and with a negative V_g applied to the gate. Interestingly, the relatively large magnitude of the contact resistance in Figure 2.1.12 (≥ 100 k Ω -cm) can be greatly reduced down to 1–2 k Ω -cm by treating the gold contacts with trifluoromethylbenzenethiol before the crystal lamination or by using nickel instead of gold, which has been recently reported to result in a remarkably low contact resistance ~ 0.1 – 0.4 k Ω -cm [61].

For several important applications in plastic optoelectronics, including the possibility of electrically pumped organic lasers, it would be very important to achieve an ambipolar operation in OFETs, with high electron and hole mobilities. Gate-controlled electroluminescence from organic small-molecule thin-film transistors

AU: to what does (2) refer?

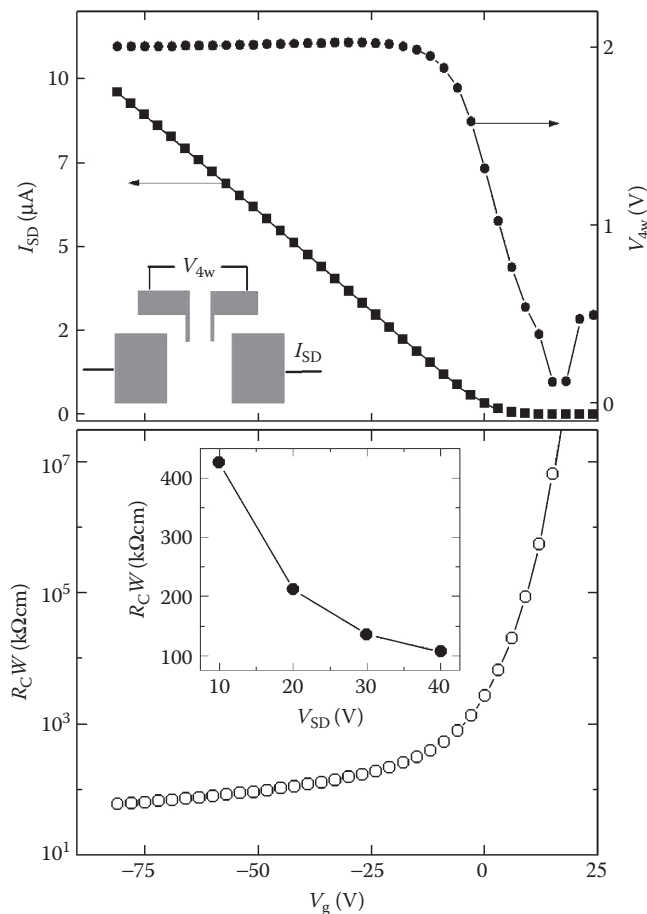


FIGURE 2.1.12 Four-probe OFET characteristics, $I_{SD}(V_g)$ and $V_{4w}(V_g)$ (top), and the corresponding contact resistance $R_C W(V_g)$ (bottom). The inset shows the dependence of the contact resistance on V_{SD} . (From Sundar V. C. et al., *Science*, 303, 1644, 2004.)

and, more recently, from single-crystal OFETs based on thiophene/phenylene oligomers has been observed (see, for example, Nakamura et al. [66] and references therein). However, because these devices have not been optimized yet, hole and electron currents were not balanced, and only unipolar (p -type) electrical characteristics have been observed.

Interestingly, V_g -controlled electroluminescence and ambipolar characteristics have been recently observed in conjugated polymer OFETs [67,68], which indicates a balanced electron and hole injection. However, low hole and electron mobilities ($\sim 10^{-3} \text{ cm}^2/\text{Vs}$), typical for polymer semiconductors, limit the channel current and therefore may present a serious problem for realization of electrically pumped polymer lasers. For this reason, ordered small-molecule organic semiconductors with higher mobilities are very promising for research in this direction.

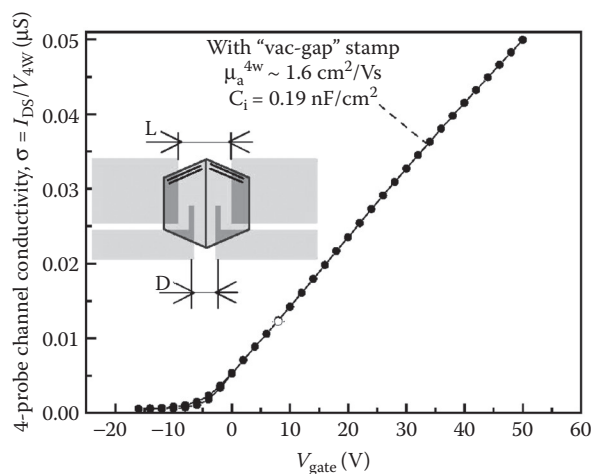


FIGURE 2.1.13 Channel conductivity along the a -axis of TCNQ single crystal measured in the “vacuum-gap” OFET. The mobility of n -type carriers is $1.6 \text{ cm}^2/\text{Vs}$. (From Menard, E. et al., *Adv. Mater.*, 16, 2097, 2004.)

Most of the small-molecule organic FETs operate in the p -type mode, and examples of n -type operation with high mobility are rare [39,69]. This “asymmetry” between n - and p -type carriers is due to several reasons: the HOMO bandwidth being typically larger than the LUMO bandwidth [17], a stronger trapping of n -type polarons [19], and a larger Schottky barrier for electron injection into organic semiconductors from the most commonly used high work function metals.

Figure 2.1.13 illustrates the n -type operation in a single-crystal TCNQ transistor. The surface of TCNQ, a semiconductor with a very high electron affinity, can be easily damaged (e.g., a direct contact of the crystal with PDMS dielectric in the contact stamps, such as those used in Houili et al. [35], results in a very poor transistor performance with electron mobilities $\sim (2\text{--}3)\cdot 10^{-3} \text{ cm}^2/\text{Vs}$). The “air-gap” PDMS stamps [39] help to solve the problem. The observed carrier mobility $\sim 1.6 \text{ cm}^2/\text{Vs}$ in the linear regime is significantly higher than in most of the n -channel organic TFTs. This value, however, is still limited by trapping (see Section. 2.1.3.2); more work is required to approach the fundamental limit of performance of n -type OFETs.

In practice, realization of high-mobility ambipolar operation is a challenge because two difficult problems must be solved simultaneously: (1) the density of both n - and p -type traps should be minimized at organic/dielectric interfaces; and (2) an effective injection of both n - and p -type carriers from the contacts into the organic semiconductor must be realized. Among inorganic FETs, only devices based on carbon nanotubes [70] and single crystals of transition metal dichalcogenides (e.g., WSe_2 and MoSe_2) [71] demonstrated high-mobility ambipolar operation. The number of organic materials in which the ambipolar operation has been demonstrated is limited as well [67,69,72,73]. The organic single crystals, with their intrinsically

low density of traps, offer a unique opportunity to realize the ambipolar operation with a relatively high mobility of both types of carriers.

Ambipolar operation has been recently observed in the single-crystal OFETs based on metal phthalocyanines (MPc), namely, FePc and CuPc [74] (Figure 2.1.14) and rubrene [75]. Because of the reduced density of electron traps at the interface and a relatively small HOMO–LUMO gap in the case of MPc (<1.5 eV), both electrons and holes can be injected in the organic crystal from the contacts. Interestingly, in these ambipolar single-crystal OFETs, both source and drain contacts were made of the same high work function metal (gold in MPc FETs and silver in rubrene FETs). Note that the CuPc-based TFTs with gold contacts demonstrate only unipolar *p*-type operation (presumably because of a high density of traps for electrons in thin films) [76].

Although the performance of these single-crystal OFETs in the *n*-type regime is still dominated by traps, the mobilities observed for holes and electrons (0.3 and 0.03 cm²/Vs in MPc FETs, respectively, and 1.8 and 0.011 cm²/Vs in rubrene FETs, respectively) compare favorably with that in the corresponding thin-film transistors employing Ca electrodes [72]. This indicates a good potential of the single-crystal OFETs for the studies of ambipolar charge injection, transport, and recombination processes.

In general, the performance of FET devices is characterized by many parameters, including the mobility, the threshold voltage, the ON/OFF ratio, and the subthreshold slope [32,63]. Next, we will focus on the first two parameters — the mobility, μ , and the threshold voltage, V_g^{th} — that are the most relevant to the physics of charge transport on the surface of organic semiconductors. Note that, with respect to other parameters (e.g., the subthreshold slope), single-crystal OFETs also compare favorably with the best organic and inorganic thin-film transistors (see, for example, Podzorov et al. [30]).

2.1.3.2 THE MULTIPLE TRAP-AND-RELEASE MODEL

Although the density of defects in the conduction channel of single-crystal OFETs is significantly lower than in organic TFTs, the defects are still present. These defects create localized electronic states in the HOMO–LUMO gap schematically shown in Figure 2.1.9 (the electronic defects will be discussed in more detail in Section 2.1.4). The effect of these states on charge transport depends on their energy. If the energy of a localized state is separated from the mobility edge (or, in other words, from the edge of HOMO(LUMO) for *p*(*n*)-type carriers) by more than a few $k_B T$, the state acts as a *deep trap*: once trapped in a deep trap, the charge cannot be released by thermal excitations. For the pristine surface of rubrene single crystals at room temperature, for instance, the density of deep traps can be as low as 10¹⁰ cm⁻². Conversely, trap states with energies within a few $k_B T$ near the mobility edge (*shallow traps*) are characterized with a finite trapping time; after being trapped for a characteristic time τ_t , a polaron can be thermally activated and released to the band.

At a phenomenological level, the effect of shallow traps on the channel conductivity can be described by the *multiple trap and release* (MTR) model [27,77]. According to this model, which helps to illustrate the distinction between the “intrinsic

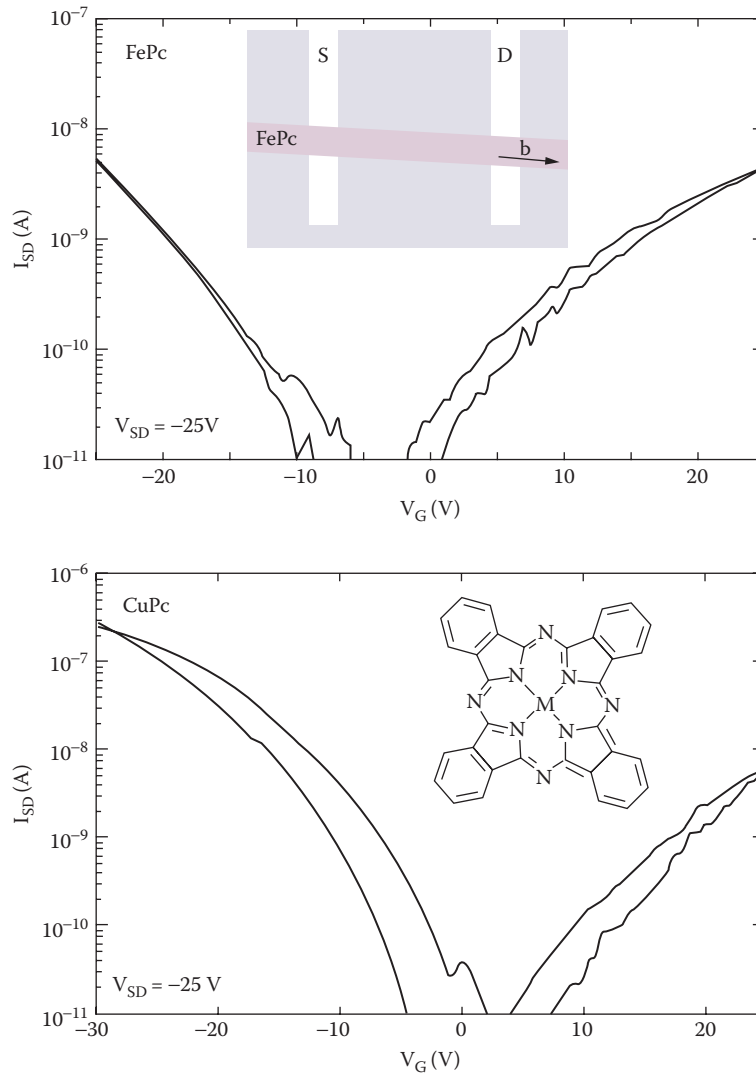


FIGURE 2.1.14 The transconductance characteristics of FePc and CuPc single-crystal FETs with gold electrodes. The hole mobilities reach $\sim 0.3 \text{ cm}^2/\text{Vs}$ for both FePc and CuPc; the electron mobilities are $3 \cdot 10^{-2} \text{ cm}^2/\text{Vs}$ and $10^{-3} \text{ cm}^2/\text{Vs}$, respectively. (From de Boer, R. W. I. et al., *Appl. Phys. Lett.*, 86, 262109, 2005.)

AU: correct?

“sic” and “trap-dominated” transport, not all the charges field induced above the threshold (at $|V_{gl}| > |V_g^{th}|$) contribute to the current flow at any given moment of time. Some of the mobile charges can be momentarily trapped by shallow traps; the number of these charges depends on the density of shallow traps and temperature.

Within the MTR model, the effect of trapping can be described using two approaches. In the first approach, one can assume that *all* carriers field induced above

the threshold, n , contribute to the current flow at any moment of time, but their effective mobility μ_{eff} is reduced in comparison with its intrinsic, trap-free value μ_0 :

$$\mu_{\text{eff}} = \mu_0(T) \frac{\tau(T)}{\tau(T) + \tau_{\text{tr}}(T)} \quad (2.1.5)$$

Here, $\tau_{\text{tr}}(T)$ is the average trapping time on shallow traps and $\tau(T)$ is the average time that a polaron spends diffusively traveling between the consecutive trapping events. In the alternative second approach, one can assume that only a fraction of the carriers field induced above the threshold voltage are moving at any given moment of time:

$$n_{\text{eff}} = n \frac{\tau(T)}{\tau(T) + \tau_{\text{tr}}(T)} \quad (2.1.6)$$

However, these charges are moving with the intrinsic trap-free mobility μ_0 .

These two approaches are equivalent for describing the channel conductivity $\sigma = en\mu$, which depends only on the product of n and μ . The distinction between these approaches becomes clear in the Hall effect measurements, in which the density and the intrinsic mobility of truly mobile carriers can be determined independently (see Section 2.1.3.4).

According to Equation 2.1.5, the intrinsic regime of conduction is realized when $\tau \gg \tau_{\text{tr}}$. In this case, the dependence $\sigma(T)$ reflects the temperature dependence of intrinsic mobility $\mu_0(T)$. In the opposite limit $\tau \ll \tau_{\text{tr}}$, the transport is dominated by shallow trapping processes. It will be shown below that the intrinsic regime is characterized by a large anisotropy of the charge transport, an increase of the mobility with decreasing temperature, and a conventional “nonactivated” Hall conductivity.

2.1.3.3 ANISOTROPY OF THE MOBILITY

Polyacenes typically form crystals with a herringbone packing of molecules (the molecular packing in rubrene crystals is shown in Figure 2.1.15). Transfer integrals between the adjacent molecules in these crystals vary significantly depending on the crystallographic direction [78–80]. This leads to a strong anisotropy of transport properties of organic crystals, which has been well documented in the TOF experiments [19]. However, prior to the development of single-crystal OFETs, the anisotropy had never been observed in the field-induced transport on the surface of organic semiconductors.

Several types of single-crystal OFETs based on rubrene demonstrate anisotropy of surface conductivity [35,38,48]. In rubrene devices based on PDMS stamps, the mobility along the crystallographic b axis exceeds the mobility along the a axis by a factor of ~three (figs. 2.1.10 and 2.1.16) [35]. Similar μ_{0b}/μ_{0a} ratio has been observed for rubrene transistors with parylene gate dielectric [48]. A clear correlation

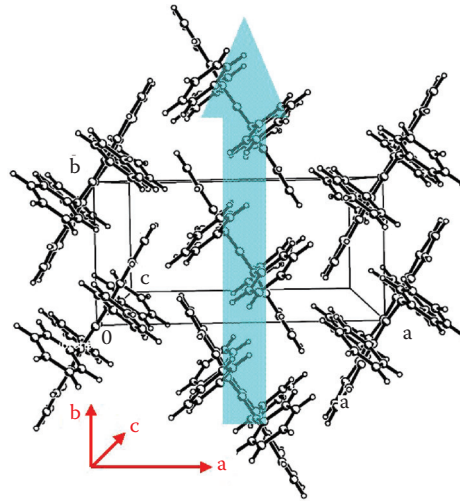


FIGURE 2.1.15 Packing of molecules in rubrene crystals. The crystal facets used for the FET fabrication correspond to the a - b crystallographic plane; the largest μ is observed for the charge transport along the b axis. (From Sundar V. C. et al., *Science*, 303, 1644, 2004.

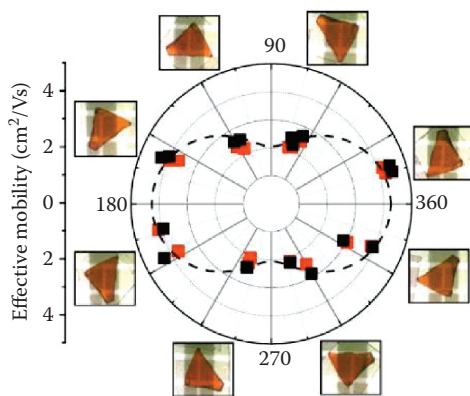
between the mobility and molecular packing has also been found recently in a family of tetrathiafulvalene derivatives [81].

Small density of shallow traps in the single-crystal rubrene OFETs facilitated observation of the mobility anisotropy. However, even in these devices, the anisotropy of μ_{eff} vanishes at lower temperatures (Figure 2.1.17), where the charge transport becomes trap dominated. To explain vanishing of the mobility anisotropy within the MTR model, one should take into account that τ_x , the time of travel between shallow traps along a certain crystallographic direction x , is inversely proportional to the intrinsic mobility along this direction, $\mu_0 x$. In the trap-dominated regime ($\tau \ll \tau_{tr}$), Equation 2.1.5 is reduced to

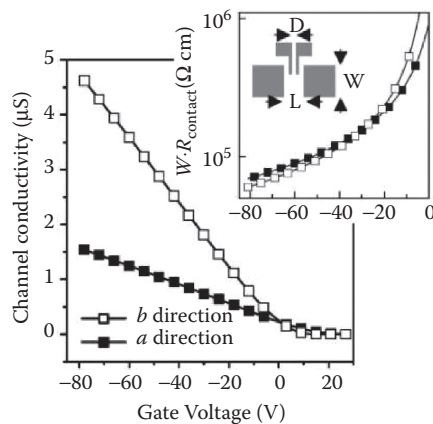
$$\mu_{\text{eff}} = \mu_0^x \frac{\tau_x}{\tau_{tr}}$$

and μ_{eff} becomes independent on the crystallographic direction. The higher the shallow trap density is, the narrower is the temperature range where the mobility anisotropy can be observed.

Qualitatively, the observed anisotropy of μ in rubrene can be explained on the basis of the molecular packing in these crystals (Figure 2.1.15). Due to the cofacial orientation of molecules in the stacks along the b axis, the charge motion along the stacks is facilitated in comparison with that in the perpendicular direction. Recent calculations of the band structure of rubrene based on the methods of quantum chemistry confirmed that the value of transfer integrals reaches a maximum for the b axis [17]. For the quantitative description of the mobility anisotropy and its



(a)



(b)

FIGURE 2.1.16 (a) Polar plot of the mobility at the rubrene a - b surface (the angle is measured between the b axis and the direction of current flow). (b) The four-probe measurements of the channel conductivity and the contact resistance (inset) as a function of V_g along the b and a axes; the μ values measured along the b and a axes are $15.4 \text{ cm}^2/\text{Vs}$ and $4.4 \text{ cm}^2/\text{Vs}$, respectively. (From Sundar V. C. et al., *Science*, 303, 1644, 2004.)

temperature dependence, *ab initio* calculations that take into account intra- and intermolecular vibrations are needed; currently, such calculations are available only for bulk conduction in crystals of linear polyacenes (naphthalene, anthracene, and tetracene) [12,13].

2.1.3.4 LONGITUDINAL AND HALL CONDUCTIVITY IN RUBRENE OFETs

The intrinsic and trap-dominated transport regimes in single-crystal OFETs can be identified by measuring the conductivity over a wide temperature range. The lon-

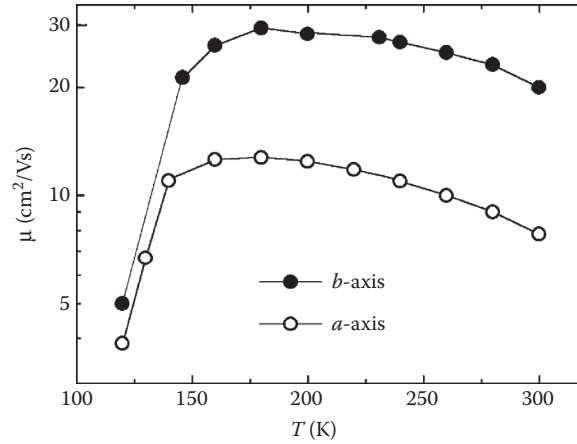


FIGURE 2.1.17 Temperature dependence of the mobility in rubrene OFET extracted from the four-probe measurements of the conductivity along the a and b axes. (From Podzorov, V. et al., *Phys. Rev. Lett.*, 93, 086602, 2004.)

gitudinal conductivity of rubrene single-crystal OFETs, measured at different T as a function of V_g , is shown in Figure 2.1.18. Assuming that all charges, n , field induced above the threshold are moving with a nonzero effective velocity at any moment of time, one can attribute the observed T -variations of the slope $d\sigma/dV_g$ to the nonmonotonic temperature dependence of the effective mobility $\mu_{\text{eff}} = \sigma/en$ (Figure 2.1.17).

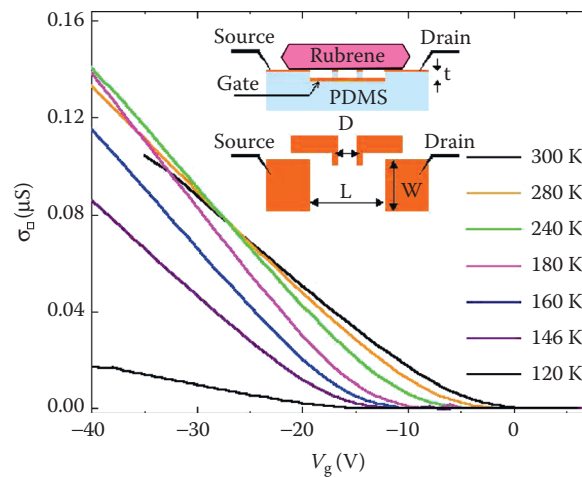


FIGURE 2.1.18 Sheet conductivity σ_0 of the "vacuum-gap" rubrene single-crystal OFET, AU: missing symbol. measured as a function of V_g at different T using the four-probe technique. (From Podzorov, V. et al., *Phys. Rev. Lett.*, 93, 086602, 2004.)

In the past, two signatures of the *intrinsic band-like polaronic conduction* have been observed in the bulk of ultrahigh-purity organic crystals in TOF measurements [19]. These signatures are the mobility increase with cooling below 300 K and a pronounced anisotropy of μ . The increase of μ_{eff} with cooling and the mobility anisotropy observed in OFETs in the temperature range 200–300 K (Figure 2.1.17) indicate that this regime corresponds to the intrinsic (i.e., not trap dominated) polaronic transport. (The effective mobility $\mu_{\text{eff}}(T)$ in this temperature range coincides with the intrinsic mobility of polarons $\mu_0(T)$.)

The rapid drop of μ_{eff} at $T \leq 160$ K and vanishing of the anisotropy indicate a crossover to the trap-dominated regime, where $\mu_{\text{eff}} < \mu_0$. Note that, for the device whose conductivity is shown in Figure 2.1.18, the density of shallow traps, $N_{\text{tr}}^{\text{sh}}$, which can be estimated from the linear temperature dependence of the threshold voltage, $V_{\text{g}}^{\text{th}}(T)$, is relatively low ($N_{\text{tr}}^{\text{sh}} \sim 10^{10} \text{ cm}^{-2}$). For devices with higher $N_{\text{tr}}^{\text{sh}}$, the crossover between the intrinsic and trap-dominated regimes occurs at higher temperatures. As a result, devices with $N_{\text{tr}}^{\text{sh}} \geq 10^{11} \text{ cm}^{-2}$ demonstrate an activated temperature dependence of μ_{eff} even at room temperature, and the effective mobility is smaller than μ_0 [29].

A better understanding of the intrinsic transport can be gained from the measurements of transverse (Hall) conductivity. In the Hall effect, a voltage across the conducting channel is induced by an application of a magnetic field (B) perpendicular to the channel (Figure 2.1.19). The origin of the Hall effect in a conventional band semiconductor is the *Lorentz force*, acting on a charge carrier propagating along the channel in a transverse magnetic field. This force is proportional to the microscopic velocity of the carrier (when it is moving between shallow traps). For the trapped carriers, Lorentz force is zero, and therefore trapped carriers do not contribute to

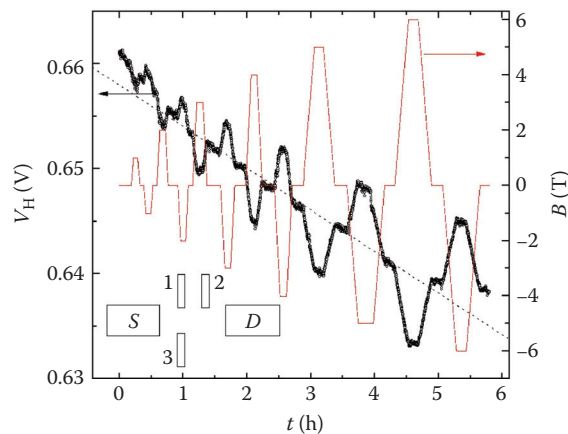


FIGURE 2.1.19 Hall effect in rubrene OFETs (the inset shows the contact geometry). Symbols: the Hall voltage, V_{H} , measured between the contacts 1 and 3; line: magnetic field, B , applied perpendicular to the channel. (From Podzorov, V. et al., *Phys. Rev. Lett.*, 95, 226601, 2005.)

Charge Carrier Transport in Single-Crystal Organic Field-Effect Transistors 53

the Hall signal. Hall measurements have the following important advantages compared to the longitudinal conductivity measurements:

The mobility determined from the Hall effect is the *intrinsic* (i.e., trap-independent) mobility $\mu_0(T)$, even if a considerable trapping occurs in the channel. Hall measurements allow for an independent determination of the density of instantaneously mobile charges and their intrinsic mobility μ_0 .

Observation of the classical (i.e., band) Hall effect strongly suggests a “band-like” motion of carriers as a fundamental conduction mechanism in small-molecule organic semiconductors, as opposed to the incoherent hopping. Indeed, in the hopping regime, conduction occurs via tunneling of charge carriers from site to site, and microscopic velocity cannot be introduced.

From the Hall data, the density of mobile carriers in the OFET’s channel can be directly determined for the first time, without the assumptions regarding the gate-channel capacitance C_i . Hall effect studies in other organic semiconductors (e.g., pentacene and tetracene) are highly desirable because most of the OFETs based on those materials still operate in the trap-dominated regime and the intrinsic mobilities at the surface of these semiconductors, $\mu_0(T)$, are unknown. The Hall measurements, however, are complicated by a very high sheet resistance of the conduction channel typical for OFETs, which often exceeds $10 \text{ M}\Omega/\text{square}$. For this reason, the first demonstration of the Hall effect appeared only recently, due to the high carrier mobility in rubrene [82,83].

The quantity n_H determined in the Hall measurements is the density of charges that are moving at any given moment of time (i.e., n_H coincides with n_{eff} given by Equation 2.1.6). The charges temporarily trapped in shallow traps do not contribute to the Hall voltage because the Lorentz force, proportional to the carrier velocity, is zero for these charges. Figure 2.1.20 shows the temperature dependence of n_H normalized to the density of charge carriers, n , field-induced in the channel above the threshold (determined using the FET capacitance C_i according to Equation 2.1.2). The ratio n_H/n is close to unity in the high-temperature (intrinsic) regime (see also Takeya et al. [83]) and decreases with cooling in the trap-dominated regime.

The mobility μ_H determined from the Hall effect measurements is the intrinsic, trap-free mobility μ_0 , even if the charge transport is significantly affected by trapping. Again, this reflects the fact that the Hall voltage is proportional to the velocity of charge carriers moving between the trapping events. Therefore, in contrast to μ_{eff} , Hall mobility μ_H continues to increase with decreasing T even at low temperatures, at which the longitudinal conduction is in the trap-dominated regime. In the experiment of Podzorov et al. [82], the increase of μ_H with cooling could be traced down to $\sim 150 \text{ K}$; at lower temperatures, the Hall measurements were hindered by a rapid enhancement of the $1/f$ noise of the channel conductivity with T decreasing below the crossover to the trap-dominated regime. Observation of a “band” Hall effect suggests that the charge transport on the surface of rubrene single crystals occurs via delocalized states over the whole studied temperature range (for a discussion of the Hall effect, see, for example, Pope and Swenberg [7]).

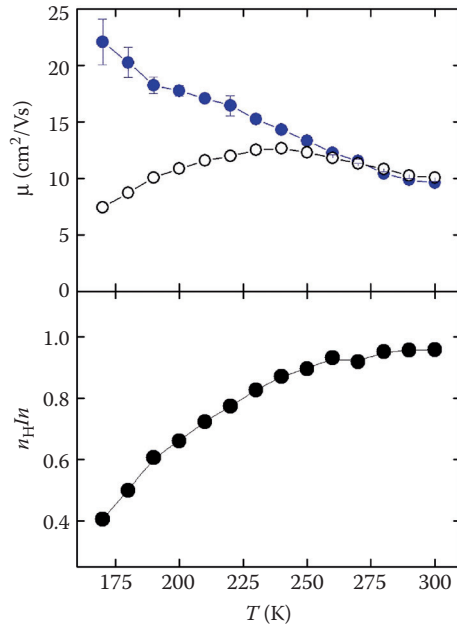


FIGURE 2.1.20 Upper panel: the temperature dependences of the Hall mobility, μ_H , (solid circles) and the effective mobility, μ_{eff} , extracted from the conventional FET equations — that is, from the longitudinal FET conductivity and the density of charges, n , field induced above the threshold (Equation 2.1.2) (open circles). Lower panel: the temperature dependence of the ratio of the Hall carrier density, n_H , to the density n . (From Podzorov, V. et al., *Phys. Rev. Lett.*, 95, 226601, 2005.)

2.1.3.5 COMPARISON WITH THE HOLSTEIN–PEIERLS MODEL AND TRANSPORT MEASUREMENTS IN THE BULK OF ORGANIC CRYSTALS

A microscopic theory of finite-density charge transport on the surface of organic crystals has yet to be developed. However, several models have been proposed for the analysis of low-density (i.e., single particle) intrinsic transport in the bulk of organic crystals observed in TOF experiments by Norbert Karl et al. [19,84] and, more recently, in the space charge limited current measurements by Jurchescu et al. [85] and de Boer et al. Signatures of the intrinsic band-like transport have also been observed in the experiments on subpicosecond transient photoconductivity [86,87]. The results of these experiments can be interpreted as an increase of the mobility with decreasing temperature ($\mu \propto T^{-\gamma}$, with $\gamma \sim 0.3$), under the assumption that the efficiency of carrier photogeneration is temperature independent. Note, however, that in these experiments, unlike the transport measurements, hot (i.e., nonthermalized) optically excited carriers are probed.

The *ab initio* calculations of polaron mobility on the basis of the Holstein–Peierls model including a nonlocal electron-lattice coupling (Hannewald and Bobbert [12,13]; see references to earlier work therein) reproduced the temperature-depen-

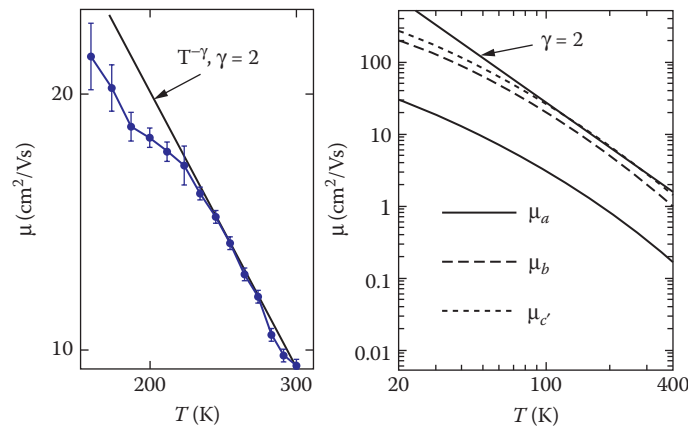


FIGURE 2.1.21 Left: the Hall mobility versus T for a rubrene OFET in the double-log scale (compare with Figure 2.1.20). (From Podzorov, V. et al., *Phys. Rev. Lett.*, 95, 226601, 2005.) Right: the calculated T -dependences of the hole mobility for different crystallographic directions in tetracene. (From Hannewald, K. and Bobbert, P. A., *AIP Conf. Proc.* 772, 1101, 2005.)

dent mobility measured in single crystals of naphthalene along different crystalline directions [19,84]. According to this theory, the mobility for p - and n -type carriers in polyacenes should exhibit a “metallic” behavior for all T , up to room temperature (with the exception of n -type carriers in naphthalene). Similar behavior was predicted by a semiclassical model developed for the high-temperature regime by Troisi and Orlandi [88].

Interestingly, the theory of Hannewald and Bobbert also agrees semiquantitatively with the temperature dependence of μ observed in the “intrinsic” regime for rubrene OFETs. Fitting the Hall mobility data for rubrene OFETs (Figure 2.1.21) by power-law dependence $\mu(T) \sim T^{-\gamma}$ yields the value $\gamma \sim 2$ at high temperatures, which agrees with the calculations for anthracene and tetracene. Similar temperature dependences of the hole mobility ($\mu \sim T^{-\gamma}$ with $\gamma \approx 2$ –2.9) were obtained in the TOF experiments with bulk ultrapure crystals of naphthalene and perylene by Karl et al. [84] and in the SCLC measurements with ultrapure pentacene single crystals by Jurchescu et al. (Figure 2.1.22) [85].

2.1.3.6 TUNING THE INTERMOLECULAR DISTANCE

Availability of OFETs operating in the intrinsic conduction regime enables studies of the dependence of polaronic mobility on intermolecular distance of the crystal lattice, d . Note that the variations of the polaron mobility with d can only be observed in the intrinsic regime, where trapping is not dominating (i.e., only when $\tau_{tr} \ll \tau$). Recently, the effect of continuous “tuning” of the intermolecular distance on mobility was observed in rubrene single-crystal OFETs with application of high pressure, P , of up to 0.5 GPa (Figure 2.1.23) [89]. The estimates show that, at such pressure, the intermolecular distance is decreased by $\Delta d \sim 1.5\%$. It was observed that the mobility increased linearly with pressure over the range 0–0.5 Gpa. This observation

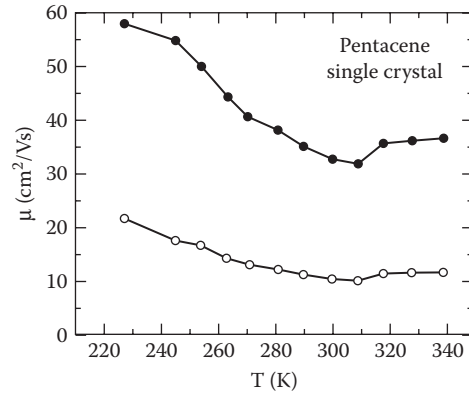


FIGURE 2.1.22 Temperature dependence of the hole mobility in ultrapure pentacene crystals extracted from the SCLC measurements. The open symbols correspond to the values of μ calculated under an assumption of uniform current flow across the crystal thickness; solid symbols — taking into account the anisotropy of conductivity in pentacene. Below room temperature, the mobility increases with decreasing T as $\mu \sim T^{-\gamma}$, where $\gamma \approx -2.4$. (From Jurchescu, O. D. et al., *Appl. Phys. Lett.*, 84, 3061, 2004.)

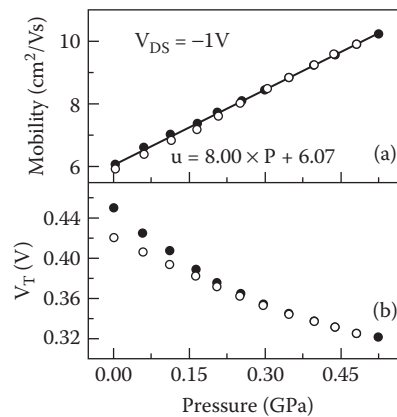


FIGURE 2.1.23 Pressure dependence of the field-effect mobility (a) and the threshold voltage (b) in single-crystal rubrene OFETs (solid and open symbols correspond to the increasing and decreasing pressure). (From Rang, Z. et al., *Appl. Phys. Lett.*, 86, 123501, 2005.)

is in line with the expectations based on polaronic models: The mobility, which is proportional to the square of the transfer integral for the Holstein type of small polaron, should depend linearly on pressure for small variations of the intermolecular distance [89].

2.1.3.7 SURFACE VERSUS BULK TRANSPORT

Semiquantitative agreement between the carrier mobilities obtained from OFET measurements and the models developed for the bulk transport may suggest that

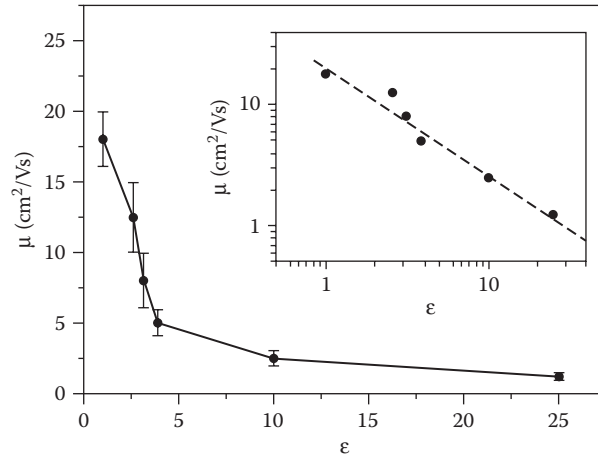


FIGURE 2.1.24 The dependence of the mobility of *p*-type carriers in rubrene single-crystal OFETs on the dielectric constant of the gate insulator, ϵ . The bars represent the spread in the mobility values. (From Stassen, A. F. et al., *Appl. Phys. Lett.*, 85, 3899, 2004.)

there are no differences between polaronic conduction in the bulk and at the surface of organic crystals. However, recent experiments with single-crystal OFETs [57] revealed strong dependence of the carrier mobility on the dielectric constant ϵ of the gate insulator. Figure 2.1.24 shows that the room-temperature mobility in these devices varies approximately as ϵ^{-1} over a wide range $\epsilon = 1 - 25$.

Earlier, a similar trend was observed for the organic TFTs based on soluble polymers [90]. (For a recent review of gate dielectrics, including inorganic, polymeric and ultrathin self-assembled molecular layers, see Facchetti et al. [91]). Note that in single-crystal OFETs these observations cannot be attributed to a difference in morphology of the organic semiconductor, since the crystals used to obtain the data in Figure 2.1.24 were grown under the same conditions, irrespective of the gate insulator. Thus, the observed $\mu(\epsilon)$ trend indicates that the mobility of charges at the interface between an organic semiconductor and an insulator is the property of the interface (a combination of the semiconductor and insulator), rather than the organic material alone.

It has been predicted that the intrinsic mobility of polarons at an interface with a highly polarizable dielectric may decrease due to an increase of the effective polaronic mass [25]. Though this prediction is in line with the experimental observations, it is worth noting that the mobilities measured in the high- ϵ OFETs by Stassen et al. [23] and de Boer et al. [57] might be trap dominated and therefore could significantly differ from the corresponding intrinsic $\mu_0(\epsilon)$ (e.g., because of a larger densities of shallow traps at interfaces with greater ϵ). More experiments are needed for better understanding of $\mu(\epsilon)$ dependence and differences between the bulk and interfacial transport in organic semiconductors. For example, measurements of the Hall mobility, μ_H , in high- ϵ OFETs could shed more light on the intrinsic $\mu_0(\epsilon)$ dependence.

Development of single-crystal OFETs allows studies of the charge transport in organic semiconductors in a much broader range of charge carrier densities, inaccessible with the bulk time of flight of SCLC measurements. Approximately one

carrier per molecule at the interface can be induced using high- ϵ gate dielectrics. At such density, polaron–polaron interactions may play a significant role, which can lead to formation of novel electronic phases. Indeed, it is known that at a sufficiently high density of chemically doped carriers, the potassium-doped fullerene K_xC_{60} exhibits superconductivity ($x = 3$) [92] and a Mott–Hubbard insulating state ($x = 4$) [93].

In rubrene single-crystal OFETs, stable operation at a carrier density $n = 5 \cdot 10^{13} \text{ cm}^{-2}$ (corresponding to 0.1 carriers per molecule) has been demonstrated by using high-quality Ta_2O_5 gate dielectric [23]. With a breakdown field of $E_B = 6.6 \text{ MV/cm}$ and a dielectric constant of $\epsilon = 25$, this insulator should allow reaching even higher density of charge carriers, $\sim 10^{14} \text{ cm}^{-2}$. However, the presence of moderate leakage currents inducing irreversible degradation in the devices currently prevents the operation of Ta_2O_5 gate insulators too close to the breakdown.

In another interesting approach for achieving high carrier densities in OFETs ($>10^{15} \text{ cm}^{-2}$), a conventional gate dielectric is replaced with a polymer electrolyte [24,94]. In OFETs with high- ϵ dielectrics and with polyelectrolytes, a nonmonotonic dependence of channel conductivity on charge carrier density has been observed, with a maximum of conductivity at $\sim 10^{15}$ charges per square centimeter. This observation might indicate filling of the conduction band in these narrow-band semiconductors when the density of field-induced carriers approaches \sim one carrier per molecule. These field-effect experiments are in line with the experiments on chemical doping of organic thin films, where the insulator–metal–insulator transition has been observed with increasing dopant concentration.

At the current stage of the exploration of high carrier density regime in OFETs, reproducible fabrication of high-capacitance devices has been achieved, and notable deviations from the standard device characteristics have been observed at high carrier densities [23,94]. Despite the first successful demonstrations, much more work is needed in this direction in order to distinguish intrinsic effects from the effects that might be associated with defects and interface morphology. For example, at these large densities, molecular steps at the crystal surface could significantly affect the longitudinal transport [95].

2.1.3.8 PHOTOINDUCED PROCESSES IN SINGLE-CRYSTAL OFETs

Despite the fact that organic transistors are intended to operate back to back with organic light-emitting diodes (OLEDs) as switches for display pixels (see, for example, Forrest), surprisingly little is known about photoinduced effects in OFETs. (In thin-film organic transistors, light illumination produces a weak photoconductivity response [96] and reduces the threshold voltage [97].) One of the explanations for this paradox is that thin-film organic transistors are ill suited for fundamental research in this direction because of a large density of defects that could trap light-generated carriers and/or act as recombination centers. By contrast, single-crystal organic transistors with a low density of defects provide a unique opportunity to investigate intrinsic photoinduced processes at organic surfaces and interfaces. Better understanding of these phenomena is crucial for optimization of organic electronic devices.

Several novel light-induced effects have been recently observed using the single-crystal OFETs as an experimental platform. In experiments with back-gated rubrene OFETs [98], switching of devices from OFF state into a persistent ON state by a short pulse of light was observed. The effect is caused by interplay between the surface built-in conducting channel and nonequilibrium carriers photogenerated in the bulk. The self-latching character of this effect opens an opportunity for using these devices as optically addressed memory elements.

The standard, front-gate transistor geometry with a transparent parylene insulator and a semitransparent gate electrode allows one to illuminate the critical semiconductor–insulator interface with photons and to study the OFET’s response (Figure 2.1.25). Light- and gate-controlled shift of the field-effect threshold voltage has been observed in these experiments. The effect is caused by the photoinduced charge transfer across the interface between an ordered semiconductor and a disordered polymeric gate insulator [55]. This class of interfaces is especially important for a wide range of all-organic flexible devices.

When the interface is illuminated with photons of energy greater than the absorption edge of the organic semiconductor, nonequilibrium charges are generated near the interface. Driven by the transverse gate electric field at the interface, these carriers are transferred into the polymer and become immobilized by its deep traps. Either holes or electrons can be transferred, depending on the sign of the gate voltage applied during the illumination, V_g^{illum} . This causes a nonvolatile shift of the field-effect threshold in OFETs that can be used for a direct measurement of the charge transfer rate. Potential applications of this effect range from organic photosensors and optical memory devices to lithography-free patterning of the conduction channel in OFETs with light exposure.

More studies using optical and nonlinear optical tools are required to investigate and characterize photoexcitations and charge transport in organic single crystals and related devices. Time-resolved photoluminescence and photocurrent studies, for example, can provide information on charge-carrier excitation mechanisms, their mobility, and lifetimes. In addition, such optical studies are complementary to the efforts on design, fabrication, and studies of organic electronic devices. For instance, the absorption edge in the spectral characteristics of rubrene single crystals, shown in Figure 2.1.26 [99], coincides with the “red boundary” of the photoinduced threshold shift in rubrene OFETs demonstrated in Figure 2.1.25. This indicates that the previously mentioned effect is indeed associated with the photocarriers generated in the organic semiconductor.

AU: no color plates in book.

2.1.4 DEFECTS AT THE SURFACE OF ORGANIC CRYSTALS

Because of the small size of polarons in molecular crystals, the conduction channel in organic transistors extends in the transverse direction for only a few molecular layers [20–22]. For the same reason, polarons interact strongly with chemical impurities and structural defects. As a result, polaronic transport in organic OFETs is very sensitive to the morphology of semiconductor surface and to the presence of

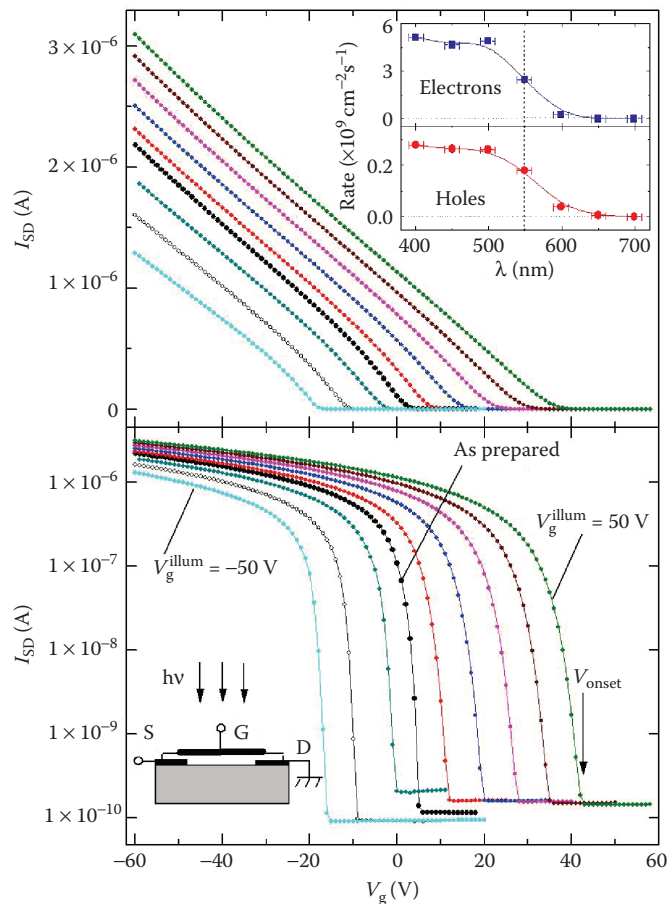


FIGURE 2.1.25 Gate controlled photoinduced shift of the onset voltage in OFET caused by the photoinduced charge transfer at the interface. Linear (top) and semilog (bottom) plots of $I_{SD}(V_g)$ of a rubrene OFET, measured in the dark after illumination of the device at fixed applied gate voltages, V_g^{illum} . The top inset shows that the effect exhibits a “red boundary.” The bottom inset schematically shows the device geometry. (From Podzorov, V. and Gershenson, M. E., *Phys. Rev. Lett.*, 95, 016602, 2005.)

AU: no color inserts in book.

electronic defects at the semiconductor–insulator interface. Carrier trapping, charge doping, molecular reorientation, dipole formation, and a range of possible chemical interactions are among the many phenomena that can occur at the semiconductor–insulator interface and they can affect the electrical characteristics of single-crystal OFETs.

For example, the localized electronic states within the HOMO–LUMO gap impair the performance of the field-effect transistors by increasing the field-effect threshold voltage and reducing the effective mobility of charge carriers [100]. The surface density of electronic defects in high-quality single-crystal OFETs can be less than 10^{10} cm^{-2} [38], which corresponds to the interdefect distances $\sim 0.1 \mu\text{m}$.

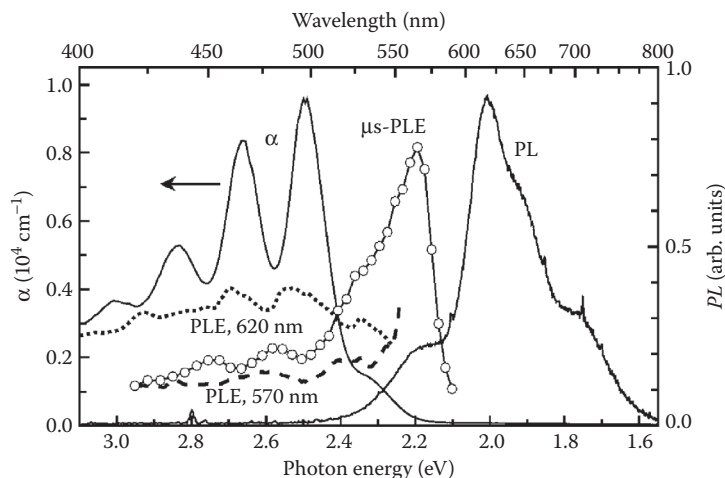


FIGURE 2.1.26 *b*-Polarized absorption spectrum (α), photoluminescence spectrum (PL), cw luminescence excitation spectrum (PLE) — monitored at 570 nm (dashed line) and 620 nm (dotted line) — and excitation spectrum of the microsecond luminescence transient induced by *b*-polarized light (open circles) in rubrene single crystals. (From Najafov, H. et al., *Phys. Rev. Lett.*, 96, 056604, 2006.)

This low density of surface defects is the major factor that determines the record performance of single-crystal OFETs and enables exploration of the fundamental limits of charge carrier transport in organic materials. In addition, these devices provide an efficient tool for studying the polaron-defect interactions. This section focuses on defects that can be formed in the process of crystal growth, OFET fabrication, and as a result of the interaction with ambient environment.

2.1.4.1 BULK AND SURFACE ELECTRONIC DEFECTS IN ORGANIC CRYSTALS

The density of electronic defects in organic crystals might significantly vary depending on the crystal growth methods. Niemax et al. performed TOF mobility measurements and concluded that vapor-grown tetracene single crystals are characterized with higher quality than vapor-Bridgman-grown crystals [44]. The distribution of localized states in the bulk of organic crystals can be probed by photoconductivity [6,7,101] and space charge limited current (SCLC) measurements [8,41,85]. Figure 2.1.27 shows the photocurrent spectra obtained at room temperature for pentacene crystals in recent experiments by Lang et al. [101]. These data indicate a broad (~ 1 eV wide) *amorphous-like* distribution of localized states within the HOMO–LUMO gap near the HOMO edge, which resembles the exponential “tails” of valence and conduction bands in strongly disordered inorganic semiconductors. This observation raises a question of the origin of such amorphous-like distribution of localized states because it is not in line with the typically high crystallinity of vapor-grown organic crystals.

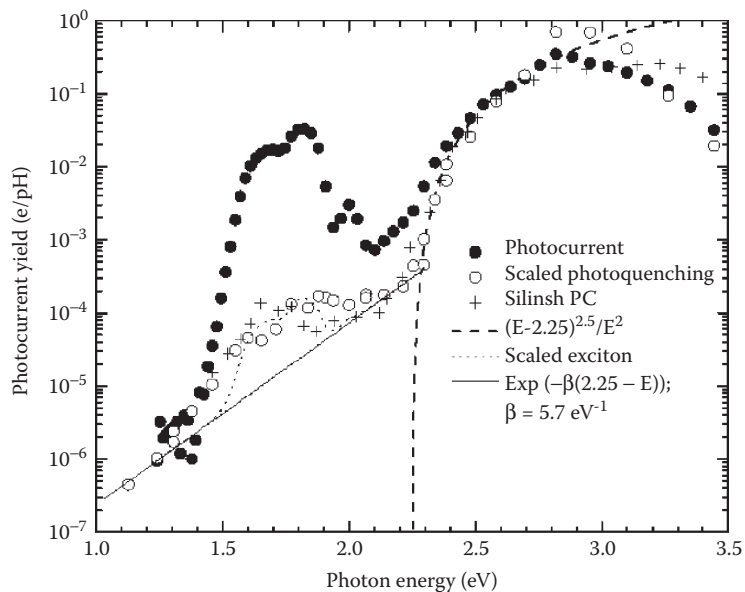


FIGURE 2.1.27 Energy distribution of localized states in HOMO-LUMO gap of single-crystal pentacene. The HOMO band corresponds to energies > 2.25 eV. (From Lang, D. V. et al., *Phys. Rev. Lett.*, 93, 086802, 2004.)

The large density of in-gap trap states in these highly purified pentacene crystals might originate from the tendency of pentacene to react with oxygen and water from the environment. Such sensitivity to gases and vapors has been used in TFT-based gas-sensing applications; it is argued that diffusion of molecules to the conduction channel along the grain boundaries in thin films is crucial for the sensing effect [102,103]. Recently, however, based on infrared absorption, mass spectrometry and SCLC measurements, it was suggested that gas molecules from the ambient can diffuse even into the single crystals of pentacene as deeply as tens of microns, creating doping centers associated with O_2 and traps associated with H_2O molecules [104].

In particular, it was shown that 6,13-pentacenequinone (the product of pentacene oxidation) forms electronic defects in pentacene and careful purification of the commercially available material by vacuum sublimation is required to achieve a significant reduction of this impurity [85]. Following an extensive purification procedure, it has been estimated from SCLC measurements that the bulk density of traps in ultrapure pentacene crystals can be as low as $\sim 2 \cdot 10^{11} \text{ cm}^{-3}$. However, the density of traps can be considerably larger close to the crystal surface, which is normally exposed to the environment during the OFET assembly.

Rubrene also reacts with oxygen and forms rubrene endoperoxide in the process of *self-sensitized photo-oxidation* [98,105]. Oxidation of rubrene is restricted to a thin surface layer [106]. The role of the surface endoperoxide in the charge transport properties of rubrene OFETs is still unclear and more work is needed in this direction. For example, surface endoperoxide might help to preserve the conduction channel

from interaction with ambient gases. Recent experiments with the “air-gap” rubrene single-crystal OFETs, in which the conduction channel is fully exposed to environmental species, have shown that the channel conductivity is not sensitive to the presence of such gases as O_2 , H_2O , N_2 , and H_2 , and even to the saturated vapors of acetone and propanol [56]. This remarkable stability of rubrene OFETs is in a sharp contrast to typically fast degradation of pentacene devices.

2.1.4.2 DENSITY OF DEFECTS IN SINGLE-CRYSTAL OFETs

Photoconductivity and SCLC experiments have been used to obtain information on localized states in the bulk of organic crystals. However, information about the surface states that are relevant to the OFET operation is still very limited. Fortunately, calculation of several basic OFET parameters does not require a detailed knowledge of the trap spectrum. For example, the field-effect threshold voltage is determined by the total density of deep traps N_{tr}^{deep} :

$$V_g^{th} = eN_{tr}^{deep}/C_i \quad (2.1.7)$$

Note that the density of deep traps is a temperature-dependent quantity: The borderline between deep and shallow traps shifts closer to the band edge with decreasing T , and any temperature-driven changes of the bandwidth of organic semiconductor, W , would affect the density and spectrum of traps.

The temperature dependence of the threshold voltage of the p -type “air-gap” rubrene single-crystal OFETs is shown in Figure 2.1.28 [38]. At room temperature, the threshold voltage is small; it corresponds to the deep-trap density on the pristine crystal surface $\sim 7 \times 10^9 \text{ cm}^{-2}$. With cooling, the concentration of deep traps increases quasilinearly up to $2 \times 10^{10} \text{ cm}^{-2}$ at 150 K. Assuming that the thickness of the conduction channel does not exceed one or two molecular layers, the three-dimensional density of traps near the surface at 300 K can be estimated as $\sim 2 \times 10^{16} \text{ cm}^{-3}$.

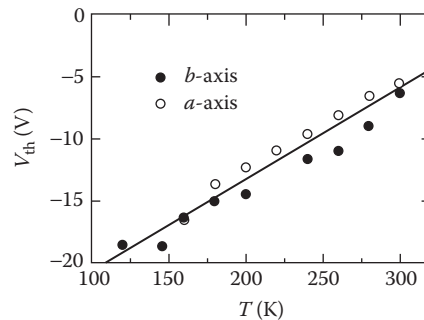


FIGURE 2.1.28 Temperature dependence of the threshold voltage of a rubrene OFET measured along a and b axes in the basal plane of an orthorhombic single crystal. (From Podzorov, V. et al., *Phys. Rev. Lett.*, 93, 086602, 2004.)]

Defects in the molecular materials that act as traps can also be generated during the device operation. Creation of such defects has been observed in tetracene, perylene, and rubrene single-crystal transistors with Ta₂O₅ gate dielectric at large gate electric fields; this results in irreversible decrease of I_{SD} of an operating OFET [23]. Systematic experiments with differently prepared gate dielectrics have shown that the defects originate from a leakage current through the gate insulator. The leakage at high gate fields induces degradation of the molecular material by creating a large density of deep traps, which causes a substantial increase of the threshold voltage and a decrease of the source-drain current. The precise nature of the leakage-induced traps has not been established yet, and more work is necessary to address this issue.

2.1.4.3 SINGLE-CRYSTAL OFETs AS TOOLS TO STUDY OF SURFACE DEFECTS

It is well known that x-rays create defects in organic semiconductors by breaking the molecules and creating new chemical species. Using this effect, Podzorov et al. [38] controllably increased the defect density in rubrene single crystals and studied how this process affected the charge transport in the corresponding air-gap OFETs (Figure 2.1.29). The x-ray treatment increases the field-effect threshold and thus the density of deep traps. Interestingly, the mobility, which is proportional to the slope of $I_{SD}(V_g)$, and its temperature dependence $\mu(T)$ were not affected by x-ray irradiation. This suggests that the deep traps, being filled above the threshold, do not scatter mobile polarons.

The defects in OMCs can be induced not only during the crystal growth and OFET fabrication, but also as a result of handling of crystals in a high-vacuum

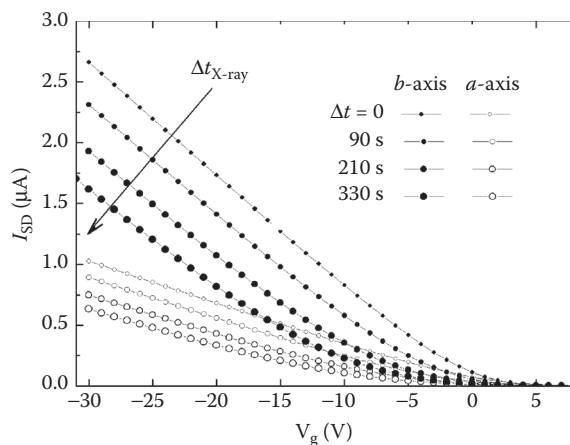


FIGURE 2.1.29 The effect of a gradual increase of x-ray exposure on the transconductance characteristics of rubrene OFET. Upon increasing the x-ray dose, the threshold voltage increases, while the mobility remains unchanged. (From Podzorov, V. et al., *Phys. Rev. Lett.*, 93, 086602, 2004.)]

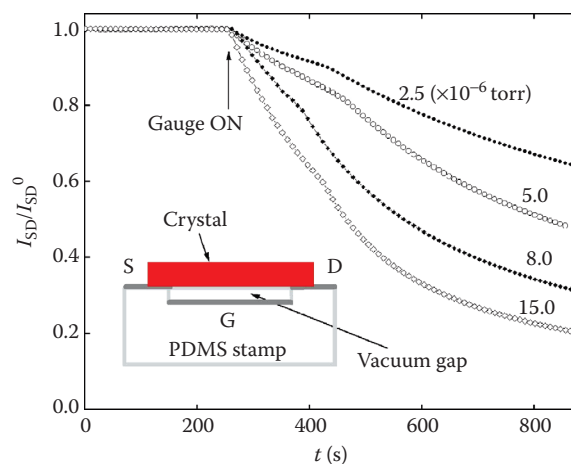


FIGURE 2.1.30 Demonstration of the “gauge effect”: time evolution of I_{SD} in a vacuum-gap OFET (the channel is exposed to the environment), operating in a vacuum chamber at different pressures: 2.5, 5, 8, and 15×10^{-6} torr. The hot-cathode high-vacuum gauge was turned on at $t = 250$ s. (From Podzorov, V. et al., *Appl. Phys. Lett.*, 87, 093505, 2005.)

environment. In the experiments with “vacuum-gap” single-crystal OFETs, where the conduction channel is exposed to environmental agents, it was observed that deep and shallow traps are generated at the organic surface in vacuum due to interactions with chemically active species produced by high-vacuum gauges or hot surfaces such as resistively heated filaments and evaporation sources — the “gauge effect” [56].

Figure 2.1.30 shows that a rapid decrease of the source-drain current of an operating device occurs when a high-vacuum gauge is turned on. The effect has been attributed to the interaction of organic surface with electrically neutral free radicals. These species can be produced at the surface of hot filaments in high-vacuum gauges in a process of *hydrocarbon cracking* that has relatively low activation energy, $E_a \sim 2.5$ eV (240 kJ/mol). Clearly, minimization of the damage induced through this mechanism is important for optimizing the performance of a wide range of thin-film organic devices that are fabricated or characterized in high vacuum.

The experiments described earlier demonstrate the great potential of single-crystal OFETs as a diagnostic tool for studies of phenomena affecting the performance of organic transistors, as well as for studying surface-limited reactions in organic semiconductors.

2.1.5 CONCLUSION

Within a short four-year span, the development of single-crystal organic field-effect transistors significantly advanced our understanding of transport processes on organic surfaces and shed light on fundamental limits of organic devices (Figure 2.1.31). Due to their reproducibility, single-crystal OFETs enabled the systematic study of polaronic effects in a broad range of parameters, bridging the gap between

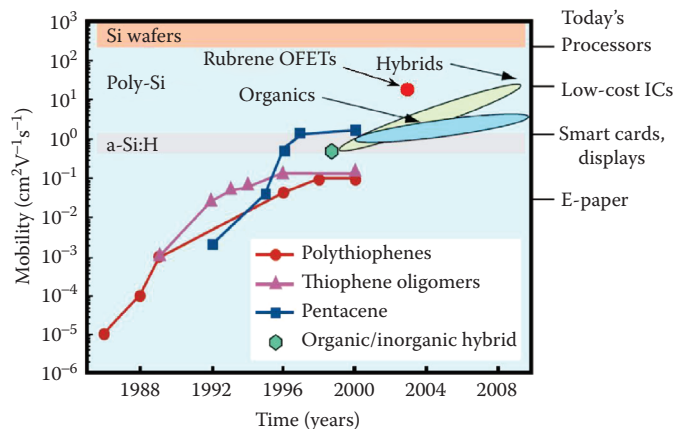


FIGURE 2.1.31 Realization of charge transport not limited by static disorder is crucial for better understanding of the fundamental limits of organic electronics. The red dot on the figure borrowed from the *IBM Journal for Research and Development*, January 2001, represents the room-temperature mobility in rubrene single-crystal OFETs, the only “intrinsic” mobility found in the field-effect experiments to date. (From Shaw, J. M. and Seidler, P. F., *IBM J. Res. Dev.* 45, 3, 2001.)

the fundamental research on ultrapure bulk crystals and applied research on thin-film transistors. The potential of single-crystal OFETs goes far beyond the fundamental research on polaronic transport. These devices are very useful for studies of surface reactions and defect formation mechanisms on organic surfaces [56], light-induced effects in organic semiconductor devices [55,98], and work-function engineering with self-assembly monolayers [107].

Although the single polaron problem was one of the early subjects of interest for condensed matter physics, polaronic conduction at a finite density remains a complex and poorly understood topic even these days, with many open questions. The organic single-crystal OFETs represent a unique tool to address these questions in a class of materials relevant for the emerging plastic electronics.

For example, the band structure calculations that can be found in the literature for different molecular crystals do not include the interaction between the electronic and vibrational degrees of freedom, so it remains to be understood how polaronic effects affect the density of states and the width of HOMO and LUMO bands. These quantities are expected to exhibit nontrivial temperature dependences due to the strongly T -dependent parameters of polarons in Holstein-like models.

Another important issue is the transport across metal/organic interfaces [58]. For inorganic semiconductors, our understanding of contacts with metals is based on the concept of Schottky barrier. For organic semiconductors based on small molecules, the experimental data remain, to a large extent, unclear and irreproducible because of the poor interface control. Because of the narrow bandwidth of organic semiconductors and weak van der Waals molecule–molecule and molecule–metal coupling, the behavior of metal/organic interfaces is likely to be qualitatively different from that of their inorganic counterparts. Due to their great reproducibility, the single-

Charge Carrier Transport in Single-Crystal Organic Field-Effect Transistors 67

crystal OFETs have a potential to clarify the situation in this field. Note that these questions are directly related to the issue of contact resistance in organic transistors that impose serious limitations on the downscaling of organic thin-film devices [108].

Increasing the purity of organic crystals and reducing the contact resistance in OFETs is another challenging direction of future experimental work, which will help to extend the temperature range where the intrinsic polaronic transport can be studied. The development of more advanced techniques for purification of molecular materials will enable the expansion of the intrinsic transport regime to much lower temperatures, where the effects of quantum statistics and polaron–polaron interactions should become experimentally accessible.

The development of high-quality single-crystal OFETs will be crucial for the comparative studies of different molecular materials and, in particular, for testing the transport properties of newly synthesized molecular compounds in their crystalline form. Such tests are essential for supporting the effort to synthesize novel organic molecules that could form high-mobility ordered aggregates from solutions — one of the most attractive goals of research in organic electronics. Although some soluble derivatives of linear acenes and the corresponding OFETs have been demonstrated, much more experimental work needs to be done to optimize these systems for solubility and charge carrier mobility [45,109,110]. Systematic effort in this direction will require the investigation of a much broader variety of new molecular compounds.

Single-crystal OFETs provide a unique tool for the express analysis of transport characteristics of new molecular materials with defect densities much smaller than those in TFTs. Therefore, even though large-scale applications will ultimately rely on thin films, research on single-crystal OFETs can play an important role in the material selection for applied devices. The case of rubrene perfectly illustrates this point. The unprecedented quality of OFETs based on vapor-grown rubrene crystals has stimulated work on the deposition of rubrene thin-films from solution: Stingelin-Stutzmann et al. have recently demonstrated solution-processed rubrene TFTs with high mobility (up to $0.7 \text{ cm}^2/\text{Vs}$ at room temperature) [111].

ACKNOWLEDGMENTS

I am indebted to all my coworkers and collaborators for their significant contributions to the work presented here, especially to M. E. Gershenson, A. F. Morpurgo, J. A. Rogers, D. Fichou, I. Biaggio, H. Najafov, M. F. Calhoun, V. M. Pudalov, E. Loginova, R. W. I. de Boer, E. Menard, V. C. Sundar, J. Zaumseil, Z. Rang, P. P. Ruden, M. I. Nathan, C. D. Frisbie, O. Ostroverkhova, B. Yakshinskiy, T. Madey, Y. Chabal and E. Garfunkel. VP at Rutgers University is supported in part by the NSF grants DMR-0405208 and ECS-0437932.

REFERENCES

1. Shaw, J. M., and Seidler, P. F., Organic electronics: Introduction, *IBM J. Res. Dev.* 45, 3, 2001.

2. Hoppe, H., and Sariciftci, N. S., Organic solar cells: An overview, *J. Mater. Res.* 19, 1924, 2004.
3. Forrest, S. R., The path to ubiquitous and low cost organic electronic appliances on plastic, *Nature* 428, 911, 2004.
4. Katz, H. E., Recent advances in semiconductor performance and printing processes for organic transistor-based electronics, *Chem. Mater.* 16, 4748, 2004.
5. Agranovich, V. M., and Bassani, G. F., *Electronic excitations in organic based nanostructures*, Elsevier Academic Press, New York, 2003.
6. Silinsh, E. A., and ápek, V., *Organic molecular crystals: Interaction, localization, and transport phenomena*, AIP Press, New York, 1994.
7. Pope, M., and Swenberg, C. E., *Electronic processes in organic crystals and polymers*, 2nd ed., Oxford University Press, New York, 1999.
8. Kao, K. C., and Hwang, W., *Electrical transport in solids*, vol. 14, Pergamon Press, New York, 1981.
9. Holstein, T., Polaron motion. II. "Small" polaron, *Ann. Phys.*, 8, 343, 1959.
10. Emin, D., Small polarons, *Phys. Today*, 35, 34, 1982.
11. Troisi, A., Orlandi, G., and Anthony, J. E., Electronic interactions and thermal disorder in molecular crystals containing cofacial pentacene units, *Chem. Mater.* 17, 5024, 2005.
12. Hannewald, K., and Bobbert, P. A., *Ab-initio* theory of charge-carrier conduction in ultrapure organic crystals, *Appl. Phys. Lett.* 85, 1535, 2004.
13. Hannewald, K., and Bobbert, P. A., *Ab-initio* theory of charge transport in organic crystals, *AIP Conf. Proc.* 772, 1101, 2005.
14. Wu, M. W., and Conwell, E. M., Transport in α -sexithiophene films, *Chem. Phys. Lett.*, 266, 363, 1997.
15. Deng, W.-Q., and Goddard, W. A., Predictions of hole mobilities in oligoacene organic semiconductors from quantum mechanical calculations, *J. Phys. Chem. B*, 108, 8614, 2004.
16. Kenkre, V. M. et al., Unified theory of the mobilities of photoinjected electrons in naphthalene, *Phys. Rev. Lett.*, 62, 1165, 1989.
17. da Silva Filho, D. A., Kim, E.-G., and Bredas, J.-L., Transport properties in the rubrene crystal: Electronic coupling and vibrational reorganization energy, *Adv. Mater.* 17, 1072, 2005.
18. Fratini, S., and Ciuchi, S., Dynamical mean-field theory of transport of small polarons, *Phys. Rev. Lett.*, 91, 256403, 2003.
19. Karl, N., Charge-carrier mobility in organic crystals, in *Organic electronic materials*, eds. Farchioni, R., and Grosso, G., pp. 283–326, Springer-Verlag, Berlin, 2001.
20. Dodabalapur, A., Torsi, L., and Katz, H. E., Organic transistors: Two-dimensional transport and improved electrical characteristics, *Science*, 268, 270, 1995.
21. Dinelli, F. et al., Spatially correlated charge transport in organic thin film transistors, *Phys. Rev. Lett.*, 92, 116802, 2004.
22. Kiguchi, M. et al., Electric-field-induced charge injection or exhaustion in organic thin film transistor, *Phys. Rev. B*, 71, 035332, 2005.
23. de Boer, R. W. et al., Influence of the gate leakage current on the stability of organic single-crystal field-effect transistors, *Appl. Phys. Lett.*, 86, 032103, 2005.
24. Panzer, M. J., and Frisbie, C. D., Polymer electrolyte gate dielectric reveals finite windows of high conductivity in organic thin film transistors at high charge carrier densities, *J. Am. Chem. Soc.*, 127, 6960, 2006.
25. Houili, H., Picon, J. D., Bussac, M. N., and Zuppiroli, L., Polarization effects in the channel of an organic field-effect transistor, *cond-mat*, 0510751, 2005.

Charge Carrier Transport in Single-Crystal Organic Field-Effect Transistors 69

26. Riordan, M., and Hoddeson, L., *Crystal fire: The birth of information age*, W. W. Norton & Co., New York, 1997.
27. Horowitz, G., Organic thin film transistors: From theory to real devices, *J. Mater. Res.*, 19, 1946, 2004.
28. Nelson, S. F., Lin, Y.-Y., Gundlach, D. J., and Jackson, T. N., Temperature-independent transport in high-mobility pentacene transistors, *Appl. Phys. Lett.*, 72, 1854, 1998.
29. Podzorov, V., Pudalov, V. M., and Gershenson, M. E., Field-effect transistors on rubrene single crystals with parylene gate insulator, *Appl. Phys. Lett.*, 82, 1739, 2003.
30. Podzorov, V. et al., Single-crystal organic field effect transistors with the hole mobility $\sim 8 \text{ cm}^2/\text{V s}$, *Appl. Phys. Lett.*, 83, 3504, 2003.
31. de Boer, R. W. I., Klapwijk, T. M., and Morpurgo, A. F., Field-effect transistors on tetracene single crystals, *Appl. Phys. Lett.*, 83, 4345, 2003.
32. de Boer, R. W. I. et al., Organic single-crystal field-effect transistors, *Phys. Stat. Sol.*, 201, 1302, 2004.
33. Takeya, J. et al., Field-induced charge transport at the surface of pentacene single crystals: A method to study charge dynamics of two-dimensional electron systems in organic crystals, *J. Appl. Phys.*, 94, 5800, 2003.
34. Butko, V. V. et al., Field-effect transistor on pentacene single crystal, *Appl. Phys. Lett.*, 83, 4773, 2003.
35. Sundar V. C. et al., Elastomeric transistor stamps: Reversible probing of charge transport in organic crystals, *Science*, 303, 1644, 2004.
36. Goldmann, C. et al., Hole mobility in organic single crystals measured by a “flip-crystal” field-effect technique, *J. Appl. Phys.*, 96, 2080, 2004.
37. Aleshin, A. N. et al., Mobility studies of field-effect transistor structures based on anthracene single crystals, *Appl. Phys. Lett.*, 84, 5383, 2004.
38. Podzorov, V. et al., Intrinsic charge transport on the surface of organic semiconductors, *Phys. Rev. Lett.*, 93, 086602, 2004.
39. Menard, E. et al., High-performance *n*- and *p*-type single-crystal organic transistors with free-space gate dielectrics, *Adv. Mater.*, 16, 2097, 2004.
40. Laudise, R. A. et al., Physical vapor growth of organic semiconductors, *J. Cryst. Growth*, 187, 449, 1998.
41. de Boer, R. W. I. et al., Space charge limited transport and time of flight measurements in tetracene single crystals: A comparative study, *J. Appl. Phys.*, 95, 1196, 2004.
42. Menard, E., Jiang, W., Podzorov, V., Garfunkel, E., Rogers, J. A., and Gershenson, M. E., unpublished.
43. Podzorov, V., Calhoun, M. F., and Gershenson, M. E., in **preparation**.
44. Niemax, J., Tripathi, A. K., and Pflaum, J., Comparison of the electronic properties of sublimation- and vapor-Bridgman-grown crystals of tetracene, *Appl. Phys. Lett.*, 86, 122105, 2005.
45. Moon, H. et al., Synthesis, crystal structure, and transistor performance of tetracene derivatives, *J. Am. Chem. Soc.*, 126, 15322, 2004.
46. Mas-Torrent, M. et al., High mobility of dithiophene-tetrathiafulvalene single-crystal organic field effect transistors, *J. Am. Chem. Soc.*, 126, 984, 2004.
47. Zeis, R., Siegrist, T., and Kloc, C., Single-crystal field-effect transistors based on copper phthalocyanine, *Appl. Phys. Lett.*, 86, 022103, 2005.
48. Zeis, R. et al., Field effect studies on rubrene and impurities of rubrene, *Chem. Mater.*, 18, 244 (2006).
49. Henn, D. E., Williams, W. G., and Gibbons, D. J., Crystallographic data for an orthorhombic form of rubrene, *J. Appl. Cryst.*, 4, 256, 1971.

AU: update?

50. Campbell, R. B., Monteath Robertson, J., and Trotter, J., The crystal structure of hexacene, and a revision of the crystallographic data for tetracene, *Acta Cryst.*, 15, 289, 1962.
51. Fritz, S. E. et al., Structural characterization of a pentacene monolayer on an amorphous SiO₂ substrate with grazing incidence x-ray diffraction, *J. Am. Chem. Soc.*, 126, 4084, 2004.
52. Ruiz, R. et al., Structure of pentacene thin films, *Appl. Phys. Lett.*, 85, 4926, 2004.
53. Menard, E., Marchenko, A., Podzorov, V., Gershenson, M. E., Fichou, D., and Rogers, J. A., to appear in *Adv. Mater.*, 2006.
54. For specifications, see the web site of Specialty Coating Systems: http://www.scscoatings.com/parylene_knowledge/specifications.cfm.
55. Podzorov, V., and Gershenson, M. E., Photoinduced charge transfer across the interface between organic molecular crystals and polymers, *Phys. Rev. Lett.*, 95, 016602, 2005.
56. Podzorov, V. et al., Interaction of organic surfaces with active species in the high-vacuum environment, *Appl. Phys. Lett.*, 87, 093505, 2005.
57. Stassen, A. F. et al., Influence of the gate dielectric on the mobility of rubrene single-crystal field-effect transistors, *Appl. Phys. Lett.*, 85, 3899, 2004.
58. Cahen, D., Kahn, A., and Umbach, E., Energetics of interfaces between molecules and conductors, *Mater. Today*, Jul./Aug., 32, 2005.
59. Chwang, A. B., and Frisbie, C. D., Field effect transport measurements on single grains of sexithiophene: Role of the contacts, *J. Phys. Chem. B*, 104, 12202, 2000.
60. Zaumseil, J., Baldwin, K. W., and Rogers, J. A., Contact resistance in organic transistors that use source and drain electrodes formed by soft contact lamination, *J. Appl. Phys.*, 93, 6117, 2003.
61. Hulea, I. N. et al., Reproducible low contact resistance in rubrene single-crystal field-effect transistors with nickel electrodes, *Appl. Phys. Lett.*, 88, 113512, 2006.
62. Troisi, A., and Orlandi, G., Charge-transport regime of crystalline organic semiconductors: Diffusion limited by thermal off-diagonal electronic disorder, *Phys. Rev. Lett.*, 96, 086601, 2006.
63. Sze, S. M., *Physics of semiconductor devices*, Wiley, New York, 1981.
64. Horowitz, G., Hajlaoui, M. E., and Hajlaoui, R., Temperature and gate voltage dependence of hole mobility in polycrystalline oligothiophene thin film transistors, *J. Appl. Phys.*, 87, 4456, 2000.
65. Shur, M., Hack, M., and Shaw, J. G., A new analytic model for amorphous silicon thin-film transistors, *J. Appl. Phys.*, 66, 3371, 1989.
66. Nakamura, K. et al., Light emission from organic single-crystal field-effect transistors, *J. Appl. Phys.*, 44, L1367, 2005.
67. Chua, L. L. et al., General observation of *n*-type field-effect behaviour in organic semiconductors, *Nature*, 434, 194, 2005.
68. Zaumseil, J., Friend, R., and Siringhaus, H., Spatial control of the recombination zone in an ambipolar light-emitting organic transistor, *Nat. Mater.*, 5, 69, 2006.
69. Chesterfield, R. J. et al., High electron mobility and ambipolar transport in organic thin-film transistors based on a π -stacking quinoidal terthiophene, *Adv. Mater.*, 15, 1278, 2003.
70. Misewich, J. A. et al., Electrically induced optical emission from a carbon nanotube FET, *Science*, 300, 783, 2003.
71. Podzorov, V. et al., High-mobility field-effect transistors based on transition metal dichalcogenides, *Appl. Phys. Lett.*, 84, 3301, 2004.

AU: update?

Charge Carrier Transport in Single-Crystal Organic Field-Effect Transistors 71

72. Yasuda, T., and Tsutsui, T., Organic field-effect transistors based on high electron and ambipolar carrier transport properties of copper-phthalocyanine, *Chem. Phys. Lett.*, 402, 395, 2005.
73. Meijer, E. J. et al., Solution-processed ambipolar organic field-effect transistors and inverters, *Nat. Mater.*, 2, 678, 2003.
74. de Boer, R. W. I. et al., Ambipolar Cu- and Fe-phthalocyanine single-crystal field-effect transistors, *Appl. Phys. Lett.*, 86, 262109, 2005.
75. Takahashi, T. et al., Ambipolar organic field-effect transistors based on rubrene single crystals, *Appl. Phys. Lett.*, 88, 033505, 2006.
76. Bao, Z., Lovinger, A. J., and Dodabalapur, A., Organic field-effect transistors with high mobility based on copper phthalocyanine, *Appl. Phys. Lett.*, 69, 3066, 1996.
77. Bube, R. H., *Photoconductivity in solids*, Wiley, New York, 1960.
78. Brédas, J. L. et al., Organic semiconductors: A theoretical characterization of the basic parameters governing charge transport, *Proc. Nat. Acad. Sci.*, 99, 5804, 2002.
79. Cheng, Y. C. et al., Three-dimensional band structure and bandlike mobility in oligoacene single crystals: A theoretical investigation, *J. Chem. Phys.*, 118, 3764, 2003.
80. de Wijs, G. A. et al., Anisotropy of the mobility of pentacene from frustration, *Synth. Met.*, 139, 109, 2003.
81. Mas-Torrent, M. et al., Correlation between crystal structure and mobility in organic field-effect transistors based on single crystals of tetrathiafulvalene derivatives, *J. Am. Chem. Soc.*, 126, 8546, 2004.
82. Podzorov, V. et al., Hall effect in the accumulation layers on the surface of organic semiconductors, *Phys. Rev. Lett.*, 95, 226601, 2005.
83. Takeya, J. et al., Hall effect of quasi-hole gas in organic single-crystal transistors, *J. Appl. Phys.*, 44, L1393, 2005.
84. Karl, N. et al., Fast electronic transport in organic molecular solids? *J. Vac. Sci. Technol. A*, 17, 2318, 1999.
85. Jurchescu, O. D., Baas, J., and Palstra, T. T. M., Effect of impurities on the mobility of single crystal pentacene, *Appl. Phys. Lett.*, 84, 3061, 2004.
86. Thorsmølle, V. K. et al., Ultrafast conductivity dynamics in pentacene probed using terahertz spectroscopy, *Appl. Phys. Lett.*, 84, 891, 2004.
87. Ostroverkhova, O. et al., Bandlike transport in pentacene and functionalized pentacene thin films revealed by subpicosecond transient photoconductivity measurements, *Phys. Rev. B*, 71, 035204, 2005.
88. Troisi, A., and Orlandi, G., Charge-transport regime of crystalline organic semiconductors: Diffusion limited by thermal off-diagonal electronic disorder, *Phys. Rev. Lett.*, 96, 086601, 2006.
89. Rang, Z. et al., Hydrostatic pressure dependence of charge carrier transport in single-crystal rubrene devices, *Appl. Phys. Lett.*, 86, 123501, 2005.
90. Veres, J. et al., Low-k insulators as the choice of dielectrics in organic field-effect transistors, *Adv. Funct. Mater.*, 13, 199, 2003.
91. Facchetti, A., Yoon, M.-H., and Marks, T. J., Gate dielectrics for organic field-effect transistors: New opportunities for organic electronics, *Adv. Mater.*, 17, 1705, 2005.
92. Hebard, A. F. et al., Conducting films of C₆₀ and C₇₀ by alkali-metal doping, *Nature*, 350, 600, 1991.
93. Kochanski, G. P. et al., Electrical resistivity and stoichiometry of K_xC₆₀ films, *Science*, 255, 184, 1992.

94. Panzer, M. J., and Frisbie, C. D., High charge carrier densities and conductance maxima in single-crystal organic field-effect transistors with a polymer electrolyte gate dielectric, *Appl. Phys. Lett.*, 88, 203504, 2006.
95. Wehrli, S., and Helm, C., Interface steps in field effect devices, *J. Appl. Phys.*, 95, 5621, 2004.
96. Narayan, K. S., and Kumar, N., Light responsive polymer field-effect transistor, *Appl. Phys. Lett.*, 79, 1891, 2001.
97. Hamilton, M. C., and Kanicki, J., Organic polymer thin-film transistor photosensors, *IEEE J. Selected Topics Quantum Electronics*, 10, 840, 2004; Noh, Y.-Y. et al., High-photosensitivity *p*-channel organic phototransistors based on a biphenyl end-capped fused bithiophene oligomer, *Appl. Phys. Lett.*, 86, 043501, 2005; Saragi, T. P. I. et al., Organic phototransistor based on intramolecular charge transfer in a bifunctional spiro compound, *Appl. Phys. Lett.*, 84, 2334, 2004.
98. Podzorov, V., and Pudalov, V. M., Gershenson, M. E., Light-induced switching in back-gated organic transistors with built-in conduction channel, *Appl. Phys. Lett.*, 85, 6039, 2004.
99. Najafov, H. et al., Primary photoexcitations and the origin of the photocurrent in rubrene single crystals, *Phys. Rev. Lett.*, 96, 056604, 2006.
100. Schmechel, R., and von Seggern, H., Electronic traps in organic transport layers, *Phys. Stat. Sol.*, 201, 1215, 2004.
101. Lang, D. V. et al., Amorphouslike density of gap states in single-crystal pentacene, *Phys. Rev. Lett.*, 93, 086802, 2004.
102. Crone, B. et al., Electronic sensing of vapors with organic transistors, *Appl. Phys. Lett.*, 78, 2229, 2001.
103. Zhu, Z.-T., Mason, J. T., Dieckmann, R., and Malliaras, G. G., Humidity sensors based on pentacene thin-film transistors, *Appl. Phys. Lett.*, 81, 4643, 2002.
104. Jurchescu, O. D., Baas, J., and Palstra, T. T. M., Electronic transport properties of pentacene single crystals upon exposure to air, *Appl. Phys. Lett.*, 87, 052102, 2005.
105. Nardello, V. et al., Photochemistry without light: Oxidation of rubrene in a micro-emulsion with a chemical source of singlet molecular oxygen ($^1\text{O}_2$, $^1\text{D}_g$), *J. Chemical Education*, 76, 1285, 1999.
106. Käffer, D., and Witte, G., Growth of crystalline rubrene films with enhanced stability, *Phys. Chem. Chem. Phys.*, 7, 2850, 2005.
107. Takeya, J. et al., Effects of polarized organosilane self-assembled monolayers on organic single-crystal field-effect transistors, *Appl. Phys. Lett.*, 85, 5078, 2004.
108. Bürgi, L. et al., Close look at charge carrier injection in polymer field-effect transistors, *J. Appl. Phys.*, 94, 6129, 2003.
109. Payne, M. M. et al., Organic field-effect transistors from solution-deposited function-alized acenes with mobilities as high as $1 \text{ cm}^2/\text{V}\cdot\text{s}$, *J. Am. Chem. Soc.*, 127, 4986, 2005.
110. Klare, J. et al., Cruciform systems for molecular electronics applications, *J. Am. Chem. Soc.*, 125, 6030, 2003.
111. Stingelin-Stutzmann, N. et al., Organic thin-film electronics from vitreous solution-processed rubrene hypererectectics, *Nat. Mater.*, 4, 601, 2005.



2.2 Charge Transport in Oligomers

Gilles Horowitz

CONTENTS

2.2.1	Introduction	73
2.2.2	Operating Mode of the Organic Thin-Film Transistor	75
2.2.3	Charge Transport in Conjugated Oligomers	77
2.2.3.1	Band Transport	78
2.2.3.2	Polaron Transport	80
2.2.3.2.1	Polarization in Molecular Crystals.....	80
2.2.3.2.2	Molecular Polaron	82
2.2.3.2.3	Marcus Model.....	83
2.2.3.3	Hopping Transport.....	85
2.2.4	Trap Limited Transport in Organic Transistors.....	86
2.2.5	Parameter Extraction.....	89
2.2.5.1	Threshold Voltage.....	91
2.2.5.2	Contact Resistance	91
2.2.5.2.1	Contact Resistance Extraction.....	91
2.2.5.2.2	Origin of Contact Resistance	94
2.2.5.3	Mobility Degradation	95
2.2.6	Concluding Remarks.....	97
	Acknowledgments.....	97
	References.....	99

2.2.1 INTRODUCTION

Solids are made of atoms, which in turn are composed of an ion core (i.e., the nucleus and those electrons so strongly bound to it that they cannot move around) and valence electrons (electrons in the outermost shell). Solid-state physics textbooks [1] teach us that the most important physical distinction in solids, as established on the basis of the configuration of valence electrons, is that between metals and insulators. The difference depends on whether there is (metals) or is not (insulators) any partially filled energy band. In perfect crystals at zero temperature, this is a rigorous criterion leading to unambiguous categories. The concept of (intrinsic) semiconductor only emerges at nonzero temperature in insulators with small energy



gap, where thermal excitation of electrons from the valence band to the conduction band may occur. Because their electrical properties so strongly depend on temperature, intrinsic semiconductors are of no practical use for realizing microelectronic devices, which instead are based on the concept of *extrinsic* semiconductors, in which charge carriers are induced by intentionally added impurities.

Based on the configuration of the valence electrons, it is of common practice to make a distinction among four classes of solids [1]:

1. The outstanding example of *molecular crystals* is the solid noble gases. They have completely filled electronic shells, so there is little electronic density between ion cores; all the electrons remain in the vicinity of their parent ions. For this reason, molecular crystals are insulators.
2. Like in molecular crystals, the electronic charge distributions in *ionic crystals* are highly localized in the neighborhood of the ion cores. However, some electrons are now bound to the component of the opposite type. As such, ionic crystals can be viewed as molecular crystals in which the constituents are not atoms or molecules, but ions. Ionic crystals are also insulators.
3. In *metals*, unlike the two previous cases, the density of electrons remains appreciable even in between the ion cores, leading to the fact that metals are electronic conductors.
4. The situation in *covalent crystals* is something in between that of insulators and metals. In covalent crystals, valence electrons are not sharply localized near the ion cores. However, the density of electrons is not uniform; instead, it concentrates along certain preferred directions, leading to chemical bonds. It is interesting to note that conventional semiconductors (and especially silicon) are covalent crystals.

The electronic charge distribution in the four categories of solids are schematically displayed in Figure 2.2.1.

Organic molecular crystals, that is, crystals made of organic molecules [2], obviously belong to the class of molecular crystals. It may therefore sound paradoxical to call some of these crystals — namely, those made of *conjugated* molecules — *organic semiconductors* [3,4]. The expression actually emerged when it was found that the electrical resistance of crystals of various phthalocyanines, measured between two metal electrodes, presented the thermally activated behavior characteristic of intrinsic semiconductors [5,6], an observation that was extended later to other conjugated organic solids [7–10]. Although the interpretation of the thermally activated resistivity was probably flawed because the presence of impurities and crystal defects was not taken into account, these findings opened the way to further investigations on the subject. The practical reason for such a development was the prospect of joining organic chemistry with electronics. The phenomena of photoconductivity, electroluminescence, superconductivity, and the photovoltaic effect have all been identified in organic crystals [26]. However, the launch of *organic electronics* had to wait until it was demonstrated that real devices, such as light-emitting diodes [12] and field-effect transistors [13], could be indeed fabricated with organic semiconductors.



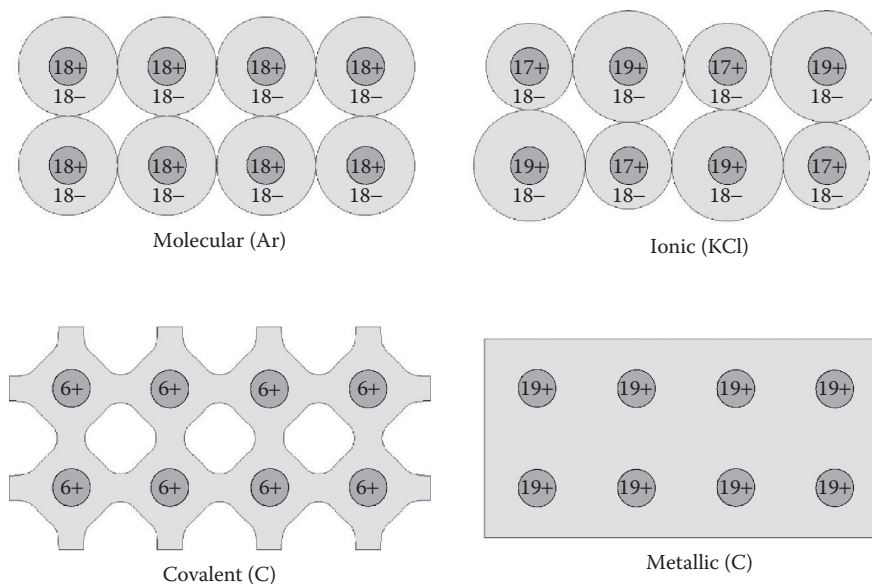


FIGURE 2.2.1 Schematic two-dimensional view of the electronic space distribution in the four basic solid categories. The small circles represent the nuclei and the shaded areas the regions where electron density is significant. (a) Molecular (argon); (b) ionic (potassium chloride); covalent (carbon-diamond); (c) metallic (potassium).

Because conjugated organic solids are more like insulators than semiconductors, charge transport in these materials is much less efficient than in conventional semiconductors. The problem is more crucial in transistors, where charges have to travel along much longer ways than in diodes. At the current state of the art, mobility in organic thin-film transistor (OTFT) ranges between 0.01 and 10 cm^2/Vs , which is still much lower than what found in inorganic semiconductors (mobility is around 1,000 cm^2/Vs in silicon), but substantially higher than the typical numbers for organic light-emitting diodes or photovoltaic cells. “High” mobility in OTFT is the result of large research efforts at improving structural order in the organic semiconductor film. It is worth pointing out that the highest mobility is achieved with organic single crystals. However, the physical origin of high mobility in organic solids is still an unresolved theoretical question. It is the aim of this chapter to account for the theoretical efforts that have been made to understand charge carrier transport in organic oligomers and small molecules.

2.2.2 OPERATING MODE OF THE ORGANIC THIN-FILM TRANSISTOR

The basic idea that guides the insulated-gate field-effect transistor (FET) traces back to the mid-1920s [14], but it was not until 1960 that this early concept could be successfully demonstrated, with the invention of the metal-oxide-semiconductor FET (MOSFET) [15]. Field-effect measurements on copper phthalocyanine films were

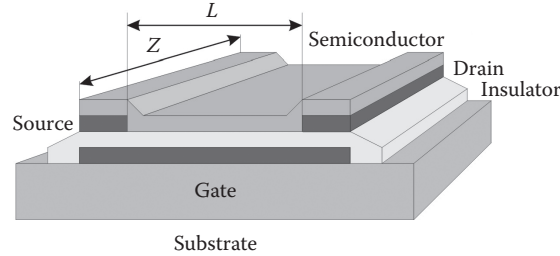


FIGURE 2.2.2 Three-dimensional view of an organic thin-film transistor.

reported as early as 1964 [16]. However, organic transistors that could indeed be used in practical electronic circuits only appeared in the late 1980s [13,17].

Figure 2.2.2 shows a three-dimensional view of an organic thin-film transistor. The active part of the device is constituted of an organic semiconductor thin film equipped with two electrodes: the source and the drain. The distance between the source and the drain is called the channel length L ; the transverse dimension of the structure is the channel width Z . A third electrode, the gate, is laid out along the channel between source and drain; this electrode is electrically isolated from the semiconductor film by a thin insulating film, hence forming a metal-insulator-semiconductor (MIS) structure. By applying a voltage V_G between source and gate, one induces the formation of an accumulation layer at the semiconductor-insulator interface, thus forming a conducting channel between these two electrodes.

A unique feature of FETs is that, unlike diodes, these devices are two dimensional. That is, they are governed by two independent voltages perpendicular to each other. The role of the gate voltage V_G is to induce charges in the conducting channel, while the drain voltage V_D drives these charges from source to drain. The most popular equations to describe the current-voltage curves of an FET are very simple, but this simplicity hides several assumptions that are not usually fulfilled in organic devices. In short, I-V characteristics can be drawn by either varying the drain voltage at a constant gate voltage (output characteristics) or changing the gate voltage at a fixed drain voltage (transfer characteristics). In the former case, the curves are divided into a linear regime at low V_D that convert into the saturation regime when $V_D > V_G$. The current in both regimes is given by Equations(1) and (2). [18]

$$I_{Dlin} = \frac{Z}{L} C_i \mu \left[(V_G - V_T) V_D - \frac{V_D^2}{2} \right], \quad (2.2.1)$$

$$I_{Dsat} = \frac{Z}{2L} C_i \mu (V_G - V_T)^2. \quad (2.2.2)$$

Here, C_i is the capacitance of the insulator, μ the mobility in the semiconductor, and V_T the threshold voltage. The meaning of the latter parameter will be detailed later. In short, V_T is the gate voltage beyond which the conducting channel forms.

Apart from showing the performance of the device, I–V curves are used to extract its basic parameter, primarily the mobility and threshold voltage. A widely used method for parameter extraction consists of plotting the square root of the saturation current as a function of the gate voltage. As seen in Equation (2.2.2), this is supposed to give a straight line, the slope of which gives μ while its extrapolation to the V_G axis corresponds to the threshold voltage.

Equations (2.2.1) and (2.2.2) rests on the following assumptions: (1) The transverse electric field induced by the gate voltage is largely higher than the longitudinal field induced by the gate bias (so-called gradual channel approximation); (2) the mobility is constant all over the channel. Assumption (1) is justified by the geometry of the device; that is, the distance from source to drain is most often much larger than the thickness of the insulator. Assumption (2) is more or less fulfilled in a conventional inorganic semiconductor. However, this is far from true in organic solids, as will be shown in this chapter. For this reason, the use of Equation (2.2.2) to extract the mobility may lead to an incomplete, if not erroneous, description of charge transport in organic semiconductors. Alternative approaches to circumvent this difficulty will be presented in the following sections.

2.2.3 CHARGE TRANSPORT IN CONJUGATED OLIGOMERS

In contrast to its parent elements of column IV of the periodic table (Si, Ge ...), carbon presents the unique feature of being able to exist under three different hybridization configurations: namely, sp , sp^2 , and sp^3 . The latter one is found in the so-called saturated compounds that are the constituting element of plastics. In this configuration, each carbon atom is linked to its neighbors by four strong σ bonds that point to the four verges of a tetrahedron. Because σ bonds are so strong, the distance between the bonding and antibonding energy levels (also called highest occupied and lowest unoccupied molecular orbitals — HOMO and LUMO) is high, which has two consequences: Plastics are transparent to visible light, and they are electrically insulating.

All the organic compounds designated as semiconductors are those made of sp^2 hybridized carbons, also called *conjugated* organic materials. Under such circumstances, each carbon is linked to its neighbors by three σ bonds resulting from the hybridization of $2s$, $2p_x$, and $2p_y$ orbitals, while the remaining $2p_z$ orbital forms a π bond, which presents significantly less overlap than σ bonds. For this reason, the energy distance between the bonding and antibonding orbitals is somewhat reduced, which has two consequences: The materials absorb visible light (dyes are conjugated materials) and may behave as a semiconductor at nonzero temperature. This concept is illustrated in Figure 2.2.3 in the case of ethylene C_2H_2 .

In larger molecules, typically benzene, the π orbitals become delocalized and form a π system that extends all over the molecule. The HOMO–LUMO gap becomes smaller with increasing delocalization.

In the case of a long chain of carbon atoms, the π bonds delocalize over the whole chain and form a one-dimensional electronic system. The resulting one-

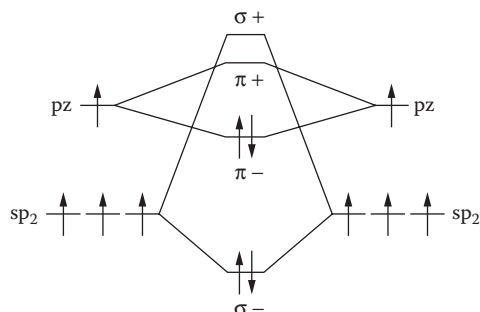


FIGURE 2.2.3 Energy scheme of ethylene C_2H_2 .

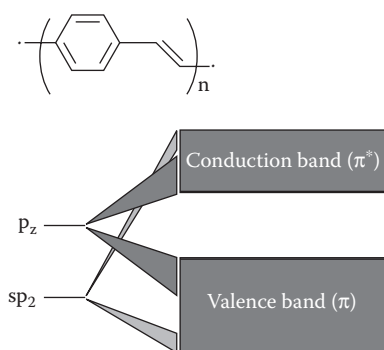


FIGURE 2.2.4 Molecular and energy schemes of poly-para-phenylene-vinylene (PPV).

dimensional band has substantial band width, and the chain can be viewed as a one-dimensional semiconductor with a filled valence band originating from the HOMO and an empty conduction band coming from the LUMO. Figure 2.2.4 illustrates this image with the molecule of poly-para-phenylene-vinylene (PPV).

The image depicted in Figure 2.2.4 gives rationale for why charge carriers can be injected and reside in a conjugated molecule. However, the limiting step for charge transport in a solid is not within single molecules; rather, it involves electron transfer between molecules or molecular chains; because orbital overlap between molecules is low, the phenomenon of charge transport in conjugated solids requires further investigations.

2.2.3.1 BAND TRANSPORT

Band transport refers to the mechanism occurring in crystalline inorganic solids like metals and semiconductors. Band theory can be found in numerous textbooks [1] and will not be detailed here. In short, energy bands in solids form because when a very large number of interacting atoms are brought together, their energy levels become so closely spaced that they become indistinct. Any solid has a large number of energy bands, but not all these bands are filled with electrons. The likelihood of any particular band to be filled is given by the Fermi–Dirac statistics, Equation

(2.2.3), so that at zero temperature, bands are filled up to the so-called Fermi energy E_F .

$$f(E) = \frac{1}{1 + \exp \frac{E - E_F}{kT}}. \quad (2.2.3)$$

On this basis, solids can be divided into insulators, in which the highest occupied band (the valence band) is completely filled, while the lowest unoccupied band (the conduction band) is completely empty and metals present a partly empty and partly filled band (the conduction band). Semiconductors are a particular case of insulators where the energy gap between the top of the valence band and the bottom of the conduction band is small enough that, at nonzero temperature, the smoothing out of the Fermi–Dirac distribution causes an appreciable number of states at top of the valence band to be empty and an equivalent number of states at bottom of the conduction band to be filled. Note that the conductivity in semiconductors is highly temperature dependent.

The simplest model of charge transport in delocalized bands is the Drude model, which assumes the carriers are free to move under the influence of an applied electric field, but subject to collisional damping forces. Note that the scattering centers are not the nuclei of the background material, but rather phonons (lattice vibrations) or impurities. A statistical equation for estimating the mean drift velocity of the carriers in the direction of the electric field F_x may be written as

$$\frac{d}{dt} \langle v_x \rangle = \frac{q}{m^*} F_x - \frac{1}{\tau} \langle v_x \rangle, \quad (2.2.4)$$

where q is the elemental charge and m^* the effective mass. τ is the mean free time between two collisions (or relaxation time). Steady state corresponds to $\frac{d}{dt} \langle v_x \rangle = 0$. Under such circumstances, the solution of Equation (2.2.4) writes

$$\langle v_x \rangle = \frac{q\tau}{m^*} F_x = \mu F_x, \quad (2.2.5)$$

which defines the mobility μ . It is important to note at this stage that the model is only valid when the mean free path λ — that is, the mean distance between two collisions — is much larger than a characteristic distance that can be the de Broglie length of the charge carrier, or the distance between two atoms in the crystal. The mean free path is given by

$$\lambda = v_{th} \tau, \quad (2.2.6)$$

where $v_{th} = \sqrt{3kT / m^*}$ is the electron thermal velocity ($\sim 10^5$ m/s at room temperature). From (5) and (6) the mobility can also be defined as

$$\mu = \frac{q\lambda}{m^* v_{th}}. \quad (2.2.7)$$

The temperature dependence of the mobility depends on the nature of the scattering centers (acoustical or optical phonons, charged impurities ...) However, in all cases, it is found that the dependence follows the general law given by Equation (2.2.8).

$$\mu(T) \propto T^{-n}. \quad (2.2.8)$$

In most practical cases, n is positive, so the mobility increases when temperature decreases.

Evidence for “band transport” is often claimed to be brought when the temperature dependence in Equation (2.2.8) is observed. The most celebrated example for such a behavior is that by Karl and coworkers on highly pure crystals of acenes [19]. However, as pointed out by Silinsh and Capek [20], the argument does not resist further analysis because, at least for temperatures above 100 K, the mean free path calculated from Equation (2.2.5) falls below the distance between molecules in the crystal, which is not physically consistent with diffusion limited transport, so the exact nature of charge transport in these crystals is still unresolved for the time being.

2.2.3.2 POLARON TRANSPORT

2.2.3.2.1 Polarization in Molecular Crystals

The main reason why the band model is unable to account for charge transport in organic semiconductors is that it fails to account for a crucial phenomenon in these materials: polarization. The occurrence of polarization in organic solids has been analyzed in detail by Silinsh and Capek [20]. The principle is the following. A charge carrier residing on a molecular site tends to polarize its neighboring region. As the resulting formed polarization cloud moves with the charge, the traveling entity is no longer a naked charge, but a “dressed” charge, and the formed species is called a *polaron*. In conjugated solids, the main polarization effect is that on the clouds formed by the π -electrons. The principle is illustrated in Figure 2.2.5, where the conjugated molecules are symbolized by benzene rings; the hexagons represent the (fixed) core of the six carbon atoms, while the circles stand for the delocalized π -electrons. Under the effect of the positive charge on the central molecule, the π -electron rings tend to move towards the central molecule, thus creating an electric dipole, the magnitude of which is the greater as the molecule is closer to the center.

In order to estimate the stability of the polaron, we can define two typical times: (1) the residence time τ_{res} corresponds to the average time a charge will reside on a molecule; (2) the electronic polarization time τ_{el} is the time it takes for the polarization cloud to form around the charge. An order of magnitude for both times can be estimated by using Heisenberg’s uncertainty principle

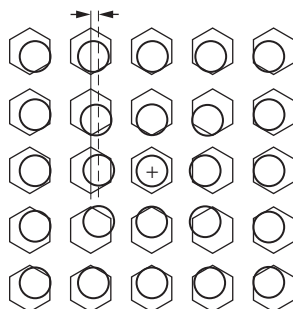


FIGURE 2.2.5 The figure is a schematic representation of the formation of a polaron when a positive charge is placed on a molecule in a conjugated organic solid. The hexagons symbolize the core of the nuclei, while the circles represent the delocalized π -electrons.

$$\tau \frac{\hbar}{\Delta E}, \quad (2.2.9)$$

where ΔE is a characteristic energy.

For the residence time, the pertinent energy is the width W of the allowed band, typically 0.1 eV in an organic semiconductor and 10 eV in an inorganic semiconductor, which gives a residence time of 10^{-14} s for the former and 10^{-16} s for the latter. As for the electronic polarization time, the corresponding energy is that of an electron transition — that is, the energy gap (~ 1 eV) — so the time of the order of 10^{-15} s in both cases.

Similarly to electronic polarization, other polarization mechanisms can be invoked: molecular polarization, which concerns the displacement of the nuclei of the molecule where the charge resides, and lattice polarization, which involves movements of the entire lattice. The energies and times corresponding to these processes are estimated from the intramolecular and lattice vibration frequencies. The energy and time of the various polarization processes are summarized in Table 2.2.1.

Table 2.2.1 reveals a striking difference between inorganic and organic semiconductors. In the former, the localization time is shorter than all the possible polarization times. In other words, electrons and holes move so fast that the polarization cloud does not have enough time to form. This is actually included in the band theory through the so-called rigid-band approximation, which states that the band structure remains unchanged when a charge is injected in the solid.

The situation is drastically different in organic materials. Here, the electronic polaron has long enough time to form, so the energy levels of a charged molecule are significantly shifted with respect to that of a neutral molecule, as shown in Figure 2.2.6. As for the molecular polarization, it forms in a time comparable to the residence time, so the situation varies from one compound to the other. Finally, the formation time of the lattice polaron is too long, so its occurrence is unlikely under all circumstances.

The pertinent parameters in the energy diagram in Figure 2.2.6 are the polarization energies for positive P^+ and negative charge carriers P^- . Both are composed

TABLE 2.2.1
Residence Time and Various Polarization Times

		Energy (eV)	Time (s)
Residence τ_{res}	Inorganic SC	10	10^{-16}
	Molecular SC	0.1	10^{-14}
Polarization	Electronic τ_{el}	1	10^{-15}
	Molecular τ_v	0.1	10^{-14}
	Lattice τ_l	< 0.01	> 10^{-13}

Note: The reference energy is bandwidth for residence time, energy gap for electronic polarization, molecular vibration ($\sim 1,000 \text{ cm}^{-1}$) for molecular polarization, and lattice vibration ($< 100 \text{ cm}^{-1}$) for lattice polarization.

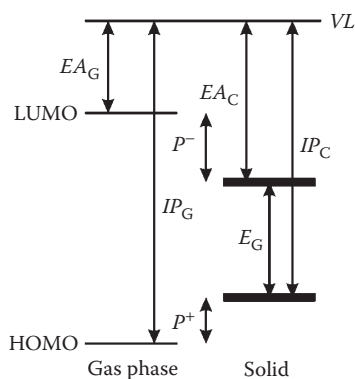


FIGURE 2.2.6 Energy scheme of the electronic polaron in a molecular crystal. VL is the vacuum level, EA the electronic affinity, and IP the ionization potential. P^+ and P^- are the polarization energy for positive and negative charge, respectively, and E_G the transport band gap. (From Silinsh, E.A. and Capek, V., *Organic molecular crystals: Interaction, localization, and transport phenomena*, AIP Press, New York, 1994.)

of various contributions that render their estimation complex. A detailed analysis of the process of electronic polarization in crystals of polyacenes can be found in Reference 21, together with theoretical and experimental determinations of the corresponding energies. Representative data are sketched in Table 2.2.2.

2.2.3.2.2 Molecular Polaron

Complementary to the electronic polarization, a charge carrier created in a molecular solid also polarizes the intramolecular vibration modes of the molecule on which it is located as well as dipole active modes of the neighboring molecules, thus forming an extended ionic state. As already mentioned, the corresponding relaxation time τ_v is comparable to the residence time τ_{res} . The new quasiparticle associated with this

TABLE 2.2.2
Calculated and Measured Polarization Energy
in Polyacenes

Crystal	P^+ (eV)		P^- (eV)	
	Experimental	Calculated	Experimental	Calculated
Anthracene	1.65	1.52	1.09	1.16
Tetracene	1.72	1.52	1.10	1.07
Pentacene	1.63	1.48	1.17	1.02

Source: Silinsh, E.A. and Capek, V., *Organic molecular crystals: Interaction, localization, and transport phenomena*, AIP Press, New York, 1994.

process is termed molecular polaron. The relaxation energy E_b gained in the process corresponds to the difference between the optical (direct) and adiabatic energy gaps.

An important feature in the rationalization of the temperature-dependent mobility of highly pure polyacenes is the temperature dependence of the effective mass expressed by

$$m_{eff}(T) = m_{eff}(0)e^{T/T_0}, \quad (2.2.10)$$

where $m_{eff}(0)$ is the molecular polaron effective mass at $T = 0$ and T_0 a characteristic temperature [20].

The great interest of the molecular polaron model is that it can account for the apparent contradiction between the band-like temperature-dependent mobility and a small mean-free path. The weak point of the approach developed by Silinsh and coworkers is that it is phenomenological. It is worth mentioning that a more consistent analytical theory has been formulated by Kenkre and coworkers [22]. The presentation of this model would go to far outside the scope of this chapter and will not be developed here.

2.2.3.2.3 Marcus Model

An alternative approach to describe charge transport in polarizable media uses Marcus's electron transfer (ET) theory. Originally, the theory aimed at describing electron transfer from an electron donor to an electron acceptor in solution, according to



It is of usual practice to represent the energy involved in the reaction in a diagram where the energy of the reactants V_R (left-hand side in the equation) and the products V_P (right-hand side of the equation) are given along a generalized coordinate q by a parabola:

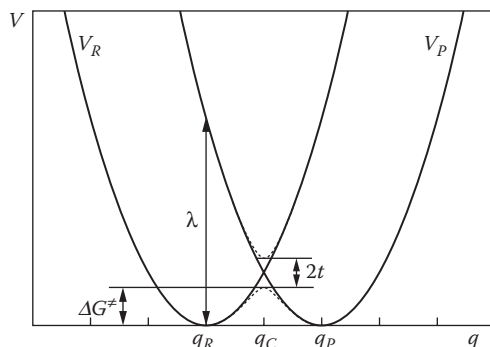


FIGURE 2.2.7 Potential energy of the charge transfer reaction in the dimer coordinate representation. λ is the reorganization energy, t the transfer integral, and ΔG^\ddagger the energy barrier height.

$$V_R = \frac{q}{2}(q - q_R)^2, \quad V_P = \frac{q}{2}(q - q_P)^2. \quad (2.2.12)$$

Here, the subscripts R refer to the reactant and P to the product.

In the case where the electron transfer is faster than molecular reorganization (nonadiabatic transfer), the path for electron transfer in the dimer coordinate representation illustrated in Figure 2.2.7 can be decomposed in a vertical activation from the minimum of V_R to the V_P curve, followed by a relaxation to the equilibrium configuration of the product. Accordingly, the Marcus theory of electron transfer [23] introduces the reorganization energy λ

$$\lambda = \frac{f}{2}(q_R - q_P)^2. \quad (2.2.13)$$

and f is an oscillator strength.

If we now introduce the transfer integral t (dotted line in Figure 2.2.7), the energy barrier height for reaction Equation (2.2.11) is given by

$$\Delta G^\ddagger = \frac{(\lambda - 2t)^2}{4\lambda} \approx \frac{\lambda}{4} - t, \quad t < \lambda, \quad (2.2.14)$$

The transfer integral t critically depends on the structural organisation (i.e., crystal structure) of the organic solid. Several computational techniques have been developed to estimate the transfer integral; a recent review can be found in Newton [24].

Assuming a classical Arrhenius behavior, the electron transfer rate k_{ET} is given by

$$k_{ET} = A \exp \left[-\frac{\lambda/4 - t}{kT} \right], \quad (2.2.15)$$

TABLE 2.2.3
Calculated Reorganisation Energy and Transfer Integral in Polyacenes

	Naphthalene	Anthracene	Tetracene	Pentacene
Reorganisation energy (meV)	187	137	113	97
Transfer integral (meV)	37	48	69	98
(meV)	74	96	138	196

Source: Taken from Bredas, J.-L. et al., *Chem. Rev.*, 104, 4971, 2004.

where A is a constant that depends on the frequency at which the electron gets across the energy barrier.

Equation (2.2.15) poses an obvious problem; that is, it predicts that the electron transfer approaches zero as the temperature approaches zero, which is at variance with experiment. The reason for such a discrepancy is that the classical theory does not account for tunneling effects that occur at low temperature. A semiclassical treatment can overcome this problem; it leads to an equation of the form [25]:

$$k_{ET} = \frac{2\pi}{\hbar} \frac{t^2}{\sqrt{4\pi\lambda kT}} \exp\left[-\frac{\lambda/4 - t}{kT}\right]. \quad (2.2.16)$$

A connection can be established between the Marcus theory and the polaron model by noting that the mobility is connected to the electron transfer rate by [26]

$$\mu = \frac{qa^2}{kT} k_{ET}. \quad (2.2.17)$$

where a is the lattice parameter of the molecular crystal.

A generalization of the Marcus theory establishes an important criterion for activationless (“band-like”) or localized transport; namely, the former occurs when $2t > \lambda$, while the latter dominates when $2t < \lambda$. A connection with the molecular polaron model developed before can be derived from the fact that the reorganization energy is linked to the molecular polarization time, and the transfer integral to the residence time, so the first inequality can also write $\tau_{res} < \tau_v$ and the second one $\tau_{res} > \tau_v$, which is precisely what was established previously.

Table 2.2.3 gives values of calculated reorganization energy and transfer integral for the polyacene series [27]. It can be seen that localized transport is expected for naphthalene and anthracene and delocalized transport for pentacene; tetracene is located in between these two extreme cases.

2.2.3.3 HOPPING TRANSPORT

The problem with hopping transport is that dozens of different models have been proposed, based on different physical principles and approximations. Moreover, most

of these models only give a qualitative description of charge transport, thus preventing the possibility of computational treatment.

However, hopping models have proved useful in rationalizing charge transport in disordered materials, such as polymers. Time of flight (TOF) measurements have revealed that the carrier mobility in these organic materials is thermally activated. Another ubiquitous feature relates to the field dependence of μ obeying $\ln \mu \propto \sqrt{F}$ law, where F is the magnitude of the electric field. The current practice is to interpret this behavior in terms of Gill's [28] or Poole–Frenkel-like equation

$$\mu = \mu_0 e^{-\left(\Delta_0 - \beta\sqrt{F}\right)/kT_{eff}}, \quad (2.2.18)$$

where $1/T_{eff} = 1/T - 1/T^*$ and β is the Poole–Frenkel (PF) factor. The problem with Equation (2.2.18) is that it presents several physical inconsistencies, among which are the lack of physical meaning for the effective temperature and the fact that the actual values of the PF factor are far from that predicted by the conventional Poole–Frenkel theory.

The disorder model developed by Bässler [29] rests on the following assumptions: (1) Because of the randomness of the intermolecular interactions, the electronic polarization energy of a charge carrier located on a molecule is subject to fluctuations; (2) transport is described in terms of hopping among localized states. In analogy to optical absorption profiles, the DOS is described by a Gaussian distribution of variance σ ; (3) charge transport is random walk described by a generalized master equation of the Miller–Abrahams form [30]:

$$v = v_0 e^{-2\gamma\Delta R_{ij}} e^{-\Delta\varepsilon_{ij}/kT}, \quad (2.2.19)$$

where ΔR_{ij} is the intersite distance and $\Delta\varepsilon_{ij}$ the energy difference of the sites; (4) In addition to the energetic disorder, there exists a position disorder with a Gaussian distribution of variance Σ (the so-called *off diagonal* disorder).

From a Monte Carlo simulation, Bässler arrives at a universal law relating the mobility to the degree of both diagonal and off diagonal disorder:

$$\mu = \mu_0 \exp\left[-\left(\frac{2}{3} \frac{\sigma}{kT}\right)^2\right] \exp\left\{C \left[\left(\frac{\sigma}{kT}\right)^2 - \Sigma^2\right] \sqrt{F}\right\}, \quad (2.2.20)$$

where C is an empirical constant.

2.2.4 TRAP LIMITED TRANSPORT IN ORGANIC TRANSISTORS

In real organic transistors, charge transport is most of the time limited by localized states induced by defects and unwanted impurities. Clear evidence for such a process

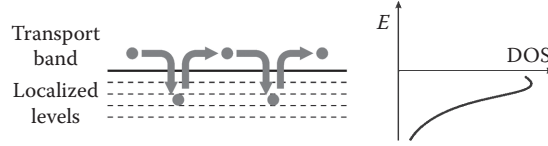


FIGURE 2.2.8 Principle of charge transport limited by multiple trapping and thermal release.

is given by the fact that the performance of the devices is strongly sample dependent. Two useful models for accounting for such a trend are the multiple trapping and thermal release (MTR) and variable range hopping (VRH) models. While hopping transport is appropriate to describe charge transport in disordered materials, the MTR model [31] applies to well-ordered materials, prototypes of which are vapor deposited small molecules like pentacene or the oligothiophenes, where thermally activated mobility is often observed. The basic assumption of the model is a distribution of localized energy levels located in the vicinity of the transport band edge. During their transit in the delocalized band, the charge carriers interact with the localized levels through trapping and thermal release (Figure 2.2.8).

The model rests on the following assumptions: (1) Carriers arriving at a trap are instantaneously captured with a probability close to one; and (2) the release of trapped carriers is controlled by a thermally activated process. The resulting effective mobility μ_{eff} is related to the mobility μ_0 in the transport band by an equation of the form

$$\mu_{eff} = \mu_0 \alpha e^{-(E_c - E_t)/kT}. \quad (2.2.21)$$

where E_c is the energy of the transport band edge. In the case of a single trap level of energy E_t and density of state (DOS) N_t , the total charge-carrier concentration n_{tot} splits into a concentration of free carriers $n_f = N_c e^{-(E_c - E_F)/kT}$, where N_c is the effective density of states at transport band edge, and a concentration of trapped carriers $n_t = N_t e^{-(E_t - E_F)/kT}$. The ratio of trapped to total densities is given by [32]

$$\Theta = \frac{n_t}{n_t + n_f} = \frac{1}{1 + \frac{N_t}{N_c} e^{(E_c - E_t)/kT}} \approx \frac{N_t}{N_c} e^{-(E_c - E_t)/kT}. \quad (2.2.22)$$

In that instance, the effective mobility is $\mu_{eff} = \Theta \mu_0$, so that E_t in Equation (2.2.21) is the energy of the single trap level and α the ratio of the trap DOS to the effective density of states at transport band edge. If traps are energy distributed, distribution-dependent effective values of E_t and α must be estimated, as will be exemplified in the following. In all circumstances, whichever the actual energy distribution of traps, the main feature predicted by the MTR model is thermally activated mobility.

An important outcome of the MTR model is that in the case of an energy distributed DOS, mobility is gate voltage dependent. The mechanism at work is schematically pictured in Figure 2.2.9.

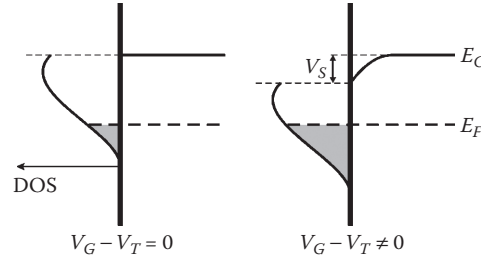


FIGURE 2.2.9 Gate voltage dependent mobility induced by an energy distributed density of traps.

When a bias is applied to the gate, a potential V_s develops at the insulator–semiconductor interface, which results in shifting by the same amount of the Fermi level towards the transport band edge, thus partly filling the distribution of localized states. Accordingly, the energy distance between the filled traps and the transport band edge is reduced, so trapped-carrier release is made easier, and the effective mobility increases. Such a gate-voltage dependence of mobility has indeed been reported on several occasions [32,33].

The shape of the gate voltage dependence depends on that of the DOS. We have seen before that in hopping models, the preferred DOS distribution is a Gaussian distribution. By analogy with what is found in hydrogenated amorphous silicon [31], the trap distribution used in the MTR model is an exponential band tail. This is because the trap distribution no longer corresponds to the transport band itself (as in the case of the hopping model); instead, the DOS is a tail to a delocalized transport band. Note, however, that an exponential tail distribution can also be associated to a Gaussian transport DOS. One of the major interests of the exponential distribution is that it leads to an analytical form of the gate voltage dependence of the mobility. The general form of an exponential distribution of traps is given by

$$N_t(E) = \frac{N_{t0}}{kT_0} e^{-(E_c - E)/kT_0}, \quad (2.2.23)$$

where N_{t0} is the total density (per unit area) of traps and T_0 a characteristic temperature that accounts for the slope of the distribution. The previously defined trapped charge is connected to the density of traps through

$$n_t = q \int_{-\infty}^{+\infty} N_t(E) f(E) dE, \quad (2.2.24)$$

where $f(E)$ is the Fermi distribution. If $N_t(E)$ is a slowly varying function, the Fermi distribution can be approximated to a step function; that is, it equals zero for $E < E_F$ and one for $E > E_F$. The integration of Equation (2.2.24) leads to

$$n_t \approx qN_t(E_{F0} + qV_s) = n_{t0}e^{qV_s/kT_0}. \quad (2.2.25)$$

As stated earlier, we have made use of the fact that the Fermi level E_F is shifted towards the band edge E_c from the value E_{F0} at zero gate bias by an amount qV_s (see Figure 2.2.9). $n_{t0} = N_{t0}e^{-(E_c - E_{F0})/kT_0}$ is the density of trapped charge at zero gate voltage. Making use of the defined effective mobility and assuming $n_f \ll n_t$, we finally obtain [34]

$$\mu_{eff} = \mu_0 \frac{N_c}{N_{t0}} \left(\frac{C_i(V_G - V_T)}{qN_{t0}} \right)^{\frac{T_0}{T} - 1}, \quad (2.2.26)$$

Note that the gate voltage dependence has the form of a power law in $V_G - V_T$ [32]. It is worth pointing out that in transistors made with single crystal, the mobility is found to be very seldom gate voltage dependent [35], which indirectly confirms that the V_G dependence originates from localized levels associated with chemical and physical defects.

2.2.5 PARAMETER EXTRACTION

Parameter extraction is a central issue in settling the debates between charge transport mechanisms in organic transistors. Before depicting in more details the different methods developed for parameter extraction, let us first go back to Equations (2.2.1) and (2.2.2) and their relevance to actual current-voltage curves. Because the drain current I_D depends on two independent voltages — the drain voltage V_D and the gate voltage V_G — the current-voltage (I–V) curves can be plotted in two ways: the *output characteristic*, where a set of drain current versus drain current curves is drawn for various values of the gate voltage, and the *transfer characteristic*, in which the drain current is plotted as a function of the gate voltage for a given drain voltage. Both representations are shown in Figure 2.2.10.

Parameter extraction mainly involves mobility and threshold voltage. Because of the very simple analytical form of Equation (2.2.2), the most widespread technique to extract mobility and threshold voltage consists of plotting the square-root of I_{Dsat} as a function of gate voltage in the saturation regime (that is, measured at a drain voltage higher than the gate voltage). However, it must be remembered that the simplicity of Equation (2.2.2) implies two assumptions: (1) gradual channel approximation; and (2) constant mobility. There are now several pieces of evidence that the second criterion is not fulfilled in organic transistors. One is the previously developed trapping model, which predicts that mobility increases with gate voltage. A second one, which will be analyzed in the following, is mobility degradation, a process by which mobility tends to decrease as the gate voltage increases.

Why the saturation regime poses a problem to extracting parameters under these circumstances is illustrated in Figure 2.2.11.

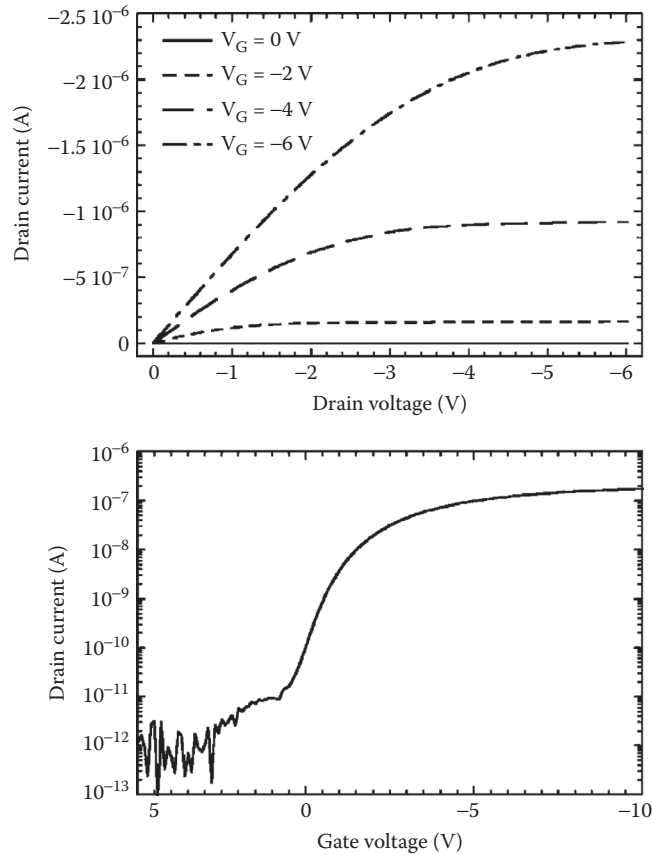


FIGURE 2.2.10 Output (left) and transfer (right) characteristics of an organic transistor.

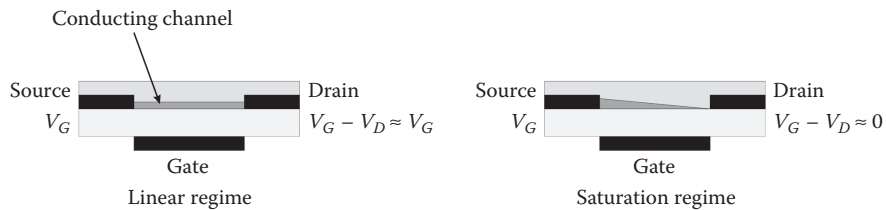


FIGURE 2.2.11 Charge distribution along the channel in a thin-film transistor. In the linear regime (left), the voltage at source and drain is nearly identical, so the charge density is constant along the channel. In the saturation regime (right), the voltage is V_G at source and practically zero at drain, and the charge density drops to zero when passing from source to drain. Note that the thickness of the channel represents the charge density, not its spatial extension.

The transistor must be thought of as a two-dimensional structure, a crucial consequence being that the voltages at source and drain are not necessarily equal; more precisely, the voltage is V_G at source and $V_G - V_D$ at drain, so, depending on the respective values of V_G and V_D , the electrical potential at the insulator–semiconductor interface may not be constant all along the channel. In the linear regime, $V_D \ll V_G$, the potential does not noticeably vary. This is not the case in the saturation regime, where $V_D \geq V_G$. When reaching the so-called pinch-off voltage ($V_D \approx V_G - V_T$), the voltage at the drain drops to zero, and the potential along the channel decreases from V_G to zero when passing from the source to the drain. Beyond the pinch-off voltage, the pinch-off point gradually moves towards the source, and the potential variation along the channel retains this magnitude. If the mobility is gate-bias dependent, an exact estimation of the saturation current would require integrating the mobility all along the channel, which does not appear easily feasible because the gate-voltage dependence of the mobility for a given device is not known beforehand. For this reason, parameter extraction from the linear regime is the preferred technique in conventional MOSFETs and will be the one adopted here.

2.2.5.1 THRESHOLD VOLTAGE

In conventional MOSFETs, the threshold voltage is an important technological parameter that plays a crucial role in circuit modeling. For this reason, numerous methods have been developed to extract the threshold voltage; most of them are performed in the linear regime. A recent review of these methods can be found in Ortiz-Conde et al. [36]. As already stated, the quasi-universal method used in OTFTs consists of plotting the square root of the saturation current as a function of the gate voltage. According to Equation (2.2.2), this should result in a straight line that crosses the V_G axis at $V_G = V_T$. However, because of several effects, such as gate-voltage dependent mobility and contact resistance, the actual curve is not a real straight line. Instead, it presents an upward curvature at low gate voltages and a downward curvature at high voltages. A representative example is given in Figure 2.2.12. On this kind of curve, the extracted mobility and threshold voltage largely depend on the voltage range used for the linear fitting. The most widespread usage is to center the linear regression curve around the inflection point, but the basis for doing so is purely empirical.

To illustrate an alternative method to extract V_T in the linear regime, we have selected the transconductance change (TC) method developed by Wong and coworkers [37], which consists of plotting the second derivative of the linear drain current as a function of gate voltage (Figure 2.2.13). In this case, V_T is given by the peak of the curve. Importantly, such a determination is insensitive to both the contact resistance and the gate-voltage dependence of the mobility.

2.2.5.2 CONTACT RESISTANCE

2.2.5.2.1 Contact Resistance Extraction

Contact resistance extraction cannot be performed from simple current-voltage curve. At this stage, specific techniques that allow an independent access to the

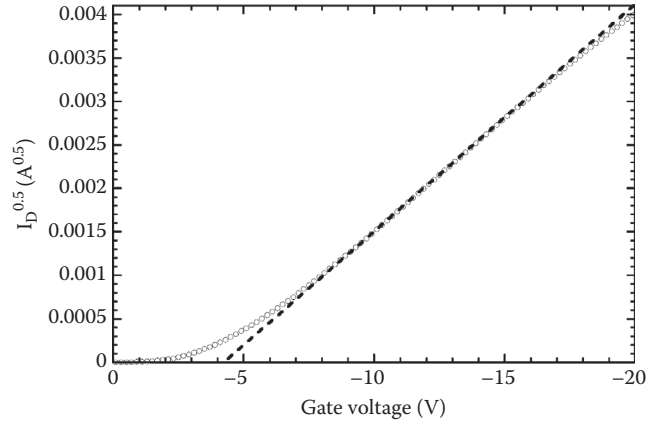


FIGURE 2.2.12 Representative example of an actual $\sqrt{I_{Dsat}}$ versus V_G curve. The dotted line is a linear fit to the data ranging between -10 and -15 V. Note the upward curvature of the curve at low gate voltage and its downward curvature at high voltage.

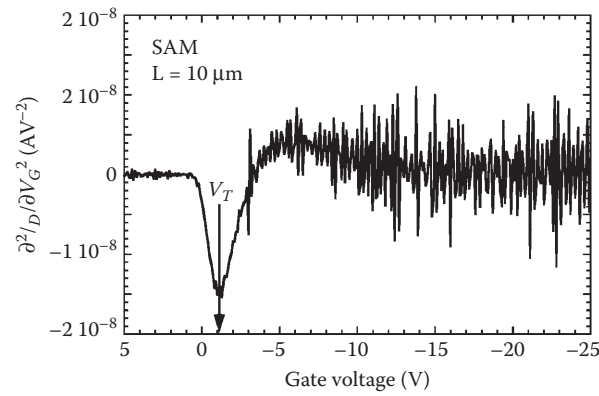


FIGURE 2.2.13 TC method for the extraction of the threshold voltage from the linear regime.

channel and contact resistances are needed. A first technique is the transfer line method (TLM) [38–41], a method adapted from a classical technique to estimate contact resistance, and first adopted in the case of the amorphous silicon thin-film transistor [42]. The method consists of measuring the channel resistance of similar devices with various channel lengths. The measured resistance is actually the sum of the channel and contact resistances. As long as the measurement is performed in the linear regime (small drain voltage), the channel resistance is proportional to L (see Equation (2.2.1)) and the width-normalized ($R \times W$) total resistance is given by

$$R \times W = \frac{L}{C_i \mu (V_G - V_T)} + R_c \times W \quad (2.2.27)$$

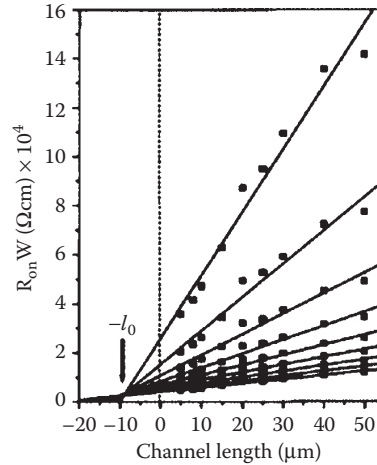


FIGURE 2.2.14 Illustration of the transfer line method. (From Zaumseil, J. et al., *J. Appl. Phys.*, 93, 6117, 2003.)

The contact resistance is extracted by plotting the width-normalized resistance as a function of channel length. The extrapolation to zero length readily gives the contact resistance, while the slope of the curve can be used to extract device parameters. The method is exemplified in Figure 2.2.14.

Each line corresponds to a given gate voltage. Figure 2.2.14 shows that the contact resistance is actually gate voltage dependent; that is, it decreases when gate voltage increases. The reason for such a behavior will be given in the next section.

However, the TLM presents several drawbacks. First of all, it requires measurements on different devices, and it cannot be taken for granted that the channel and contact resistances are strictly similar for all of them, even if they are prepared during the same run. This is the reason why scattering appears when plotting the data, as shown in Figure 2.2.14. Next, the validity of Equation (2.2.27) requires that the contact resistance follows Ohm's law. In other words, the method cannot be used in the case of nonlinear contact resistance. It must also be noted that, as the method requires measurements in the linear regime (that is, at low drain voltages), it is very sensitive to leaks through the insulator. Finally, the method cannot make a distinction between the contact resistance at the source and that at the drain. This last point has its importance; theoretical modeling predicts that in the case of ideal contacts, all the ohmic drop should occur at the source electrode.

An alternative method to TLM is the four-point probe, which consists of introducing in the conducting channel two additional electrodes [44,51]. Being a conservative magnitude, the current remains the same all along the channel and the voltage drop between these two additional electrodes is not affected by the contact resistance, thus giving access to the true channel resistance. Moreover, as shown in Figure 2.2.15, the contact resistance at each side of the channel can now be independently estimated.

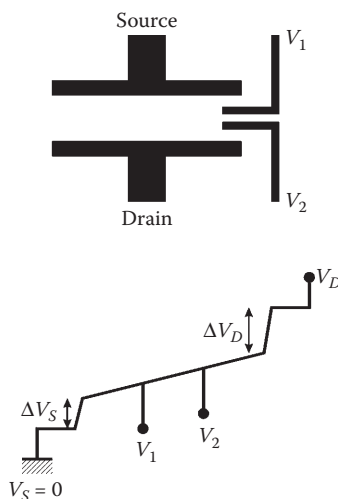


FIGURE 2.2.15 Principle of the four-probe technique.

2.2.5.2.2 Origin of Contact Resistance

The most commonly used image to describe source and drain contacts is that of a metal–semiconductor junction. According to the conventional Mott–Schottky (MS) model [18], contacts are expected to be ohmic when the work function of the metal is close to the HOMO or LUMO level of the semiconductor, depending on whether the semiconductor is *p*- or *n*-type. If the reverse situation prevails, an energy barrier forms at the metal–semiconductor interface, leading to poor charge injection. From this standpoint, the Au–pentacene interface would be a good candidate as low-resistance contact because the ionization potential *IP* of pentacene, which measures the energy distance between the HOMO level and the vacuum level E_{vac} , is close to the work function Φ of gold (see Figure 2.2.16). In practice, the actual resistance is rather high. The mechanism of barrier formation at metal–organic semiconductor interfaces has been studied in great detail in the field of organic light-emitting diodes

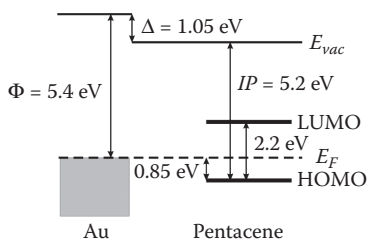


FIGURE 2.2.16 Actual energy level alignment in the Au-pentacene junction as determined by UV photoelectron spectroscopy. (Adapted from [45].)



(OLEDs), where contact resistance is a crucial issue too. UV photoelectron spectroscopy (UPS) and inverse UPS have been used to precisely determine the energy levels at both sides of the interface [45]. A typical result for the Au–pentacene interface is shown in Figure 2.2.16, which clearly shows that the actual interface strongly deviates from the MS model.

Instead, the interface exhibits an additional “dipole” barrier Δ that shifts the vacuum level upward by more than 1 eV, hence increasing the barrier height by the same amount. The rather large interface dipole is explained by the fact that the electron density at a metal surface presents a tail that extends from the metal free surface into vacuum, thus forming a dipole pointing at the metal bulk. Molecules deposited on the metal tend to push back this tail, thus reducing the surface dipole and decreasing the work function of the metal.

The previously described four-probe technique [44,51] allows a separate determination of the source and drain contact resistances. If contacts would behave as Schottky barriers, one would expect the voltage drop at source to be substantially higher than that at drain. This is what is indeed observed with “bad” contacts. However, “good” contacts show comparable drops at both electrodes. A possible origin of this behavior has been recently put forward [46]. The model assumes that the regions immediately adjacent to the electrodes are made of organic material of quality different from that of the rest of the conducting channel, with very low mobility.

It is worth pointing out that top contacts usually offer lower contact resistance than bottom contacts. The asymmetry of the organic-metal contact, depending on whether the organic film is deposited on the metal or the metal on the organic layer, has been studied from both the theoretical [47] and experimental [48] points of view. For instance, combined UPS and XPS measurements have demonstrated that the deposition of gold atop a pentacene layer shows signs of metal penetration coupled with the formation of metal clusters, leading to a substantial reduction of the interface barrier from 1 to 0.3 eV.

2.2.5.3 MOBILITY DEGRADATION

Gate-voltage dependent mobility has already been dealt with in the case of trap-limited transport; in this circumstance, mobility increases with gate voltage. Another well-documented source of dependence in conventional MOSFETs is the so-called *mobility degradation*, which results in a reverse effect; that is, mobility *decreases* with gate voltage. Mobility degradation is attributed to various scattering agents in the vicinity of the insulator interface: namely, charged centers, surface phonons, and surface roughness [49]. A usual way to describe this behavior is to introduce the so-called mobility degradation factor θ , which in its simplest formulation leads to a mobility that looks like

$$\mu = \frac{\mu_0}{1 + \theta(V_G - V_T)}. \quad (2.2.28)$$



A similar trend has been recently also observed in OTFT [50–52]. To account for this decrease, a model has been developed that takes advantage of the particular structure found in semiconductor films made of short molecules. Such molecules can be viewed as rigid rods, which in the solid state assemble parallel to each other, thus forming parallel layers, the thickness of which equals the length of the molecule (minus a small correction to account for a tilt angle). Taking into consideration that (1) each molecule can bear only one charge carrier and (2) the charge practically extends over the entire molecule [53], one can assimilate the film to a stack of n dielectric layers of thickness d , each layer bearing a uniform density of carriers n_i . The calculation of the charge distribution has been performed by Horowitz and coworkers [54]. Layers are numbered starting from the insulator–semiconductor interface. To calculate the charge-carrier density n_i (per unit area) in the i th layer, let us apply Gauss's law to a cylinder of unit cross-section limited by the boundary between the $(i - 1)$ th and the i th layers and that between the i th and the $(i + 1)$ th layers. Within the gradual channel approximation, the electric field F is perpendicular to the layer so that

$$F_{i-1} - F_i = -\frac{qn_i}{\epsilon_s} \quad (2.2.29)$$

where F_i is the module of the electric field at the boundary between the i^{th} and the $(i + 1)$ th layers.

Because the charge density is constant in each layer, the electric field varies linearly between two boundaries, which in turn implies that the potential is quadratic within the same limits. Furthermore, assume that charge transfer between adjacent layers is sufficiently efficient so that the distribution of charge in the whole film is at thermal equilibrium. This yields

$$\frac{n_{i+1}}{n_i} = \exp\left[-\frac{kT}{q}(V_i - V_{i+1})\right] \quad (2.2.30)$$

After some manipulation, the following series of equations is found:

$$n_i = n_{i+1} \exp\left[\frac{dq^2}{kT\epsilon_s}\left(\frac{n_{i+1}}{2} + \sum_{j=i+2}^n n_j\right)\right] \quad (2.2.31)$$

The gate-voltage dependent charge distribution across the conducting channel can be obtained by starting from an arbitrary value of the density of charge in the n th layer and cascading down to the first layer. The gate voltage is then calculated from the total density of charge carriers.

$$qn_{\text{tot}} = q \sum_1^n n_i = C_i V_G \quad (2.2.32)$$

Figure 2.2.17 shows the calculated relative distribution of charge in the case of a 30-nm thick pentacene film. Note that with a monolayer of around 1.5 nm, 30 nm of pentacene represents 20 layers. It is immediately seen that as the gate voltage increases, the charge gradually concentrates in the first layer. The decrease of the effective mobility is then attributed to the fact that the mobility in this first layer is likely to be degraded by the various effects mentioned earlier. The layers can now be regarded as parallel conductors, so the total conductance of the film equals the sum of the mobility times the density of charge in each layer. If the mobility is lower in the first layer, the effective mobility decreases with gate voltage because the proportion of charge carriers in the first layer increases. An alternative way to describe mobility degradation is to say that charge trapping is more pronounced at the insulator–semiconductor interface, thus reducing the density of free carriers.

2.2.6 CONCLUDING REMARKS

Charge transport in organic semiconductors is the result of an interplay between intramolecular and intermolecular effects. The most remarkable consequence of such an interplay is that, unlike what occurs in their inorganic counterparts, charge carriers in organic semiconductors can no longer be viewed as bare particles; instead, they are dressed by a polarization cloud that follows their movement, thus leading to the formation of polarons. Polarons are the main reason why mobility is substantially lower in organic semiconductors than in their inorganic counterpart. Another important consequence of this interplay is that the electronic properties of a conjugated organic solid depend on the chemical structure of the individual molecules and are also strongly determined by the crystalline structure of the solid. Because of that, theoretical calculations on charge transport in conjugated organic materials are intricate, and a predictive theory is still lacking.

Additional limitations to charge transport occur in thin-film conductors. These limitations concentrate at the interfaces of the device: namely, the metal–semiconductor and insulator–semiconductor interfaces. The former is responsible for limitations by contact resistance, while problems with the latter arise from the fact that defects tend to concentrate at this interface, thus leading to a degradation of charge transport. Under these circumstances, parameter extraction is not straightforward and often requires measurements on devices with various geometries. Recent results on organic transistors made of highly pure and carefully crystallized materials have shown that mobility can reach the 10 cm²/Vs range [55], thus giving hope for further improvements.

ACKNOWLEDGMENTS

Most of the experimental work on which this chapter is based was performed while the author was at the Laboratoire des Matériaux Moléculaires, CNRS, directed by Francis Garnier. The author gratefully acknowledges his past and present coworkers Abderrahim Yassar, Zhi-Gang Xu, Xue-Zhou Peng, Denis Fichou, Bai Xu, Didier Delabouglise, Mohamed Hmyene, Françoise Deloffre, Fayçal Kouki, Philippe Lang,

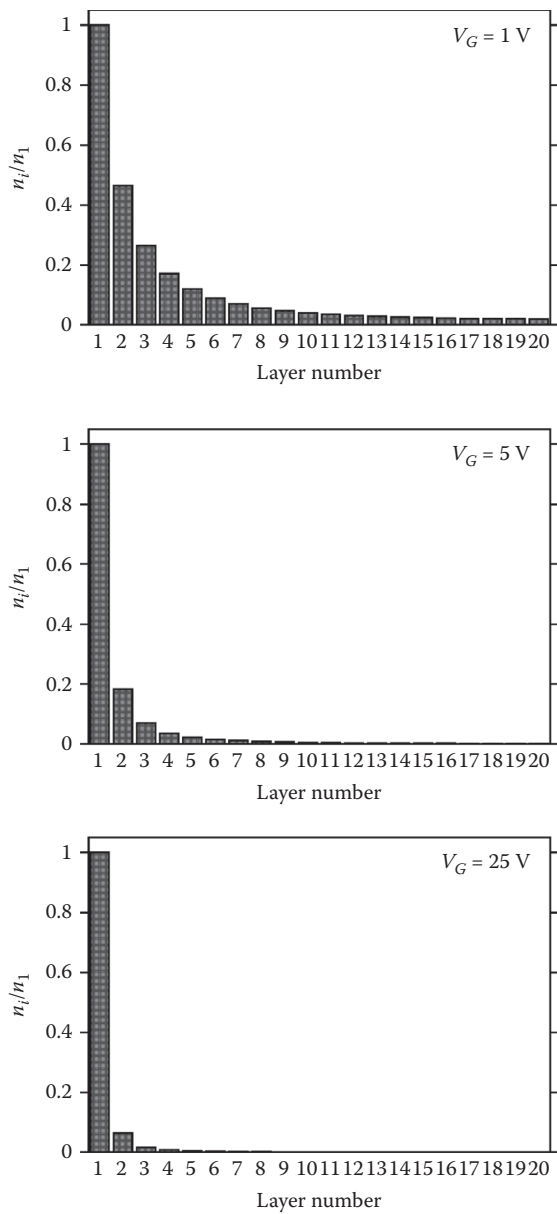


FIGURE 2.2.17 Relative distribution of charge in a 20-layer (30-nm) thick pentacene film for three different values of the gate voltage.

Riadh Hajlaoui, Frédéric Demanze, Pratima Srivastava, Claude Noguès, Xavier Pan, Peter Spearman, Belkasssem Nessakh, Ahmed El Kassmi, Mohammad Mottaghi, and Wolfgang Kalb. He is indebted to Philippe Delannoy, Jean-Luc Brédas, Jérôme Cornil, Fabio Biscarini, Antoine Kahn, Jean-Noël Chazalviel, and Libero Zuppiroli for stimulating discussions and fruitful collaborations.

REFERENCES

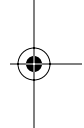
1. Ashcroft, N. W. and Mermin, N. D., *Solid state physics*, Holt, New York, 1976.
2. Wright, J. D., *Molecular crystals*, 2nd ed., Cambridge University Press, Cambridge, 1995.
3. Gutman, F. and Lyons, L. E., *Organic semiconductors*, John Wiley, New York, 1967.
4. Meier, H., *Organic semiconductors: Dark- and photoconductivity of organic solids*, Verlag Chemie, Weinheim, 1974.
5. Eley, D. D., Phthalocyanines as semiconductors, *Nature*, 162, 819, 1948
6. Vartanyan, A. T., Semiconductor properties of organic dyes. I. Phthalocyanines. *Zh. Fiz. Khim.*, 22, 769, 1948.
7. Vartanyan, A. T., Semiconductivity of organic dyes. II. Trypaflavine, *Zh. Fiz. Khim.*, 24, 1361, 1950.
8. Vartanyan, A. T., Semiconductive properties of organic dyes, *Izv. Akad. Nauk SSSR*, 16, 169, 1952.
9. Eley, D. D. et al., Semiconductivity of organic substances. I, *Trans. Faraday Soc.*, 49, 79, 1953.
10. Eley, D. D. and Parfitt, G. D., Semiconductivity of organic substances. II, *Trans. Faraday Soc.*, 51, 1529, 1955.
11. Pope, M. and Swenberg, C. E., *Electronic processes in organic crystals and polymers*, 2nd ed., Oxford University Press, New York, 1999.
12. Tang, C. W. and van Slyke, S. A., Organic electroluminescent diodes, *Appl. Phys. Lett.*, 51, 913, 1987.
13. Horowitz, G. et al., A field-effect transistor based on conjugated alpha-sexithienyl, *Solid State Commun.*, 72, 381, 1989.
14. Lilienfeld, J. E., U.S. Patent 1,745,175, 1930.
15. Kahng, D. and Atalla, M. M., Silicon-silicon dioxide field induced surface devices, in IRE Solid-State Devices Research Conference, Pittsburgh, PA, 1960.
16. Heilmeyer, G. H. and Zaroni, L. A., Surface studies of alpha-copper phthalocyanine films, *J. Phys. Chem. Solids*, 25, 603, 1964.
17. Koezuka, H., Tsumura, A., and Ando, T., Field-effect transistor with polythiophene thin-film, *Synth. Metal.*, 18, 699, 1987.
18. Sze, S. M., *Physics of semiconductor devices*, 2nd ed., John Wiley, New York, 1981.
19. Karl, N. et al., High-field saturation of charge carrier drift velocities in ultrapurified organic photoconductors, *Synth. Metal.*, 42, 2473, 1991.
20. Silinsh, E. A. and Cápek, V., *Organic molecular crystals: Interaction, localization, and transport phenomena*, AIP Press, New York, 1994.
21. Sato, N., Inokuchi, H., and Silinsh, E. A., Reevaluation of electronic polarization energies in organic molecular crystals, *Chem. Phys.*, 115, 269, 1987.
22. Kenkre, V. M. et al., Unified theory of the mobilities of photoinjected electrons in naphthalene, *Phys. Rev. Lett.*, 62, 1165, 1989.

23. Marcus, R.A., Chemical and electrochemical electron-transfer theory, *Ann. Rev. Phys. Chem.*, 15, 155, 1964.
24. Newton, M.D., Quantum chemical probes of electron-transfer kinetics: The nature of donor–acceptor interactions, *Chem. Rev.*, 91, 767, 1991.
25. Marcus, R.A., Electron transfer in chemistry. Theory and experiment, *Rev. Mod. Phys.*, 65, 599, 1993.
26. Pope, M. and Swenberg, C. E., *Electronic processes in organic crystals and polymers*, 2nd ed., Oxford University Press, New York, 1999.
27. Brédas, J.-L. et al., Charge-transfer and energy-transfer processes in *p*-conjugated oligomers and polymers: A molecular picture, *Chem. Rev.*, 104, 4971, 2004.
28. Gill, W. D., Drift mobilities in amorphous charge-transfer complexes of trinitrofluorenone and poly-*n*-vinylcarbazole, *J. Appl. Phys.*, 43, 5033, 1972.
29. Bäessler, H., Charge transport in disordered organic photoconductors, *Phys. Stat. Sol. (b)*, 175, 15, 1993.
30. Miller, A. and Abrahams, E., Impurity conduction at low concentrations, *Phys. Rev.*, 120, 745, 1960.
31. Le Comber, P. G. and Spear, W. E., Electronic transport in amorphous silicon films, *Phys. Rev. Lett.*, 25, 509, 1970.
32. Horowitz, G., Hajlaoui, R., and Delannoy, P., Temperature dependence of the field-effect mobility of sexithiophene. Determination of the density of traps, *J. Phys. III France*, 5, 355, 1995.
33. Völkel, A. R., Street, R. A., and Knipp, D., Carrier transport and density of state distributions in pentacene transistors, *Phys. Rev. B*, 66, 195336, 2002.
34. Horowitz, G., Hajlaoui, M. E., and Hajlaoui, R., Temperature and gate voltage dependence of hole mobility in polycrystalline oligothiophene thin film transistors, *J. Appl. Phys.*, 87, 4456, 2000.
35. Stassen, A. F. et al., Influence of the gate dielectric on the mobility of rubrene single-crystal field-effect transistors, *Appl. Phys. Lett.*, 85, 3899, 2004.
36. Ortiz-Conde, A. et al., A review of recent MOSFET threshold voltage extraction methods, *Microelectronics Reliability*, 42, 583, 2002.
37. Wong, H.-S. et al., Modeling of transconductance degradation and extraction of threshold voltage in thin oxide MOSFETs, *Solid-State Electron.*, 30, 953, 1987.
38. Necliudov, P. V. et al., Contact resistance extraction in pentacene thin film transistors, *Solid-State Electron.*, 47, 259, 2003.
39. Zaumseil, J., Baldwin, K. W., and Rogers, J. A., Contact resistance in organic transistors that use source and drain electrodes formed by soft contact lamination, *J. Appl. Phys.*, 93, 6117, 2003.
40. Klauk, H. et al., Contact resistance in organic thin film transistors, *Solid-State Electron.*, 47, 297, 2003.
41. Meijer, E. J. et al., Scaling behavior and parasitic series resistance in disordered organic field-effect transistors, *Appl. Phys. Lett.*, 82, 4576, 2003.
42. Luan, S. and Neudeck, G. W., An experimental study of the source/drain parasitic resistance effects in amorphous silicon thin film transistors, *J. Appl. Phys.*, 72, 766, 1992.
43. Chesterfield, R. J. et al., Variable temperature film and contact resistance measurements on operating *n*-channel organic thin film transistors, *J. Appl. Phys.*, 95, 6396, 2004.
44. Yagi, I., Tsukagoshi, K., and Aoyagi, Y., Direct observation of contact and channel resistance in pentacene four-terminal thin-film transistor patterned by laser ablation method, *Appl. Phys. Lett.*, 84, 813, 2004.



45. Koch, N. et al., Conjugated organic molecules on metal versus polymer electrodes: Demonstration of a key energy level alignment mechanism, *Appl. Surf. Sci.*, 82, 70, 2003.
46. Li, T. et al., Investigation of bottom-contact organic field effect transistors by two-dimensional device modeling, *J. Appl. Phys.*, 93, 4017, 2003.
47. Tessler, N. and Roichman, Y., Two-dimensional simulation of polymer field-effect transistor, *Appl. Phys. Lett.*, 79, 2987, 2001.
48. Watkins, N. J., Yan, L., and Gao, Y., Electronic structure symmetry of interfaces between pentacene and metals, *Appl. Phys. Lett.*, 80, 4384, 2002.
49. van Langevelde, R. and Klaassen, F. M., Effect of gate-field dependent mobility degradation on distortion analysis in MOSFETs, *IEEE Trans. Electron Devices*, 44, 2044, 1997.
50. Kalb, W. et al., Structure–performance relationship in pentacene/Al₂O₃ thin-film transistors, *Synth. Metal.*, 146, 279, 2004.
51. Chesterfield, R. J. et al., Variable temperature film and contact resistance measurements on operating *n*-channel organic thin film transistors, *J. Appl. Phys.*, 95, 6396, 2004.
52. Merlo, J. A. et al., *p*-Channel organic semiconductors based on hybrid acene-thiophene molecules for thin-film transistor applications, *J. Am. Chem. Soc.*, 127, 3997, 2005.
53. Sancho-Garcia, J. C. et al., Effect of an external electric field on the charge transport parameters in organic molecular semiconductors, *J. Chem. Phys.*, 119, 12563, 2003.
54. Horowitz, G. and Mottaghi, M., Depth dependent mobility in pentacene thin-film transistors, *Phys. Rev. B*, in press.
55. de Boer, R. W. I. et al., Organic single-crystal field-effect transistors, *Phys. Stat. Sol. (a)*, 201, 1302, 2004.







2.3 Charge Transport Physics of Solution- Processed Organic Field-Effect Transistors

Henning Sirringhaus

CONTENTS

2.3.1	Introduction	103
2.3.2	Solution-Processable p-Type Organic Semiconductors	106
2.3.2.1	Conjugated Polymers	106
2.3.2.2	Solution-Processable Small Molecules	110
2.3.3	Solution-Processable n-Type Organic Semiconductors	111
2.3.4	Gate Dielectrics.....	112
2.3.5	Charge Transport Physics	115
2.3.6	Charge Injection Physics	124
2.3.7	Defect States and Device Degradation Mechanisms.....	127
2.3.8	Outlook.....	130
	References.....	130

TS: insert
ToC.

2.3.1 INTRODUCTION

The semiconducting properties of conjugated polymers allow realization of a range of electronic and optoelectronic devices, such as light-emitting diodes (LEDs) [1], photovoltaic diodes [2], and field-effect transistors (FETs) [3]. Following the initial demonstration of field-effect conduction in small organic molecules [4,5] and conjugated polymers [3,6,7], for several years the field-effect transistor was merely a convenient experimental tool to probe the charge transport properties of undoped polymer semiconductors, circumventing the need for chemical doping to be able to measure electrical transport. Its potential for technological applications was limited by the then insufficient field-effect mobility of polymer semiconductors of typically less than 10^{-4} cm²/Vs and the relatively poor environmental stability of materials such as polyacetylene and polythiophene. However, since then field-effect transistors based on solution-processable organic semiconductors have experienced impressive

improvements in both performance and reliability as a result of a variety of different factors, including:

- availability of polymer materials with lower density of chain defects, better chemical purity, and higher molecular weights
- more controlled polymer processing guided by better understanding of the required thin-film microstructure
- better understanding of the requirements for the gate dielectric forming the active interface with the semiconducting layer and of the charge injecting source-drain contacts
- development of more controlled solution and printing-based device manufacturing processes

As a result, the performance of OFETs, which is generally benchmarked against that of amorphous silicon (a-Si) thin-film transistors (TFTs) with field-effect mobilities of 0.5–1 cm²/Vs and ON–OFF current ratio of 10⁶–10⁸ has improved significantly. Currently, the record mobility values for OFETs are 5 cm²/Vs in the case of vacuum-deposited small molecules [8] and 0.6 cm²/Vs for solution-processed polymers [9]. Even more importantly, very significant progress has been made on developing materials that allow combining high mobilities with good materials stability under air, moisture, and light exposure.

OFETs are most commonly manufactured using standard top-gate (Figure 2.3.1a) and bottom-gate TFT architectures. Figure 2.3.1(b) shows the output characteristics of a state-of-the-art, unencapsulated polymer FET. The figure compares measurements performed in ambient air and light directly after device manufacture and several weeks later, after the device had participated in a customer trial and had crossed the Atlantic twice [10]. No evidence for device degradation is observed.

As a result, there is now a serious level of industrial interest in using OFETs for applications currently incompatible with the use of a-Si or other inorganic transistor technologies. One of their main technological attractions is that all the layers of an OFET can be deposited and patterned at low room temperature by a combination of low-cost, solution-processing, and direct-write printing, which makes them ideally suited for realization of low-cost, large-area electronic functions on flexible substrates (for a review, see Sirringhaus et al. [11] and Forrest [12]). The first applications in which we can realistically expect OFETs to be used within the next three to five years are flexible, active matrix electronic paper displays [10,13] and simple, low-cost radio frequency identification (RFID) tags [14] and sensing devices. In particular, in the case of electronic paper displays there seems to be an excellent match between present technological capabilities and application requirements.

To illustrate the current capabilities of OFET technology in this application area, Figure 2.3.2 shows an optical micrograph of an A5 active matrix display demonstrator on a flexible polyethyleneterephthalate (PET) substrate made by Plastic Logic. The display was fabricated by laminating the OFET backplane with an E Ink® Imaging Film. The display has a resolution of 100 pixels per inch (ppi) and displays four levels of gray. It contains 480,000 solution-processed OFETs (600 × 800 rows and columns). No substrate encapsulation is needed. The display exhibits excellent

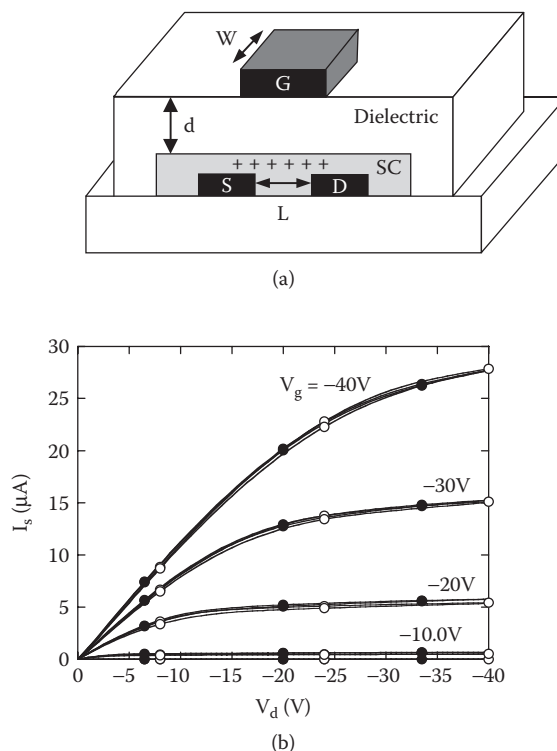


FIGURE 2.3.1 (a) Schematic diagram of top-gate OFET using a standard TFT device architecture. (b) Output characteristics of state-of-the-art, unencapsulated OFET measured in air and light (closed symbols = device measured after manufacture; open symbols = device measured two weeks later).

contrast and can be bent to a radius of curvature of 5 mm. Other, more demanding display applications such as active matrix liquid crystal or organic light-emitting diode (OLED) displays or high-performance RFID tags compatible with existing communication standards are also envisioned, but require a transistor performance with mobilities exceeding $1 \text{ cm}^2/\text{Vs}$, which is still difficult to achieve with solution-processed OFETs.

Through their ability to control the charge carrier concentration electrostatically, rather than chemically, FET devices provide a useful scientific tool for the wealth of fundamental scientific questions regarding the charge transport and charge injection physics of organic semiconductors and their structure–property relationships. Significant effort has been devoted to understanding the fundamental electronic structure of the organic semiconductor — in particular, at the interface with the dielectric — and how microscopic molecular-scale transport processes determine the electrical characteristics of macroscopic devices. This is a challenging task because of the complex microstructure of solution-processed organic semiconductors, which in many cases cannot be fully characterized by conventional diffraction and microscopy techniques. An important related topic is the understanding of

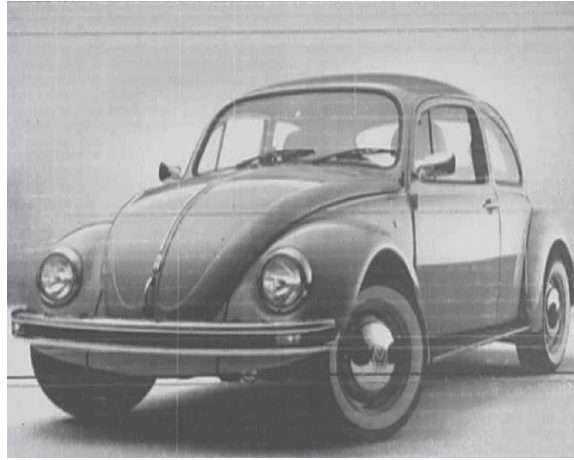


FIGURE 2.3.2 Photograph of A5, 600 × 800 electronic paper display on a flexible PET substrate display comprising an active matrix of OFETs on a PET substrate laminated with an E Ink® Imaging Film. (Courtesy of Plastic Logic Ltd.)

electronic defects states and associated device degradation mechanisms, which are becoming an increasingly important topic as OFETs are nearing their introduction into first products with strict reliability and lifetime requirements.

This section is focused on providing an up-to-date review of the state of knowledge of the materials, device, and charge transport physics of solution-processed OFETs. Sections 2.3.2 and 2.3.3 discuss the materials physics of solution-processable *p*- and *n*-type organic semiconductors, respectively. Section 2.3.4 is devoted to the important topic of solution-processable gate dielectrics, which determine critically the performance as well as the reliability of OFETs. Section 2.3.5 focuses at a more fundamental level on the electronic structure of solution-processed organic semiconductors, the charge transport processes at the active interface, and how these are affected by disorder and molecular relaxation effects. Section 2.3.6 discusses the charge injection physics at the source-drain contacts. Finally, in Section 2.3.7, we review the current understanding of electronic defect states and degradation mechanisms in OFETs, which lead to device instabilities and threshold voltage shifts upon bias stressing and/or environmental exposure.

2.3.2 SOLUTION-PROCESSABLE *P*-TYPE ORGANIC SEMICONDUCTORS

2.3.2.1 CONJUGATED POLYMERS

Two different approaches to high-performance, solution-processable polymer semiconductors have emerged. The first approach is based on achieving high charge carrier mobilities by designing the material to exhibit microcrystalline [15] or liquid-crystalline [16] order through self-organization or by making use of specific interactions with a templating substrate. The second approach aims to produce a com-

pletely amorphous microstructure to provide a uniform path for charge transport along which carriers experience a minimum degree of site energy fluctuations. Although the first approach is likely to lead to higher mobilities eventually, impressive device performance and stability have been demonstrated with the second approach recently.

Amorphous polymers: Early FET studies on amorphous, disordered conjugated polymers, such as regioirregular polythiophene [7] or polyacetylene [17] suggested that field-effect mobilities in amorphous microstructures might be limited to low values $< 10^{-3}$ – 10^{-4} cm^2/Vs . However, several groups have recently reported that amorphous polymers based on triarylamine similar to those used in xerographic applications allow achieving high field-effect mobilities of 10^{-3} – 10^{-2} cm^2/Vs , combined with good operating, environmental and photostability. Veres et al. have reported high-performance FETs with field-effect mobilities of up to $1 \cdot 10^{-2}$ cm^2/Vs , low threshold voltage, and good device stability based on a range of polytriarylamine (PTAA) derivatives [18,19]. These are used in combination with apolar, low-k polymer dielectrics (Figure 2.3.3). With structurally related (9,9-dialkylfluorene-alt-triarylamine) (TFB) in contact with benzocyclobutene dielectric, very stable device operation during continuous switching at 120°C without device degradation was demonstrated [20].

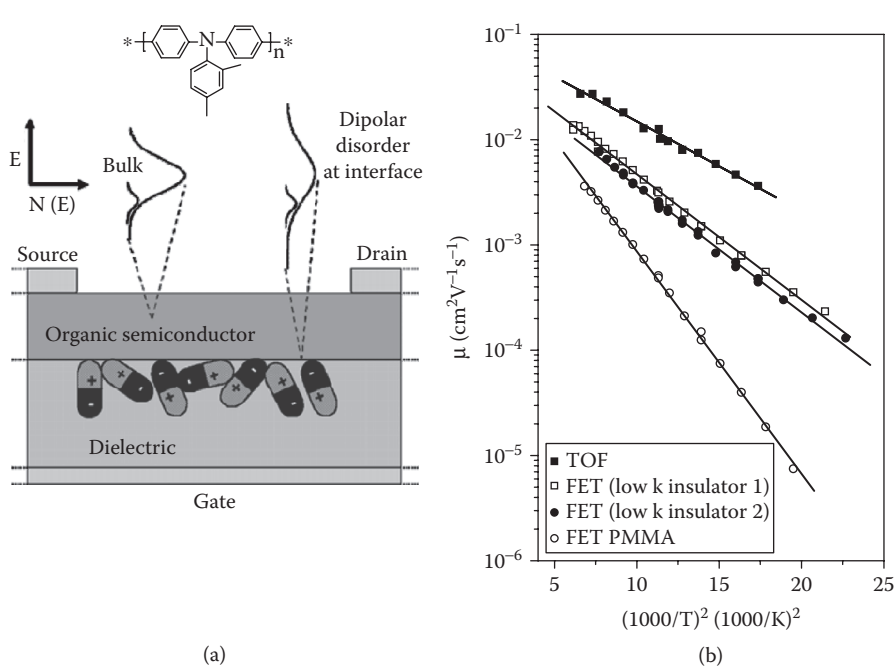


FIGURE 2.3.3 (a) Schematic diagram of the effect of disordered polar groups on the energetic disorder at the active interface (b) Temperature dependence of the time-of-flight and field-effect mobility of PTAA. For the field-effect mobility, data for top-gate FETs with PMMA gate dielectric and two different lower k dielectrics are shown. (From Veres, J. et al., *Adv. Func. Mater.*, 13, 199–204, 2003. Reprinted with permission. Copyright 2003, Wiley.)

Microcrystalline polymers: A prototype microcrystalline polymer is regioregular poly(3-hexylthiophene) (P3HT) [21, 22] with which high field-effect mobilities of 0.1–0.3 cm²/Vs have been achieved. Thin films of P3HT adopt a highly microcrystalline and anisotropic lamellar microstructure comprising two-dimensional conjugated layers with strong π – π interchain interactions separated by layers of solubilizing, insulating side chains (Figure 2.3.4a) leading to fast in-plane charge transport [15]. The microcrystals have been found to have a nanoribbon shape [23–27]. The mobility of P3HT depends very sensitively on the degree of head-to-tail regioregularity [21,22] and deposition conditions [15,21,28].

The mobility of P3HT FETs has also been reported to improve by orders of magnitude upon modification of the SiO₂ gate dielectric substrate by hydrophobic self-assembled monolayers (SAMs), possibly through lowering of the surface energy of the gate dielectric and removal of residual surface water and other polar groups prior to deposition of the polymer [22] or by inducing microstructural changes through specific interactions with functional groups of the polymer [29]. From studies of high molecular weight P3HT films with varying degrees of crystallinity as induced by varying the boiling point of the solvent [26], there is clear evidence that a higher degree of crystallinity generally results in higher mobility.

Recently, much effort has been devoted to understanding the dependence of mobility on molecular weight [24,30–32]. Figure 2.3.4(b) illustrates the dependence of the field-effect mobility on the combined effects of film formation kinetics and molecular weight (MW) [32]. Data for three kinds of deposition conditions are shown: rapid film formation by spin-casting from low-boiling point solvent (chloroform) as well as slow film formation by drop-casting from chloroform and spin-casting from a high boiling point solvent (trichlorobenzene). In this way the microstructure, polymer chain folding, and degree of crystallinity of the polymer film can be controlled. In trichlorobenzene spin-cast devices, the mobility increases sharply with MW from 10⁻³ (M_w = 15.4 and 20 kD) up to 10⁻¹ cm²/Vs (52 kD) and then starts to level off for even higher molecular weight. The MW dependence of mobilities in chloroform drop-cast devices behaves in a similar manner but saturates at a value slightly lower than 10⁻¹ cm²/Vs.

In contrast, in films spin-coated from chloroform, the mobility varies only little between 3 × 10⁻³ to 10⁻² cm²/Vs in an MW range of 15 to 270 kD, but no systematic dependence on MW is found. The behavior in the low mobility regime ($\mu < 10^{-2}$ cm²/Vs) has been attributed to grain boundaries limiting the transport in low molecular weight samples by Kline et al. [24] as well as a more isotropic orientation of polymer crystallites [33]. Zen et al. [30] have explained a similar observation in terms of a less planar polymer backbone in the amorphous regions of the film in the case of low molecular weight fractions. Chang et al. have established a correlation between the mobility and interchain/intrachain disorder as accessed by optical and electro-optical spectroscopy, which suggests that, in the high-mobility regime ($\mu \approx 10^{-1}$ cm²/Vs), the mobility is limited by the crystalline quality of the P3HT nanocrystals as opposed to grain boundaries between the crystals [32].

Since transport in an FET reflects primarily the structure of the semiconducting polymer at the interface as opposed to the bulk, it is important to have experimental probes available that are able to distinguish between interface/surface and bulk micro-

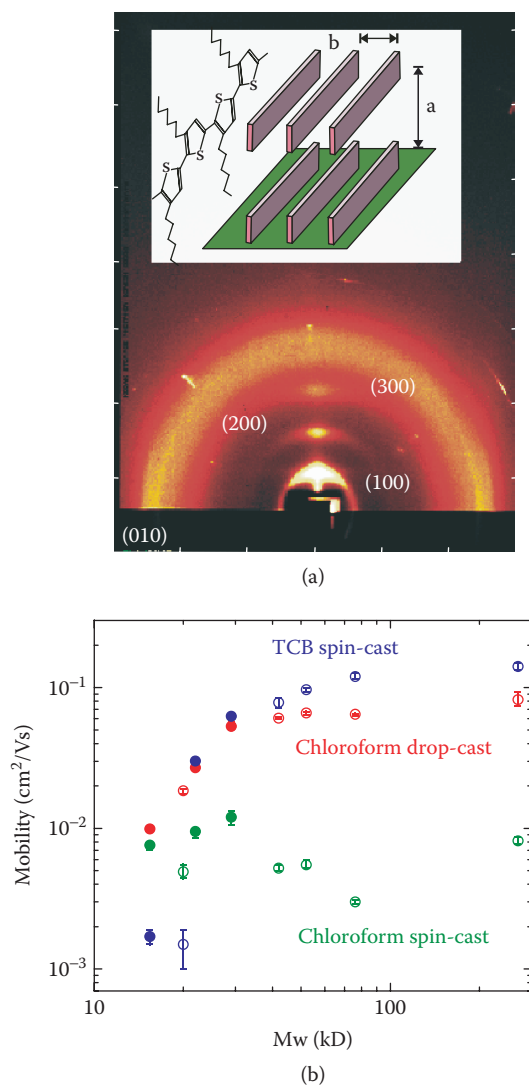


FIGURE 2.3.4 (a) Wide-angle x-ray scattering image of high-mobility P3HT on SiO₂. The inset shows the in-plane, lamellar self-organization of P3HT. (From Sirringhaus, H. et al., *Nature*, 401, 685–688, 1999. Reprinted with permission. Copyright 1999, *Nature*.) (b) Dependence of mobility of P3HT FETs with SiO₂ gate dielectric as a function of molecular weight for different film formation conditions (spin-casting from trichlorobenzene, as well as spin-casting and drop-casting from chloroform).

structure. Kline et al. have recently used x-ray rocking curves to probe selectively the orientation of crystallites at the substrate interface. An exceptional, instrument-limited degree of orientation and a clear correlation between the mobility and the degree of orientation of the P3HT crystals at the interface was found [33].

p-Type semiconducting materials with low ionization potential (typically less than 4.9–5.0 eV), such as regioregular P3HT, tend to exhibit large positive V_T shifts of threshold voltage upon exposure to air, presumably due to doping of the polymer [34]. P3HT is known to form a reversible charge transfer complex with oxygen [35]. Nevertheless, encouraging shelf life stability, albeit with low ON–OFF current ratio of $<10^3$, has been reported for P3HT FETs in a top-gate configuration, which may provide some encapsulation [36]. P3HT has poor photostability when exposed to ultraviolet sunlight in the presence of oxygen, causing formation of carbonyl defects in the polymer with associated loss of conjugation and mobility degradation [37]. The oxidative stability of P3HT can be improved by increasing the ionization potential of the polythiophene backbone by disrupting its ability to adopt a fully planar conformation through the side-chain substitution pattern [38] or by incorporating partially conjugated co-monomers into the main chain [9,39]. These materials maintain the beneficial microcrystalline, lamellar self-organization motive of the parent P3HT polymer. As a result, they exhibit similar or even somewhat higher field-effect mobilities, but have significantly improved environmental and operating stability.

2.3.2.2 SOLUTION-PROCESSABLE SMALL MOLECULES

An alternative route to solution-processable organic semiconductors is to use small molecule semiconductors that have been designed to be compatible with solution deposition.

Precursor routes: Polycrystalline thin films of a conjugated molecule can be obtained by forming a thin film of a soluble precursor on the substrate with subsequent thermal [40] or irradiative [41] conversion into the fully conjugated form. Pentacene precursors have been shown to yield field-effect mobilities of 0.01–0.1 cm^2/Vs [42] and 0.1–0.8 cm^2/Vs [43] after thermal conversion at 150–200°C. Recently, it was shown that even unsubstituted pentacene can be solution deposited from high-boiling point solvents at elevated temperatures [44]. A precursor route approach to tetrabenzoporphyrin has also been developed [45] that yields field-effect mobilities on SiO_2 of 0.017 cm^2/Vs when converted at a temperatures of 150–200°C. Sexithiophene substituted with ester groups that can be removed by thermolysis at 150–260°C exhibits field-effect mobilities on SiO_2 up to 0.07 cm^2/Vs [46].

Side-chain substitution: Small molecule organic semiconductors can also be rendered solution processable by attachment of flexible side chains. The substitution pattern needs to be designed carefully so that the side chains, which are needed to impart adequate solubility and film forming properties, do not interfere with the ability of the molecule to π -stack. Katz reported side-chain-substituted small molecule semiconductors such as dihexylanthradithiophene [47,48] that can be solution-deposited with mobilities of 0.01–0.02 cm^2/Vs . In bis(hexyl-bithiophene)benzene solution-cast onto a heated SiO_2 substrate, mobilities of up to 0.03 cm^2/Vs were reported [49]. Due to the relatively low solubility of these molecules, growth con-

ditions need to be optimized carefully to prevent aggregation and crystallization of the molecules in solution. This can lead to three-dimensional film morphology with poor connectivity and orientation of the grains in the films.

An interesting new strategy to solution-processable small conjugated molecules such as rubrene has recently been reported [50]. The approach is based on incorporation of a glass-inducing diluent that enables controlled crystallization from an initial amorphous, vitreous state of the organic semiconductor. This leads to high crystalline quality, high mobility of up to $0.7 \text{ cm}^2/\text{Vs}$, and good device stability.

Liquid-crystalline molecules: Small side-chain-substituted molecules that exhibit liquid-crystalline phases at elevated temperatures provide alternative routes to forming highly crystalline thin films from solution. Discotic liquid-crystalline molecules such as hexabenzocoronenes have been uniaxially aligned in thin film form with the columnar axis oriented along the transport direction in the FET by using graphoepitaxy on highly crystalline teflon alignment layers [51] or deposition by zone crystallization [52] with field-effect mobilities up to $0.01 \text{ cm}^2/\text{Vs}$ along the discotic columns. Encouraging device performance has also been obtained for contorted discotic derivatives of hexabenzocoronene [53]. Reactive mesogens based on oligothiophenes with photopolymerisable end groups have been homeotropically aligned on a substrate prior to cross-linking to fix the orientation of the molecules and used as the active FET layer [54].

2.3.3 SOLUTION-PROCESSABLE *n*-TYPE ORGANIC SEMICONDUCTORS

Many organic semiconductors show *p*-type conduction only (i.e., in contact with a SiO_2 gate dielectric); for example, hole accumulation layers can be readily formed for negative gate bias, provided that a source-drain metal with a work function matching the ionization potential of the organic semiconductor is used. However, *n*-type organic semiconductors that exhibit electron transport in contact with a suitably low work function source-drain metal upon application of positive gate bias are comparatively rare, but are needed for realization of complementary logic circuits.

Electron field-effect conduction has been reported in several, relatively high electron affinity ($\text{EA} > 3.5 \text{ eV}$) small molecule organic semiconductors deposited from vacuum phase (for a review, see Dimitrakopoulos and Malenfant [55]) and solution-processed organic semiconductors. High electron-affinity materials are less susceptible to the presence of electron-trapping impurities, since such trapping groups are more likely to be positioned in energy above the LUMO states of the organic semiconductor. It has been shown recently [56] (see Section 2.3.4) that electron conduction is in fact a generic feature of most organic semiconductors, including those with normal electron affinities of $2.5\text{--}3.5 \text{ eV}$, provided that the right dielectric, which avoids trapping of electrons at the interface, is used.

Fluoroalkyl-substituted naphthalenetetracarboxylic diimide can be processed into thin films from fluorinated solvents to yield mobilities of $0.01 \text{ cm}^2/\text{Vs}$ (bottom gate FET with SiO_2 dielectric, and gold contacts) [57]. The ladder polymer poly(benzobisimidazobenzophenanthroline) (BBL) has an electron affinity of $4.0\text{--}4.4 \text{ eV}$ and can be solution processed into microcrystalline thin films from Lewis and methane-

sulfonic acids [58]. High electron mobilities of 0.03–0.1 cm²/Vs were achieved in a bottom gate FET configuration with SiO₂ dielectric measured unencapsulated in air. Solution-processed diperfluorohexyl substituted quinque- and quaterthiophene with electron affinities of 2.8–2.9 eV have been reported to exhibit field-effect mobilities of 4–8 · 10⁻⁴ cm²/Vs (on HMDS treated SiO₂ dielectric with gold contacts).

The devices suffer from a relatively high threshold voltage > 25 V due to electron trapping, which might be related to the relatively low electron affinity of fluoroalkyl substituted thiophene molecules [59]. *n*-Type field-effect conduction has also been reported in methanofullerene phenyl C₆₁-butyric acid methyl ester (PCBM) [60] and 6,6-phenyl-C₇₁-butyric acid methyl ester [61]. In the case of the C₆₀ derivative, field-effect mobilities of 3–4 · 10⁻³ cm²/Vs were achieved in an encapsulated, bottom gate device with an organic dielectric and calcium source-drain contacts. Much lower apparent mobilities were observed with gold or aluminum contacts. For the C₇₀ derivative, the electron mobility is somewhat lower, but the material exhibits better environmental stability than the C₆₀ derivative.

Recently, there has been growing interest in ambipolar organic semiconductors, which, in a device with suitable choice of source-drain contacts, exhibit hole accumulation for negative gate bias and electron accumulation when the gate bias is reversed. One application of ambipolar semiconductors is in light-emitting FETs, which are operated by biasing the gate voltage in between the values of the source and the drain voltage to form a hole accumulation layer near the source contact and an electron accumulation layer near the drain contact. Ambipolar conduction was established in blends of solution-processed hole (poly(methoxy-dimethyloctyloxy)-phenylene vinylene OC₁C₁₀-PPV or P3HT) and electron (PCBM) transporting organic semiconductors by Meijer et al. The electron mobility in such blends (7 · 10⁻⁴ cm²/Vs) was two orders of magnitude lower than the electron mobility of a pure film of PCBM; the hole mobility was similar to that of single-component OC₁C₁₀-PPV (3 · 10⁻⁵ cm²/Vs) [62].

Similarly, Babel reported ambipolar conduction measured in air in blends of BBL and CuPc [63]. Also in this case the electron (1.7 · 10⁻⁴ cm²/Vs) and hole (3 · 10⁻⁵ cm²/Vs) mobilities were several orders of magnitude lower than that of films of the single components. Interestingly, it was possible to improve either the electron or the hole mobility by postdeposition annealing under solvent atmosphere; however, this was associated with the loss of the ambipolar conduction. Shkunov et al. investigated ambipolar transport in blends of polythiophene and PCBM [64]. Ambipolar conduction has also been reported in single-component systems such as low band gap poly(3,9-di-tert-butylindeno[1,2-b]fluorene) (PIF) [62], PCBM [65], and soluble oligothiophene/fullerene donor-acceptor triads [66]. It has been shown recently [56] (see Section 2.3.4) that ambipolar conduction is in fact a generic feature of a number of organic semiconductors, provided that the right dielectric, which avoids trapping of electrons at the interface, is used.

2.3.4 GATE DIELECTRICS

The performance of organic field-effect devices depends critically on the use of high-performance dielectrics that form active interfaces with low defect densities.

In the same way as silicon MOS technology owes much to the quality of the Si–SiO₂ interface, dielectrics for organic FETs have recently received significant attention (for a comprehensive review, see Facchetti et al. [67]). In comparison to inorganic heterointerfaces, many aspects of the physics of charge transport along solution-processed heterointerfaces are still poorly understood. In the present section we will review recent progress in the understanding of these issues and some of the general selection criteria for gate dielectric materials.

For a solution-processed active interface in which the gate dielectric material is deposited from solution onto a solution-processable semiconducting material or vice versa, it is critical to avoid dissolution or swelling effects during deposition of the upper layer, which can lead to interfacial mixing and increased interface roughness. This can be avoided by cross-linking the lower layer; however, this restricts the choice of materials and requires special care to avoid introducing unwanted impurities and trapping groups [68]. The preferred approach is to choose orthogonal solvents for the deposition of the multilayer structure [69]. It has been demonstrated that in this way solution-processed interfaces can be achieved at which the field-effect mobility is as high as that of the corresponding organic semiconductor–SiO₂ interface, for which interfacial mixing is not an issue.

This is somewhat surprising since a solution-processed polymer heterointerface is never atomically abrupt; its width is determined by a balance between entropy favoring a wider interface and the unfavorable energy of interaction between the two polymers [70]. The correlation between interface roughness and mobility in solution-processed OFETs has recently been investigated by Chua et al. [71], who developed an approach for fabricating self-assembled polymer semiconductor–polymer dielectric bilayers making use of vertical phase separation in ternary solutions of semiconducting polymer–gate dielectric–solvent. By varying the speed of solvent removal, the roughness of the phase-separated interface could be varied in a controlled way. The mobility was found to be constant for low values of the interface roughness less than a critical roughness threshold. For roughness exceeding this threshold, a very rapid drop of the mobility by orders of magnitude was observed, even for roughness features of surprisingly long wavelength > 100 nm.

In principle, for a given thickness of dielectric, a high-*k* dielectric is preferable to a low-*k* dielectric for an FET application, which requires the FET to exhibit a high drive current at low drive voltage. Various solution-processable high-*k* dielectrics for low-voltage OFETs have been used in the literature, such as anodized Al₂O₃ [72] ($\epsilon = 8\text{--}10$), TiO₂ [73] ($\epsilon = 20\text{--}41$), or polyvinylphenol loaded with TiO₂ nanoparticles [74] (for a review see Veres et al. [19]). Many polar, high-*k* polymer dielectrics, such as polyvinylphenol ($\epsilon = 4.5$) or cyanoethylpullulan ($\epsilon = 12$), are hygroscopic and susceptible to drift of ionic impurities during device operation and thus cannot be used for ordinary TFT applications [75].

Veres et al. have shown that the field-effect mobilities of amorphous PTAA [18] and other polymers are higher in contact with low-*k* dielectrics with $\epsilon < 3$ than dielectrics with higher *k* [19]. The latter usually contain polar functional groups randomly oriented near the active interface, which is believed to increase the energetic disorder at the interface beyond what naturally occurs due to the structural disorder in the organic semiconductor film resulting in a lowering of the field-effect

mobility (Figure 2.3.3a). Low- k dielectrics also have the advantage of being less susceptible to ionic impurities, which can drift under the influence of the gate field, causing device instabilities (see Section 2.3.4).

A range of techniques have been developed that allow fabrication of OFET source-drain electrodes with submicrometer channel length (see, for example, Hamadani and Natelson [76] and Sele et al. [77]). To ensure correct scaling of the device characteristics in such short channel devices, the dielectric thickness needs to be significantly thinner than the channel length. Ideally, the gate dielectric thickness should be one order of magnitude smaller than the channel length. In this way, saturation of the FET current when the gate voltage (corrected for the threshold voltage) exceeds the source-drain voltage can be achieved even for submicrometer channel lengths.

Very thin, sub-20 nm organic dielectrics have been demonstrated using several approaches, such as self-assembled monolayer dielectrics [78], self-assembled molecular multilayers [79], or ultrathin polymer dielectrics [20]. Cross-linking of polyvinylphenol and polystyrene using bis(trichlorosilyl)alkyl reagents has been shown to result in improved dielectric properties and enable very thin spin-coatable polymer dielectrics [79]. Cho et al. have used self-assembled monolayers of dicosyltrichlorosilane as the gate dielectric of a bottom-gate, top-contact P3HT FET with inkjet-printed conducting polymer source-drain electrodes [80].

The chemical purity and composition of the gate dielectric can have dramatic effects on interfacial charge transport. The reason for the absence of n -type field-effect conduction in “normal” polymers such as PPVs or P3HT with electron affinities around 2.5–3.5 eV has puzzled the community for some time because, in LED devices, many of these polymers support electron conduction. Chua et al. [56] have demonstrated that by using appropriate gate dielectrics free of electron-trapping groups, such as hydroxyl, silanol, or carbonyl groups, n -channel FET conduction is in fact a generic property of most conjugated polymers. In contact with trapping-free dielectrics such as BCB or polyethylene, electron and hole mobilities were found to be of comparable magnitude in a broad range of polymers. Some polymers, such as P3HT and OC₁C₁₀-PPV, even exhibit ambipolar charge transport in suitable device configurations (Figure 2.3.5). This demonstrates clean inversion behavior in organic semiconductors with band gaps > 2 eV. n -Type behavior has previously been so elusive because most studies were performed on SiO₂ gate dielectrics for which electrochemical trapping of electrons by silanol groups at the interface occurs [56].

Light-emitting organic field-effect transistors (LEOFETs) have recently attracted much attention because they combine the switching characteristics of transistors with the light emission of diodes. Although several groups had reported light-emission from an OFET [81–85], no report of spatially resolved light emission from within the channel of an organic light-emitting FET had been made until recently. As a corollary to the realization of clean ambipolar transport in organic semiconductors at trap-free gate dielectric interfaces, light-emitting polymer field effect transistors with a well-defined recombination zone within the channel have recently been demonstrated [86,87]. Figure 2.3.6(a) shows a schematic diagram of an ambipolar OFET with a semiconducting layer of OC₁C₁₀-PPV in contact with BCB gate

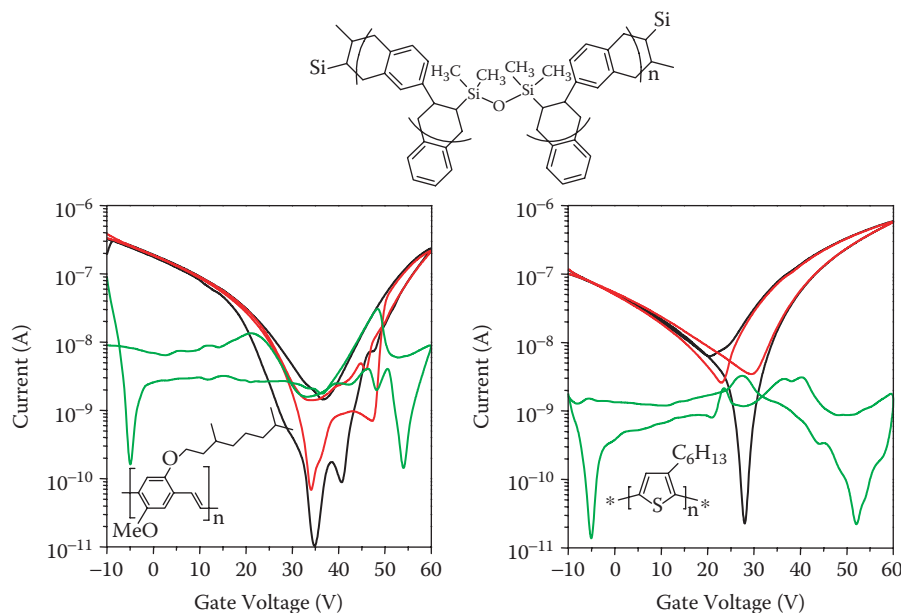


FIGURE 2.3.5 Transfer characteristics of bottom-gate OC₁C₁₀ PPV and P3HT FET with trap-free BCB gate dielectric exhibiting clean ambipolar transport ($V_{sd} = 60\text{V}$). (Courtesy of Jana Zaumseil, University of Cambridge.)

dielectric and two dissimilar source and drain contacts (Au and Ca) formed by an angled evaporation technique.

When such an ambipolar FET is biased with the gate voltage in between the source and the drain voltage, an electron accumulation layer is formed near one electrode coexisting with a hole accumulation layer near the other electrode. Electrons and holes can be observed to recombine where the two accumulation layers meet, leading to light emission from a well-defined zone, the position of which can be moved to any position along the channel by varying the applied voltages (Figure 2.3.6b). Since the semiconducting layer is unpatterned, light-emission can also be observed from the periphery of the device at distances of more than 500 μm from the edge of the electrodes (Figure 2.3.6c). The observation of a spatially resolved recombination in the channel provides an unambiguous proof of the coexisting electron and hole channels and the truly ambipolar nature of charge transport at such trap-free dielectric–organic semiconductor interfaces [86].

2.3.5 CHARGE TRANSPORT PHYSICS

The electronic structure of conjugated polymer semiconductors reflects the complex interplay between intrinsic π -electron delocalization along the polymer backbone and strong electron–phonon coupling, and the existence of energetic and positional disorder in solution-processed thin films. In a hypothetical, infinitely straight polymer chain, the highest occupied molecular orbital (HOMO) and lowest unoccupied

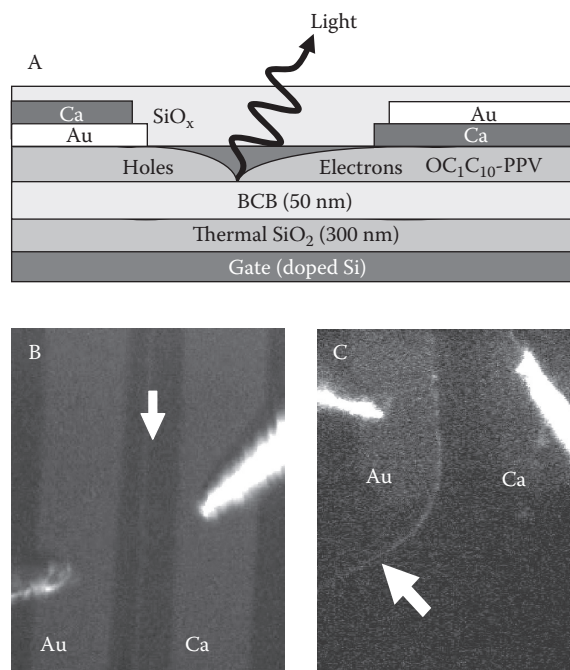


FIGURE 2.3.6 (A) Schematic diagram of bottom-gate, ambipolar light-emitting FET with an active semiconducting layer of OC₁C₁₀-PPV and BCB gate dielectric. (B) Photograph of light emission from within the channel of the FET ($I_{\text{FET}} = 30 \text{ nA}$, $V_g = -75\text{V}$). (C) Photograph of light emission from periphery of the device illustrating the spreading of both electron and hole accumulation layers into the unpatterned semiconductor region around the source-drain electrodes. The channel length is $80 \mu\text{m}$. (From Zaumseil, J. et al., *Nat. Mater.*, 5, 69–74, 2006. Reprinted with permission. Copyright 2006, Nature Publishing Group.)

molecular orbital (LUMO) states of the neutral polymer are fully delocalized along the polymer chain and, in fact, exhibit significant dispersion with calculated bandwidths of several electron volts [88]. However, as a result of the strong electron–phonon coupling and the disorder-induced finite conjugation length, charges introduced onto the polymer interact strongly with certain molecular vibrations and are able to lower their energy with respect to the extended HOMO/LUMO states by forming localized polaron states surrounded by a region of molecular distortion [89].

There is clear, experimental evidence that the charge carriers carrying the current in a conjugated polymer FET are indeed of polaronic nature. Due to the surrounding molecular distortion and electronic relaxation, the charged molecule exhibits characteristic optical transitions below the absorption edge of the neutral molecule. These can be observed in operational FETs using charge modulation spectroscopy (CMS), which detects changes of the optical transmission of a semitransparent FET device upon gate voltage induced modulation of the carrier concentration in the accumulation layer [90].

In polymers such as poly(di-octyl-fluorene-co-bithiophene) (F8T2) in which close interchain interactions are weakened by the sp^3 -coordinated carbon atom on

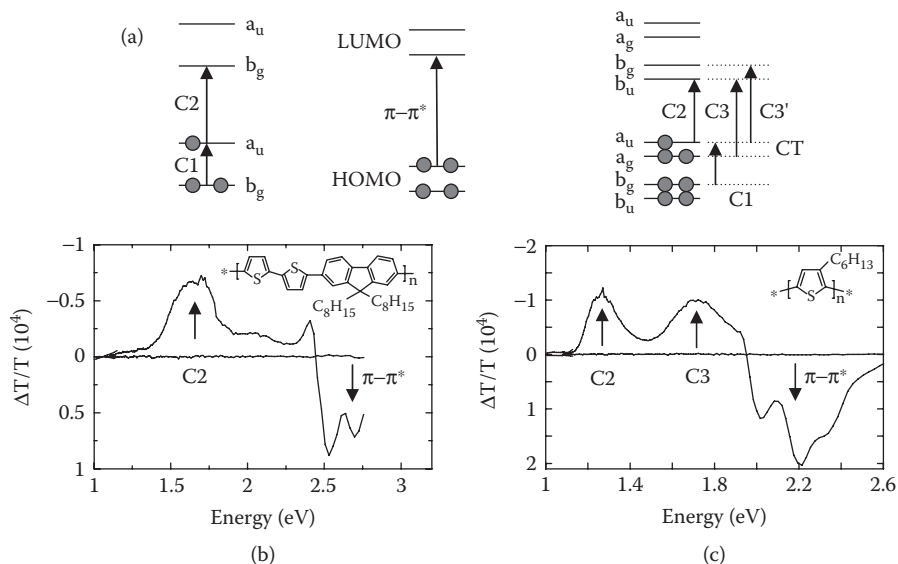


FIGURE 2.3.7 (a) Schematic energy diagram of neutral polymer (center), polaronic absorptions in the case of isolated chains (left) and interacting chains (right); charge modulation spectra of F8T2/PMMA (b) and P3HT/PMMA (c) top-gate FETs. (Courtesy of Shlomy Goffri, University of Cambridge.)

the fluorene unit, two characteristic sub-bandgap polaronic absorptions (Figure 2.3.7b) can be accounted for by the dipole-allowed C1 (≈ 0.4 eV) and visible C2 (1.6 eV) transitions of a simple isolated chain model (Figure 2.3.7a) [91]. In contrast, the charge-induced absorption spectrum of P3HT (Figure 2.3.7c) can only be explained by taking into account interchain interactions [92]. In addition to the C1 (0.3 eV) and C2 (1.3 eV) transitions, the CMS spectrum of high-mobility P3HT exhibits an additional C3 transition (1.6–1.8 eV), which is dipole forbidden in the isolated chain case, and low-energy charge transfer (CT) transitions at 60–120 meV [15,93]. Polarons in P3HT are not confined to a single chain, but are spread over several π -stacked chains. As a result of their two-dimensional nature, the polaron binding energy in P3HT is much reduced. From the position of the CT transition [89], the polaron binding energy E_p can be estimated to be on the order of

$$E_p \approx \frac{E_{CT}}{2} \approx 30\text{--}60 \text{ meV}.$$

At sufficiently high temperatures, charge transport of polaronic carriers in conjugated polymers should be governed by the physics of electron transfer processes, which was established by Marcus for chemical reactions and biological electron transfer processes [94]. In order for the localized polaron to hop between neighboring sites, the molecular configuration of the initial (occupied) site and the final (empty) site need to be distorted to a common configuration, where the molecular distortion

of both sites is equal (Figure 2.3.10a). This leads to thermally activated transport even in the absence of disorder. In the nonadiabatic limit, where the time scale for electron hopping is longer than that of the lattice vibrations, the mobility is given by:

$$\mu = \frac{e \cdot a^2}{k \cdot T} \cdot \nu \cdot \exp\left(-\frac{E_p}{2 \cdot k \cdot T}\right) \quad (2.3.1)$$

ν is the attempt frequency

$$\nu = \frac{\sqrt{\pi} \cdot J^2}{\sqrt{2 \cdot E_p \cdot kT}}$$

and a is the typical hopping distance.

However, in most experimental systems, the manifestations of the polaronic character of the charge carriers are masked by the effects of disorder. In any solution-deposited thin film, disorder is present and causes the energy of a polaronic charge carrier on a particular site to vary across the polymer network. Variations of the local conformation of the polymer backbone, presence of chemical impurities or structural defects of the polymer backbone, or dipolar disorder due to random orientation of polar groups of the polymer semiconductor or the gate dielectric result in a significant broadening of the electronic density of states.

The transport of charges injected into a molecular solid dominated by the effects of disorder is well understood from the work on molecularly doped polymers and other organic photoconductors used in xerography. Assuming a disorder-broadened Gaussian density of transport states with a characteristic width σ , Bässler [95] has shown on the basis of Monte Carlo simulations that an injected carrier hopping through such an otherwise empty density of states (DOS) relaxes to a dynamic equilibrium energy

$$\langle \epsilon_\infty \rangle = -\frac{\sigma^2}{kT}$$

below the center of the DOS, leading to a characteristic

$$\log \mu \propto \frac{1}{T^2}$$

temperature dependence of the mobility (Figure 2.3.8b).

The model has been improved by Novikov et al. [96], who showed that the dominant source of diagonal disorder is due to charge–dipole interactions and that spatial correlations of such interactions need to be taken into account in order to explain the commonly observed Poole–Frenkel dependence of the mobility on the electrical field. These researchers derived an expression for the electric field (E) and

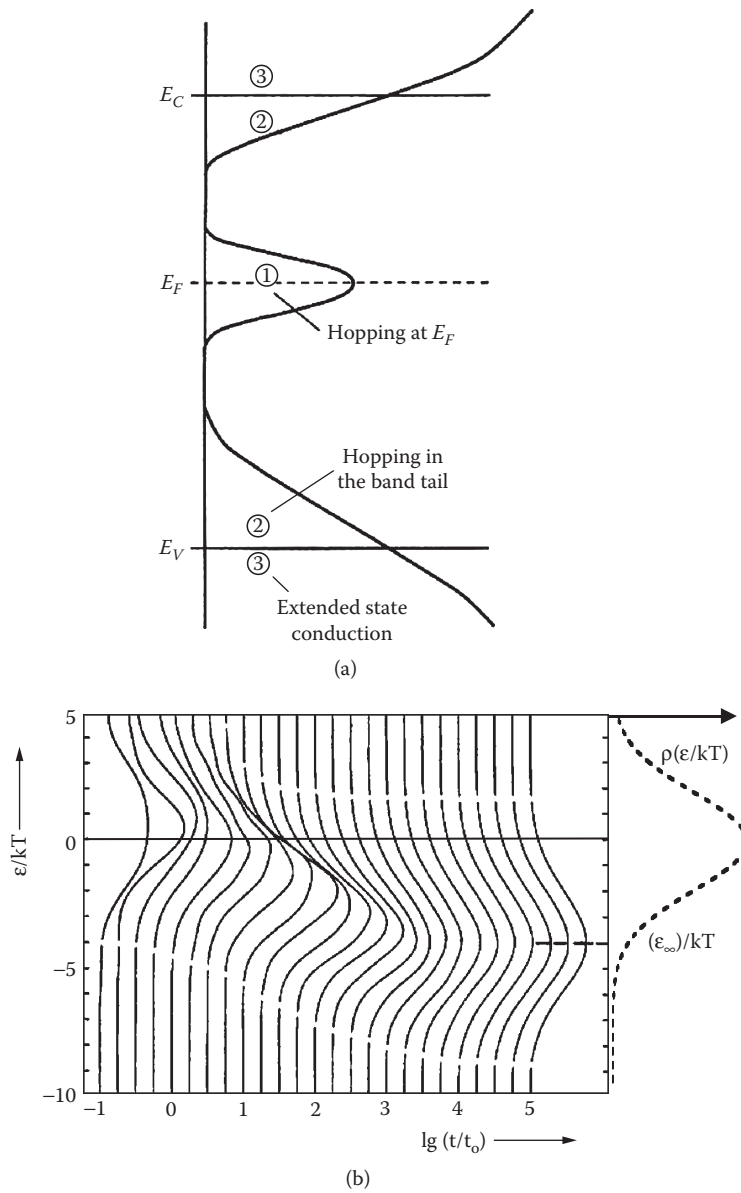


FIGURE 2.3.8 (a) Schematic energy diagram of DOS of a disordered semiconductor with a mobility edge. (b) Relaxation of energy distribution of an injected charge carrier hopping in a Gaussian DOS as a function of time. The DOS is shown as a dashed line on the right. (From Bäessler, H., *Phys. Status Solidi B*, 175, 15, 1993. Reprinted with permission. Copyright 1993, Wiley.)

temperature dependence of the mobility in a correlated DOS with diagonal as well as nondiagonal positional disorder:

$$\mu = \mu_0 \cdot \exp \left[- \left(\frac{3\sigma}{5 \cdot k_B \cdot T} \right)^2 + 0.78 \cdot \left(\left(\frac{\sigma}{k_B \cdot T} \right)^{3/2} - 2 \right) \sqrt{\frac{e \cdot a \cdot E}{\sigma}} \right] \quad (2.3.2)$$

The model describes the transport of individual injected carriers at zero/small carrier concentrations (i.e., in principle, it should not be directly applicable to the relatively high carrier concentrations $p = 10^{18}$ – 10^{19} cm⁻³ present in the accumulation layer of FETs). Vissenberg [97] has developed a percolation model for variable range hopping transport in the accumulation layer of an FET assuming an exponential DOS with width T_0 . An expression for the field-effect mobility as a function of carrier concentration p was derived:

$$\mu_{FE} = \frac{\sigma_0}{e} \left[\frac{\left(\frac{T_0}{T} \right)^4 \sin \left(\pi \frac{T}{T_0} \right)}{(2 \cdot \alpha)^3 \cdot B_c} \right]^{T_0/T} p^{\frac{T_0}{T} - 1}, \quad (2.3.3)$$

where σ_0 is the prefactor for the conductivity, α is the effective overlap parameter between localized states, and $B_c \cong 2.8$ is the critical number for onset of percolation. Transport in this model can be effectively described as activation from a gate voltage-dependent Fermi energy to a specific transport energy in the DOS.

Tanase et al. [98] have shown that in a series of isotropic, amorphous PPV polymers the large difference between the low mobility values extracted from space-charge limited current measurements in LEDs and the comparatively higher field-effect mobilities can be explained by the largely different charge carrier concentrations (Figure 2.3.9). It was possible to fit the temperature dependence of the zero-field LED mobility to Equation 2.3.2 and the carrier concentration dependence of the FET mobility to Equation 2.3.3 with a consistent value of $\sigma = 93$ – 125 meV. Building on this work, Pasveer et al. showed that at room temperature the current-voltage characteristics are dominated by the carrier concentration dependence of the mobility, while at low temperatures and high fields the field dependence of the mobility also needs to be considered [99]. The gate voltage dependence of the FET mobility of MEH-PPV has also been analyzed by Shaked et al. [100].

In several higher mobility amorphous hole transporting materials such as PTAA [18] and TFB [20], as well as in nematic, glassy polyfluorene-co-bithiophene [16], a somewhat different behavior was observed. The field-effect mobility was found to be independent of gate voltage within the carrier concentration range of 10^{18} – 10^{19} cm⁻³. In PTAA the low-density time-of-flight and high-density field-effect mobilities are of similar magnitude, with the bulk TOF mobility even higher by a factor of two to three at room temperature than the field-effect mobility. The Gaussian disorder

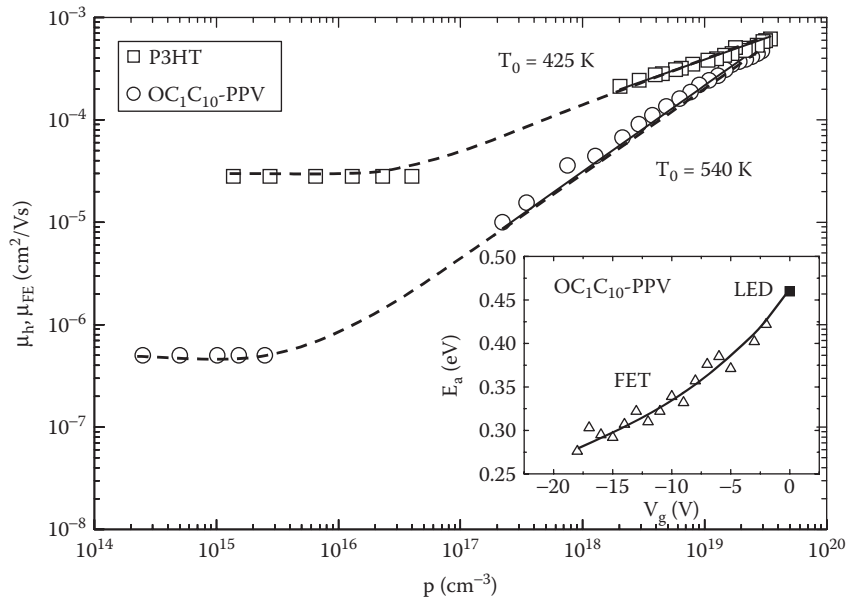


FIGURE 2.3.9 Hole mobility as a function of charge carrier concentration in diode and field-effect transistors for P3HT and a PPV derivative. (From Tanase, C. et al., *Phys. Rev. Lett.*, 91, 216601, 2003. Reprinted with permission. Copyright 2003, American Physical Society.)

model was used to extract significantly smaller values of $\sigma = 57$ meV and $\sigma = 68$ – 90 meV from the temperature dependence of the time-of-flight and field-effect mobility of amorphous PTAA, respectively (Figure 2.3.3b). The increased σ -value in the case of the FET mobility was attributed to the contribution to energetic disorder from polar disorder in the dielectric close to the charge-transporting accumulation layer.

The reason for the different behavior observed in PPVs with room-temperature field-effect mobility $< 10^{-3}$ – 10^{-4} cm²/Vs and the higher mobility PTAA and polyfluorene polymers ($\mu_{\text{FET}} = 10^{-3}$ – 10^{-2} cm²/Vs) might be related to the lower degree of energetic disorder in the latter. With narrow DOS ($\sigma < 60$ – 90 meV), the expected concentration dependence of the room-temperature mobility over a concentration range of 10^{14} – 10^{19} cm⁻³ spanned by LED/FET measurements is relatively weak (i.e., less than an order of magnitude) and might be masked by other effects such as differences in bulk and interface microstructure, effects of interface roughness, or disorder effects induced by polar or charged groups in the dielectric.

An alternative theoretical framework for understanding the effects of disorder is the multiple trapping model, which is well established for describing transport in amorphous silicon and has been claimed to be more appropriate for describing the charge transport in microcrystalline polymers such as P3HT [22] and poly(bis(alkylthienyl)-bithiophene) [101,102]. This model assumes that disorder broadening is sufficiently weak that, in a certain energy range, the DOS becomes high enough that electronic states above the so-called mobility edge are extended, while electronic states below the mobility edge remain localized (Figure 2.3.8a). The current is

assumed to be transported by carriers thermally activated into the delocalized states above the mobility edge, while carriers in localized states are effectively trapped and do not contribute to the current.

Assuming a specific DOS and a mobility for carriers above the mobility edge, the FET current can be obtained by first determining the position of the quasi-Fermi level at the interface for a particular gate voltage and then calculating the number of free carriers thermally excited above the mobility edge using Fermi–Dirac statistics. Salleo et al. [101] found that the multiple trapping model explained the temperature dependence of the FET mobility of poly(bis(alkyl-thienyl-bithiophene)) more consistently than the Vissenberg hopping model; the latter yielded an unphysical dependence of σ_0 and T_0 on the processing conditions.

In spite of detailed investigations to model the charge transport in a mobility regime between 10^{-2} and $1 \text{ cm}^2/\text{Vs}$, it can be difficult to distinguish between hopping and band transport models. Many of the qualitative features are common to both hopping and multiple trapping and release models, such as the mobility decreasing with decreasing temperature and the dependence of the mobility on the carrier concentration. Therefore, characterization of the charge transport by techniques that provide complementary information is needed.

One of the techniques providing such information is CMS. The spectroscopic properties of polarons in P3HT have been characterized as a function of molecular weight and film deposition conditions by CMS [32]. CMS experiments on regioregular P3HT have revealed a pronounced low-energy charge transfer (CT) transition in the midinfrared spectral region [15]. This transition can be interpreted in the framework of Marcus–Hush electron transfer theory describing the transfer of electrons between neighboring molecules in the presence of strong electron–lattice interactions [103]. The process is governed by two main parameters: The relaxation energy λ (which is twice the polaron binding energy) measures the energy lowering that charged molecules can achieve by adopting a relaxed conformation as a result of the electron–lattice coupling. The transfer integral t is a measure of the strength of the interchain coupling of the electronic wave functions on neighboring molecules. In the weak coupling case ($\lambda > 2t$), the lower adiabatic potential surface has a number of minima, and the charge is localized on an individual molecule (Figure 2.3.10a). Under such conditions, a charge transfer optical transition is observed centered at an energy $\omega_{\text{CT}} = \lambda$.

In contrast, in the strong coupling case ($\lambda < 2t$), the lower adiabatic potential surface has only one minimum and the charge is delocalized over a certain number of neighboring molecules. In this case, an optical charge transfer transition can also be observed; it is not centered around λ , but rather around $\omega_{\text{CT}} = 2t$ (Figure 2.3.10b). In intermediate MW samples with mobilities $> 0.05 \text{ cm}^2/\text{Vs}$, we observe an intense CT transition centered around 0.1 eV (Figure 2.3.10c). In the highest mobility, highest MW samples, the transition is similarly intense and appears to peak at slightly lower energies below 0.08 eV, which is the low energy cutoff of our experimental setup. In contrast, in the low MW samples with mobilities less than $10^{-2} \text{ cm}^2/\text{Vs}$, a much less intense CT transition is observed, and the transition peaks at significantly higher energies on the order of 0.3 eV.

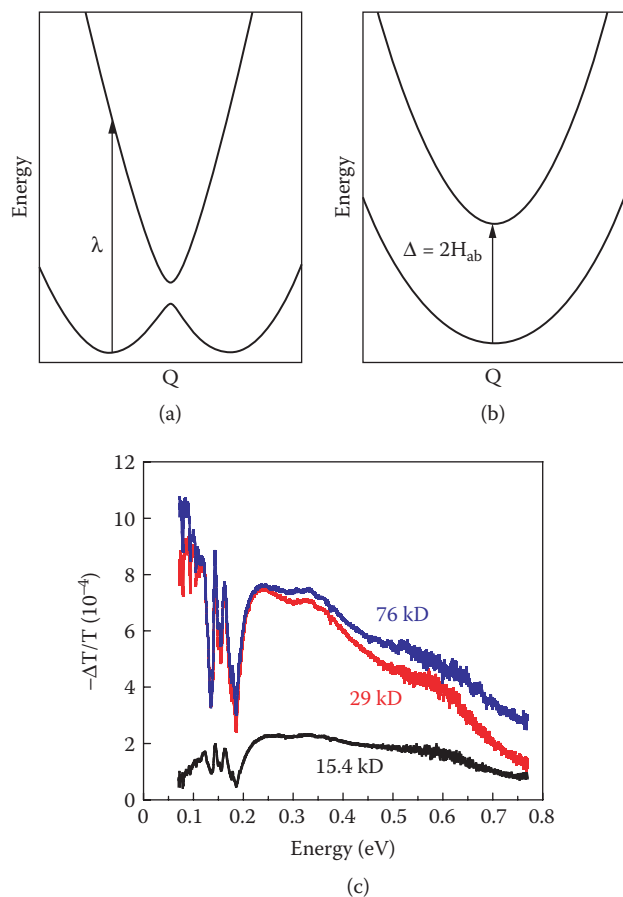


FIGURE 2.3.10 Potential energy diagram as a function of configuration coordinate illustrating electron transfer between two sites in the case of weak coupling (a) and strong coupling (b). (c) Charge modulation spectra in the midinfrared spectral range of TCB spin-cast P3HT films for different MW. The spectra were obtained by subtracting the infrared absorption spectra of the device structure taken at 10 and -30 V.

The position and intensity of the CT transition appears to be very directly correlated with the field-effect mobility. In high-mobility P3HT, the strong coupling situation applies [103]. The lower intensity of the CT transition indicates a lower degree of interchain polaron delocalization in the low MW samples. A plausible explanation for the reduced intensity and higher energy of the CT transition in the low MW samples is that, due to the enhanced disorder and shorter conjugation length in these samples, the weak coupling regime might apply. Such a crossover behavior between localized and delocalized polarons as a function of MW would provide an intriguing microscopic explanation for the observed rapid increase of mobility with MW below 15–20 kD (see Figure 2.3.4b) [32].

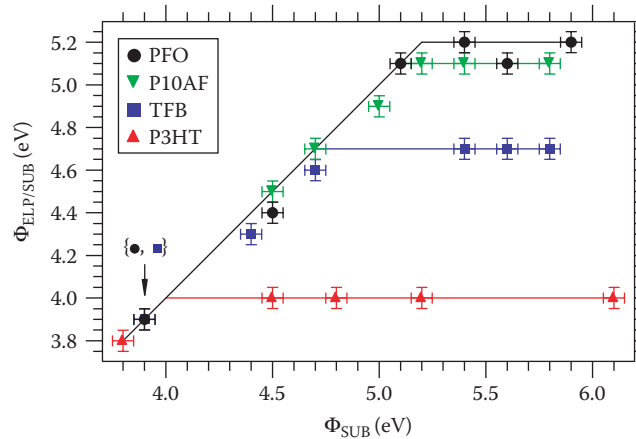


FIGURE 2.3.11 Dependence of work function of polymer coated substrate, $\Phi_{ELP/SUB}$, on the work function of bare substrate, Φ_{SUB} , for four studied materials: P3HT, TFB, poly(9-1-decylundecylidene fluorene) (P10AF), and polydioctylfluorene (PFO). (From Tengstedt, C. et al., *Appl. Phys. Lett.*, 88, 053502, 2006. Reprinted with permission. Copyright 2006, American Institute of Physics.)

2.3.6 CHARGE INJECTION PHYSICS

Another important aspect of the device physics, particularly in the context of short channel OFETs with $L < 5 \mu\text{m}$, is the injection of charges from a metal source-drain contact into the organic semiconductor. In contrast to inorganic semiconductors, controlled doping of organic semiconductors is still difficult, since dopants incorporated in the form of small molecule counter ions can migrate and cause device instabilities. Since most organic semiconductors that have shown useful FET performance have band gaps $> 2 \text{ eV}$, the formation of low-resistance ohmic contacts with common metals is often challenging.

The energy barrier for hole injection at the metal–polymer interface is determined by the vacuum work function of the metal contact Φ_w and the ionization potential I_p of the polymer. For conjugated polymer films spin-coated onto hole injecting metal electrodes, it has been reported that as long as Φ_w is smaller than a critical value characteristic of the polymer, no interface dipole is formed [104]. In this case, the barrier for hole injection can be estimated simply by aligning the vacuum levels of the metal and the polymer (Mott–Schottky limit); the measured work function of the metal with the polymer deposited on top increases linearly with Φ_w with a slope of one (see Figure 2.3.11).

However, when Φ_w exceeds said critical value a significant interface dipole can be formed. Positive charges are transferred from the metal to the semiconductor and the position of the Fermi level at the interface becomes pinned at an energy level interpreted as the hole polaron/bipolaron energy level in the polymer semiconductor. This simple picture suggests that, at least in the case of solution-deposited polymers on common hole-injecting contacts, chemical interactions between the metal and

the polymer and other defect states in the band gap of the polymer do not influence strongly the contact formation.

We emphasize that this is less likely to be the case for metals deposited on top of the polymer semiconductor as well as for reactive metals employed to achieve electron injection into common organic semiconductors. It has been shown that deposition of gold contacts on top of an organic semiconductor, such as pentacene, can result in formation of trap states in the organic semiconductor [105]. There are intriguing reports of efficient charge injection in systems for which Schottky barriers calculated using Mott–Schottky theory should exceed 1 eV, such as hole injection from Ca into P3HT [56] or electron injection from Au into fluorocarbon-substituted oligothiophenes [106]. It is likely that in such systems chemical interactions and interface states are important factors that determine contact formation.

In order to understand the contact injection in the OFET not only the interface electronic structure, but also the device configuration and injection geometry need to be taken into account because they determine the potential profile in the vicinity of the contact and the transport of injected charges away from the contacts. In the bottom gate device configuration, the charge injection physics can be studied directly using scanning Kelvin probe microscopy (SKPM) [107–109]. SKPM uses an atomic force microscope tip with a conducting coating operated in noncontact mode to probe the electrostatic potential profile along the channel of the OFET with a spatial resolution on the order of 100 nm (Figure 2.3.12a). The voltage applied to the conducting tip is regulated by a feedback loop so that the electrostatic force between tip and sample is minimized. For polymer TFTs in accumulation the tip potential essentially follows the electrostatic potential in the accumulation layer.

Figure 2.3.12(b) shows typical SKPM potential profiles obtained for bottom-gate, bottom contact P3HT devices on SiO₂ with Au contacts comprising a Cr adhesion layer (Cr–Au) (inset) and pure Cr contacts. It can be seen that the contact resistance at the source and drain contacts exhibits very different behavior in the two cases. In the case of Cr–Au contacts, generally, in the case of contacts for which the Schottky barrier Φ_b is less than 0.3 eV, the voltage drop across the source and drain contacts is small and the contact resistance at the source contact is very similar to that of the drain contact. This is somewhat unexpected since in normal FET operation the source contact is reverse biased while the drain contact is forward biased, implying that the source contact resistance should be significantly larger than the drain contact resistance.

This implies that under conditions that might be typical for high-performance OFETs, the contact resistance is not determined by the Schottky barrier at the interface, but by bulk transport processes in the semiconductor in the vicinity of the contact. Consistent with this interpretation, the contact resistance was found to depend on temperature in the same way as the mobility [107] so that the potential profiles become independent of temperature. This result was explained by invoking the existence of a depletion layer in the vicinity of the contacts. Similar results have been reported using channel length scaling analysis [76].

In contrast in the case of Cr contacts or generally for systems with Schottky barriers exceeding 0.3 eV, the voltage drops across the contacts become very significant and the source resistance is found to be larger than the drain resistance, as

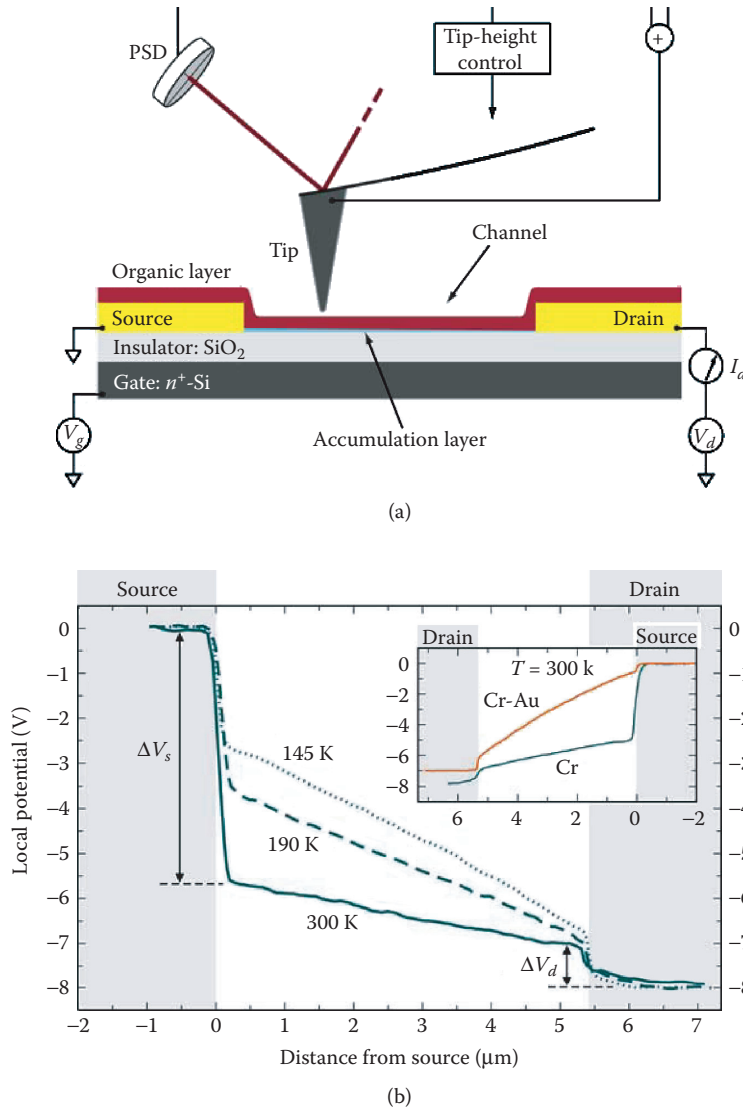


FIGURE 2.3.12 (a) Schematic diagram of experimental setup for scanning Kelvin probe microscopy (SKPM). (b) Profiles of an $L = 5.5 \mu\text{m}$ P3HT transistor with Cr electrodes taken at three different temperatures ($V_g = -40 \text{ V}$, $V_d = -8 \text{ V}$). The inset shows a profile obtained after switching the source and drain contacts on the same TFT with both Cr and Cr-Au contacts $V_g = -40 \text{ V}$, $V_d = -8 \text{ V}$. (From Burgi, L. et al., *J. Appl. Phys.*, 94, 6129–6137, 2003. Reprinted with permission. Copyright 2003, American Institute of Physics.)

expected (see Figure 2.3.11b). This implies that in this regime the contact resistance is determined by the injection physics at the interface [107]. It is remarkable that, in spite of the significant expected Schottky barrier height, the contact resistance shows only a very weak increase with decreasing temperature, which is even weaker than that of the field-effect mobility (i.e., the voltage drop at the contacts decreases compared to that across the bulk of the polymer with decreasing temperature and charge transport becomes less contact limited at low temperatures).

This behavior cannot be explained in the framework of the commonly used diffusion-limited thermionic emission model [110], which takes into account back-scattering into the metal due to the small mean-free path in the organic semiconductor and predicts the activation energy of the contact resistance to be larger than that of the mobility and larger than Φ_p/kT .

Explanation of the experimental data required taking into account disorder-induced broadening of the density of states of the organic semiconductor, which provides carriers with injection pathways through deep states in the DOS, leading to a reduced effective barrier at low temperatures. Similar conclusions have recently been drawn on the basis of channel length scaling experiments [111].

2.3.7 DEFECT STATES AND DEVICE DEGRADATION MECHANISMS

Electronic defect states in the semiconductor at the interface between semiconductor and dielectric and inside the dielectric layer can cause instabilities of the threshold voltage of the TFT. For practical applications, the threshold voltage stability is a figure of merit as important as, if not more important than, the field-effect mobility because it is closely related to the operational and shelf lifetime of the device. Most TFT technologies, including those based on a-Si, suffer from threshold voltage shifts induced by bias-temperature stress (BTS). In a-Si TFTs, generation of defect states inside the semiconducting layer, such as dangling bond defects, as well as charge injection into the SiN_x gate dielectric has been found to contribute to V_T shifts upon BTS; charge injection into the dielectric is the dominant mechanism in high-quality material [112]. Several groups have recently reported systematic BTS investigations and studies of organic TFT characteristics upon exposure to atmospheric conditions and humidity.

In most *p*-type organic semiconductors, a negative shift of the threshold voltage is observed upon prolonged operation of the device in accumulation, which is generally attributed to charge trapping in the organic semiconductor and/or at the active interface. Matters et al. reported negative V_T shifts due to charge trapping for a PTV precursor polymer in contact with inorganic SiO_2 dielectric; these were more pronounced in the presence of water than when the device was operated in vacuum or dry air [113]. Street et al. reported significant negative V_T shifts in F8T2/ SiO_2 bottom-gate, bottom-contact TFTs [114], which were more pronounced than reported for top-gate F8T2 devices with a polymer dielectric [16]. Street et al. also found the V_T stability of PQT/ SiO_2 devices to be significantly better than that of F8T2/ SiO_2

devices. It is clear from these experiments whether the device configuration, choice of contacts, and dielectric play a crucial role in determining the device stability.

There is little known at present about the nature of the electronic states involved in defect formation and device degradation. Few experimental studies have been aimed at understanding at a microscopic level the nature of defect states in organic semiconductors [115]. Device modeling has been used to understand the subthreshold characteristics of OFETs [116]. Based on an analysis of the relationship between the current decay at early times after FET turn-on and the hole concentration in the channel, Street et al. have suggested that charge trapping occurs due to formation of low-mobility bipolarons by reaction of two polarons [114,117]. However, Deng et al. performed optical spectroscopy of field-induced charge on F8T2/PMMA TFTs exhibiting significant V_T shifts, but were unable to detect the spectroscopic signature of bipolarons [91].

When discussing threshold voltage shifts in OFETs, it is important to distinguish between reversible and irreversible charge trapping effects [118]. Reversible charge trapping depends on the duty cycle during operation and can be recovered by not operating the device for several minutes or hours. Threshold voltage shifts due to irreversible charge trapping are independent of duty cycle and do not recover on timescales of hours if the device is not operated while being kept in the dark. However, the irreversible threshold shift can be erased by illuminating the sample with above-bandgap light [119,120] (Figure 2.3.13a).

The spectral dependence of the light-induced recovery follows the absorption spectrum of the organic semiconductor (Figure 2.3.13b). Charge traps that can be emptied in this way must be located inside the organic semiconductor or directly at the interface, but cannot be located inside the gate dielectric. It has also been reported that a positive gate voltage stress leads to a shift of V_T to more positive values [119]. This has recently been explained by injection and trapping of negative electrons at the interface [56].

Zilker et al. have reported that, in films of *p*-type solution-processed pentacene in contact with an organic photoresist dielectric, the threshold voltage shifts to more positive values for negative gate bias stress during operation in air [121]. The V_T shift was the more pronounced the smaller the source-drain voltage was. This was interpreted as the result of mobile ions drifting in the gate dielectric in the presence of water. Negative ions drifting towards the active interface cause accumulation of positive countercharges in the semiconducting layer. Only during operation in vacuum or in dry air was a negative V_T shift of -3 V after application of $V_g = -20$ V for 1000 s observed resulting from charge trapping at or near the interface. Rep et al. have investigated the role of ionic impurities originating from the substrate on the conductivity of P3HT films [122]. On Na_2O containing glass substrates, Na^+ ions were found to drift towards the negatively biased contact, leaving behind negative charge centers on the glass surface. Gomes et al. have claimed recently that the bias stress instability in organic FETs is caused by trapped water in the organic semiconductor [123].

The preceding results point to the crucial role of the gate dielectric in determining the operational and shelf stability of the device. Several groups have recently reported very encouraging BTS and shelf lifetime data for solution-processed

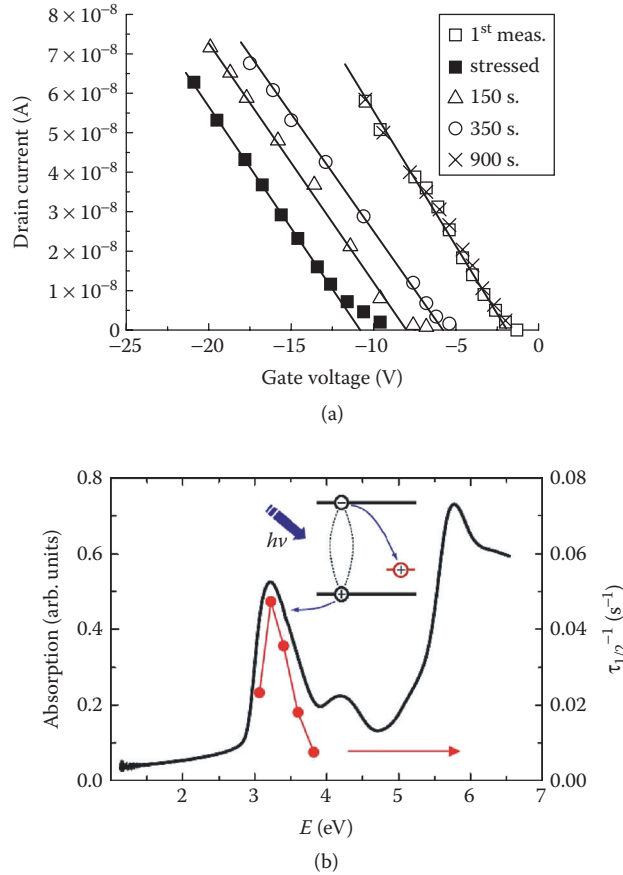


FIGURE 2.3.13 (a) Pulsed transfer characteristics of bottom-gate F8T2/SiO₂ FET after applying a negative gate bias stress showing subsequent recovery of the threshold voltage shift after illuminating the device for different periods of time. (From Salleo, A. and Street, R.A., *J. Appl. Phys.*, 94, 4231–4231, 2003. Reprinted with permission. Copyright 2003, American Physical Society.) (b) Comparison of the wavelength dependence of the time constant for the light-induced trap release in TFB/SiO₂ with the absorption spectrum of the organic semiconductor. (From Burgi, L. et al., *Syn. Met.*, 146, 297–309, 2004. Reprinted with permission. Copyright 2004, Elsevier.)

OFETs measured and stored in air without special encapsulation. PTAA combined with low- k dielectrics exhibits excellent shelf life with no discernible V_T shift upon storage in air and light for periods of several months [18]. Similarly, TFTs based on TFB with BCB dielectric exhibit very good operational stability during accelerated lifetime testing at temperatures of 120°C [20]. In both cases, the good stability is believed to be related to the use of an apolar, low- k dielectric, which is less susceptible to ionic impurities, and the amorphous microstructure of the aryl-amine-based polymer semiconductor with good thermal and photostability and low degree of energetic disorder.

The group at Plastic Logic has recently reported excellent operational stability results on unencapsulated polymer TFTs fabricated on PET substrates [10]. Although, of course, significant work to assess and improve the operational and shelf life of OFETs under realistic application conditions and to understand degradation mechanisms in much more detail remains, these early results strongly suggest that solution-processed OFETs can exhibit device stability and reliability similar to if not higher than their a-Si counterparts.

2.3.8 OUTLOOK

Solution-processable organic FETs have become a promising emerging technology for low-cost, large-area electronics on flexible plastic substrates. FET performance is approaching that of a-Si TFTs, and solution/printing-based manufacturing processes have been developed. Device operational and environmental stability has improved significantly recently as a result of availability of organic semiconductors with higher inherent oxidative stability, better understanding of the requirements for gate dielectrics, and more controlled manufacturing processes.

In this chapter, we have reviewed recent progress in understanding the device physics of solution-processable organic semiconductors. It should be apparent from the discussion that although much progress has been made in understanding the materials physics and requirements for high-performance FETs, understanding of the fundamental excitations and processes at a microscopic level involved in charge transport and injection as well as device degradation is still much more superficial than the corresponding level of fundamental understanding available in inorganic semiconductors. Particularly, many fundamental aspects of the correlation between the structure and physics of charge transport at solution-processed organic–organic heterointerfaces remain to be explored.

However, the field of organic electronics is gaining momentum. Continued breakthroughs in materials and device performance, concrete industrial applications in active matrix flexible electronic paper displays, and simple, low-cost intelligent labels are emerging on the horizon to be commercialized within the next three to five years. It is likely that new scientific discoveries and technological advances will continue to cross-fertilize each other for the foreseeable future.

REFERENCES

1. Burroughes, J.H., Bradley, D.D.C., Brown, A.R., Marks, R.N., Mackay, K., Friend, R.H., Burn, P.L. and Holmes, A.B., Light-emitting diodes based on conjugated polymers, *Nature*, 347, 539–541, 1990.
2. Yu, G., Gao, J., Hummelen, J.C., Wudl, F. and Heeger, A.J., Polymer photovoltaic cells: enhanced efficiencies via a network of internal donor-acceptor heterojunctions, *Science*, 270, 1789–1791, 1995.
3. Burroughes, J.H., Jones, C.A. and Friend, R.H., New semiconductor device physics in polymer diodes and transistors, *Nature*, 335, 137–141, 1988.

4. Heilmeyer, G.H. and Zanoni, L.A., Surface studies of alpha-copper phthalocyanine films, *J. Phys. Chem. Solids*, 25, 603, 1964.
5. Horowitz, G., Peng, X.Z., Fichou, D. and Garnier, F., A field-effect transistor based on conjugated alpha-sexithyrynyl, *Sol. St. Commun.*, 72, 381–384, 1989.
6. Ebisawa, E., Kurokawa, T. and Nara, S., Electrical properties of polyacetylene/polysiloxane interface, *J. Appl. Phys.*, 54, 3255, 1983.
7. Koezuka, H., Tsumara, A. and Ando, T., Field-effect transistor with polythiophene thin film, *Synth. Met.*, 18, 699–704, 1987.
8. Baude, P.F., Ender, D.A., Haase, M.A., Kelley, T.W., Muires, D.V. and Theiss, S.D., Pentacene-based radio-frequency identification circuitry, *Appl. Phys. Lett.*, 82, 3964–3966, 2003.
9. McCulloch, I., Heeney, M., Bailey, C., Genevicius, K., Macdonald, I., Shkunov, M., Sparrowe, D., Tierney, S., Wagner, R., Zhang, W., Chabinyc, M.L., Kline, R.J., McGehee, M.D. and Toney, M.F., Liquid-crystalline semiconducting polymers with high charge-carrier mobility, *Nat. Mater.*, Advance online publication, 2006.
10. Reynolds, K., Burns, S., Banach, M., Brown, T., Chalmers, K., Cousins, N., Creswell, L., Etechells, M., Hayton, C., Jacobs, K., Menon, A., Siddique, S., Ramsdale, C., Reeves, W., Watts, J., Werne, T.v., Mills, J., Curling, C., Sirringhaus, H., Amundson, K. and McCreary, M.D., Printing of polymer transistors for flexible active matrix displays, *Proc. Int. Display Workshop (IDW)*, 2004.
11. Sirringhaus, H., Sele, C.W., Ramsdale, C.R. and Werne, T.V., Manufacturing of organic transistor circuits by solution-based printing. In *Organic electronics*, ed. H. Klauk, Wiley–VCH, Weinheim, Germany, 2006.
12. Forrest, S.R., The path to ubiquitous and low-cost organic electronic appliances on plastic, *Nature*, 428, 911–918, 2004.
13. Gelinck, G.H., Huitema, H.E.A., Van Veenendaal, E., Cantatore, E., Schrijnemakers, L., Van der Putten, J., Geuns, T.C.T., Beenhakkers, M., Giesbers, J.B., Huisman, B.H., Meijer, E.J., Benito, E.M., Touwslager, F.J., Marsman, A.W., Van Rens, B.J.E. and De Leeuw, D.M., Flexible active-matrix displays and shift registers based on solution-processed organic transistors, *Nat. Mater.*, 3, 106–110, 2004.
14. Clemens, W., Fix, I., Ficker, J., Knobloch, A. and Ullmann, A., From polymer transistors toward printed electronics, *J. Mater. Res.*, 19, 1963–1973, 2004.
15. Sirringhaus, H., Brown, P.J., Friend, R.H., Nielsen, M.M., Bechgaard, K., Langeveld-Voss, B.M.W., Spiering, A.J.H., Janssen, R.A.J., Meijer, E.W., Herwig, P. and de Leeuw, D.M., Two-dimensional charge transport in self-organized, high-mobility conjugated polymers, *Nature*, 401, 685–688, 1999.
16. Sirringhaus, H., Wilson, R.J., Friend, R.H., Inbasekaran, M., Wu, W., Woo, E.P., Grell, M. and Bradley, D.D.C., Mobility enhancement in conjugated polymer field-effect transistors through chain alignment in a liquid-crystalline phase, *Appl. Phys. Lett.*, 77, 406–408, 2000.
17. Burroughes, J.H. and Friend, R.H., The semiconductor device physics of polyacetylene. In: *Conjugated polymers*, ed. J.L. Brédas and R. Silbey, Kluwer, Dordrecht, 1991, 555–622.
18. Veres, J., Ogier, S.D., Leeming, S.W., Cupertino, D.C. and Khaffaf, S.M., Low-k insulators as the choice of dielectrics in organic field-effect transistors, *Adv. Func. Mater.*, 13, 199–204, 2003.
19. Veres, J., Ogier, S., Lloyd, G. and de Leeuw, D., Gate insulators in organic field-effect transistors, *Chem. Mater.*, 16, 4543–4555, 2004.

20. Chua, L.L., Ho, P.K.H., Sirringhaus, H. and Friend, R.H., High-stability ultrathin spin-on benzocyclobutene gate dielectric for polymer field-effect transistors, *Appl. Phys. Lett.*, 84, 3400–3402, 2004.
21. Bao, Z., Dodabalapur, A. and Lovinger, A.J., Soluble and processable regioregular poly(3-hexylthiophene) for thin film field-effect transistor applications with high mobility, *Appl. Phys. Lett.*, 69, 4108–4110, 1996.
22. Sirringhaus, H., Tessler, N. and Friend, R.H., Integrated optoelectronic devices based on conjugated polymers, *Science*, 280, 1741–1744, 1998.
23. Bjornholm, T., Hassenkam, T., Greve, D.R., McCullough, R.D., Jayaraman, M., Savoy, S.M., Jones, C.E. and McDevitt, J.T., Polythiophene nanowires, *Adv. Mater.*, 11, 1218–1221, 1999.
24. Kline, R.J., McGehee, M.D., Kadnikova, E.N., Liu, J.S. and Frechet, J.M.J., Controlling the field-effect mobility of regioregular polythiophene by changing the molecular weight, *Adv. Mater.*, 15, 1519, 2003.
25. Merlo, J.A. and Frisbie, C.D., Field effect transport and trapping in regioregular polythiophene nanofibers, *J. Phys. Chem. B*, 108, 19169–19179, 2004.
26. Chang, J.F., Sun, B.Q., Breiby, D.W., Nielsen, M.M., Solling, T.I., Giles, M., McCulloch, I. and Sirringhaus, H., Enhanced mobility of poly(3-hexylthiophene) transistors by spin-coating from high-boiling-point solvents, *Chem. Mater.*, 16, 4772–4776, 2004.
27. Zhao, N., Botton, G.A., Zhu, S.P., Duft, A., Ong, B.S., Wu, Y.L. and Liu, P., Microscopic studies on liquid crystal poly(3,3''- dialkylquaterthiophene) semiconductor, *Macromolecules*, 37, 8307–8312, 2004.
28. Wang, G.M., Swensen, J., Moses, D. and Heeger, A.J., Increased mobility from regioregular poly(3-hexylthiophene) field-effect transistors, *J. Appl. Phys.*, 93, 6137–6141, 2003.
29. Kim, D.H., Park, Y.D., Jang, Y.S., Yang, H.C., Kim, Y.H., Han, J.I., Moon, D.G., Park, S.J., Chang, T.Y., Chang, C.W., Joo, M.K., Ryu, C.Y. and Cho, K.W., Enhancement of field-effect mobility due to surface-mediated molecular ordering in regioregular polythiophene thin film transistors, *Adv. Func. Mater.*, 15, 77–82, 2005.
30. Zen, A., Pflaum, J., Hirschmann, S., Zhuang, W., Jaiser, F., Asawapirom, U., Rabe, J.P., Scherf, U. and Neher, D., Effect of molecular weight and annealing of poly(3-hexylthiophene)s on the performance of organic field-effect transistors, *Adv. Func. Mater.*, 14, 757–764, 2004.
31. Zhang, R. et al., Nanostructure dependence of field-effect mobility in regioregular poly(3-hexylthiophene) thin film field effect transistors, *J. Am. Chem. Soc.*, advance online publication, 2006.
32. Chang, J.F., Clark, J., Zhao, N., Sirringhaus, H., Breiby, D.W., Andreasen, J.W., Nielsen, M.M., Giles, M., Heeney, M. and McCulloch, I., Molecular weight dependence of interchain polaron delocalization and exciton bandwidth in high-mobility conjugated polymers, 2006 (submitted).
33. Kline, R.J., McGehee, M.D. and Toney, M.F., Highly oriented crystals at the buried interface in polythiophene thin-film transistors, *Nat. Mater.*, 5, 222–228, 2006.
34. Sirringhaus, H., Tessler, N., Thomas, D.S., Brown, P.J. and Friend, R.H., High-mobility conjugated polymer field-effect transistors. In: *Advances in Solid State Physics*, Vol. 39, ed. B. Kramer Vieweg, Braunschweig, 1999, 101–110.
35. Abdou, M.S.A., Orfino, F.P., Son, Y. and Holdcroft, S., Interaction of oxygen with conjugated polymers: Charge transfer complex formation with poly(3-alkylthiophenes), *J. Am. Chem. Soc.*, 119, 4518–4524, 1997.

36. Ficker, J., Ullmann, A., Fix, W., Rost, H. and Clemens, W., Stability of polythiophene-based transistors and circuits, *J. Appl. Phys.*, 94, 2638–2641, 2003.
37. Ficker, J., von Seggern, H., Rost, H., Fix, W., Clemens, W. and McCulloch, I., Influence of intensive light exposure on polymer field-effect transistors, *Appl. Phys. Lett.*, 85, 1377–1379, 2004.
38. Ong, B.S., Wu, Y.L., Liu, P. and Gardner, S., High-performance semiconducting polythiophenes for organic thin-film transistors, *J. Am. Chem. Soc.*, 126, 3378–3379, 2004.
39. Heeney, M., Bailey, C., Genevicius, K., Shkunov, M., Sparrowe, D., Tierney, S. and McCulloch, I., Stable polythiophene semiconductors incorporating thieno 2,3-b thiophene, *J. Am. Chem. Soc.*, 127, 1078–1079, 2005.
40. Herwig, P.T. and Mullen, K., A soluble pentacene precursor: Synthesis, solid-state conversion into pentacene and application in a field-effect transistor, *Adv. Mater.*, 11, 480, 1999.
41. Afzali, A., Dimitrakopoulos, C.D. and Graham, T.O., Photosensitive pentacene precursor: Synthesis, photothermal patterning, and application in thin-film transistors, *Adv. Mater.*, 15, 2066, 2003.
42. Gelinck, G.H., Geuns, T.C.T. and de Leeuw, D.M., High-performance all-polymer integrated circuits, *Appl. Phys. Lett.*, 77, 1487–1489, 2000.
43. Afzali, A., Dimitrakopoulos, C.D. and Breen, T.L., High-performance, solution-processed organic thin film transistors from a novel pentacene precursor, *J. Am. Chem. Soc.*, 124, 8812–8813, 2002.
44. Minakata, T. and Natsume, Y., Direct formation of pentacene thin films by solution process, *Syn. Met.*, 153, 1–4, 2005.
45. Aramaki, S., Sakai, Y. and Ono, N., Solution-processable organic semiconductor for transistor applications: Tetrabenzoporphyrin, *Appl. Phys. Lett.*, 84, 2085–2087, 2004.
46. Chang, P.C., Lee, J., Huang, D., Subramanian, V., Murphy, A.R. and Frechet, J.M.J., Film morphology and thin film transistor performance of solution-processed oligothiophenes, *Chem. Mater.*, 16, 4783–4789, 2004.
47. Laquindanum, J.G., Katz, H.E. and Lovinger, A.J., Synthesis, morphology, and field-effect mobility of anthradithiophenes, *J. Am. Chem. Soc.*, 120, 664–672, 1998.
48. Katz, H.E., Recent advances in semiconductor performance and printing processes for organic transistor-based electronics, *Chem. Mater.*, 16, 4748–4756, 2004.
49. Mushrush, M., Facchetti, A., Lefenfeld, M., Katz, H.E. and Marks, T.J., Easily processable phenylene-thiophene-based organic field-effect transistors and solution-fabricated nonvolatile transistor memory elements, *J. Am. Chem. Soc.*, 125, 9414–9423, 2003.
50. Stingelin-Stutzmann, N., Smits, E., Wondergem, H., Tanase, C., Blom, P., Smith, P. and De Leeuw, D., Organic thin-film electronics from vitreous solution-processed rubrene hypereutectics, *Nat. Mater.*, 4, 601–606, 2005.
51. van de Craats, A.M., Stutzmann, N., Bunk, O., Nielsen, M.M., Watson, M., Mullen, K., Chanzy, H.D., Sirringhaus, H. and Friend, R.H., Meso-epitaxial solution-growth of self-organizing discotic liquid-crystalline semiconductors, *Adv. Mater.*, 15, 495–499, 2003.
52. Pisula, W., Menon, A., Stepputat, M., Lieberwirth, I., Kolb, U., Tracz, A., Sirringhaus, H., Pakula, T. and Müllen, K., A zone-casting technique for device fabrication of field-effect transistors based on discotic hexa-peri-hexabenzocoronene, *Adv. Mater.*, 17, 684–689, 2005.

53. Xiao, S.X., Myers, M., Miao, Q., Sanaur, S., Pang, K.L., Steigerwald, M.L. and Nuckolls, C., Molecular wires from contorted aromatic compounds, *Angew. Chem.-Inter. Ed.*, 44, 7390–7394, 2005.
54. McCulloch, I., Zhang, W.M., Heeney, M., Bailey, C., Giles, M., Graham, D., Shkunov, M., Sparrowe, D. and Tierney, S., Polymerizable liquid crystalline organic semiconductors and their fabrication in organic field effect transistors, *J. Am. Chem. Soc.*, 13, 2436–2444, 2003.
55. Dimitrakopoulos, C.D. and Malenfant, P.R.L., Organic thin film transistors for large area electronics, *Adv. Mater.*, 14, 99, 2002.
56. Chua, L.L., Zaumseil, J., Chang, J.F., Ou, E.C.W., Ho, P.K.H., Sirringhaus, H. and Friend, R.H., General observation of *n*-type field-effect behaviour in organic semiconductors, *Nature*, 434, 194–199, 2005.
57. Katz, H.E., Lovinger, A.J., Johnson, J., Kloc, C., Siegrist, T., Li, W., Lin, Y.-Y. and Dodabalapur, A., A soluble and air stable organic semiconductor with high electron mobility, *Nature*, 404, 478–481, 2000.
58. Babel, A. and Jenekhe, S.A., High electron mobility in ladder polymer field-effect transistors, *J. Am. Chem. Soc.*, 125, 13656–13657, 2003.
59. Facchetti, A., Musherush, M., Yoon, M.H., Hutchison, G.R., Ratner, M.A. and Marks, T.J., Building blocks for *n*-type molecular and polymeric electronics. Perfluoroalkyl versus alkyl-functionalized oligothiophenes (*nT*; *n* = 2–6). Systematics of thin film microstructure, semiconductor performance, and modeling of majority charge injection in field-effect transistors, *J. Am. Chem. Soc.*, 126, 13859–13874, 2004.
60. Waldauf, C., Schilinsky, P., Perisutti, M., Hauch, J. and Brabec, C.J., Solution-processed organic *n*-type thin-film transistors, *Adv. Mater.*, 15, 2084, 2003.
61. Anthopoulos, T.D., de Leeuw, D.M., Cantatore, E., van't Hof, P., Alma, J. and Hummelen, J.C., Solution processable organic transistors and circuits based on a C-70 methanofullerene, *J. Appl. Phys.*, 98, 2005.
62. Meijer, E.J., De Leeuw, D.M., Setayesh, S., Van Veenendaal, E., Huisman, B.H., Blom, P.W.M., Hummelen, J.C., Scherf, U. and Klapwijk, T.M., Solution-processed ambipolar organic field-effect transistors and inverters, *Nat. Mater.*, 2, 678–682, 2003.
63. Babel, A., Wind, J.D. and Jenekhe, S.A., Ambipolar charge transport in air-stable polymer blend thin-film transistors, *Adv. Func. Mater.*, 14, 891–898, 2004.
64. Shkunov, M., Simms, R., Heeney, M., Tierney, S. and McCulloch, I., Ambipolar field-effect transistors based on solution-processable blends of thieno 2,3-b thiophene terthiophene polymer and methanofullerenes, *Adv. Mater.*, 17, 2608, 2005.
65. Anthopoulos, T.D., de Leeuw, D.M., Cantatore, E., Setayesh, S., Meijer, E.J., Tanase, C., Hummelen, J.C. and Blom, P.W.M., Organic complementary-like inverters employing methanofullerene-based ambipolar field-effect transistors, *Appl. Phys. Lett.*, 85, 4205–4207, 2004.
66. Kunugi, Y., Takimiya, K., Negishi, N., Otsubo, T. and Aso, Y., An ambipolar organic field-effect transistor using oligothiophene incorporated with two 60 fullerenes, *J. Mater. Chem.*, 14, 2840–2841, 2004.
67. Facchetti, A., Yoon, M.H. and Marks, T.J., Gate dielectrics for organic field-effect transistors: New opportunities for organic electronics, *Adv. Mater.*, 17, 1705–1725, 2005.
68. Drury, C.J., Mutsaers, C.M.J., Hart, C.M., Matters, M. and de Leeuw, D.M., Low-cost all-polymer integrated circuits, *Appl. Phys. Lett.*, 73, 108–110, 1998.
69. Sirringhaus, H., Kawase, T., Friend, R.H., Shimoda, T., Inbasekaran, M., Wu, W. and Woo, E.P., High-resolution inkjet printing of all-polymer transistor circuits, *Science*, 290, 2123–2126, 2000.

70. R.A.L. Jones and Richards, R.W., *Polymers at surfaces and interfaces*, Cambridge University Press, Cambridge, 1999.
71. Chua, L.L., Ho, P.K.H., Sirringhaus, H. and Friend, R.H., Observation of field-effect transistor behavior at self-organized interfaces, *Adv. Mater.*, 16, 1609–1613, 2004.
72. Majewski, L.A., Grell, M., Ogier, S.D. and Veres, J., A novel gate insulator for flexible electronics, *Org. Elect.*, 4, 27–32, 2003.
73. Majewski, L.A., Schroeder, R. and Grell, M., One volt organic transistor, *Adv. Mater.*, 17, 192–196, 2005.
74. Chen, F.C., Chu, C.W., He, J., Yang, Y. and Lin, J.L., Organic thin-film transistors with nanocomposite dielectric gate insulator, *Appl. Phys. Lett.*, 85, 3295, 2004.
75. Sandberg, H.G.O., Backlund, T.G., Osterbacka, R. and Stubb, H., High-performance all-polymer transistor utilizing a hygroscopic insulator, *Adv. Mater.*, 16, 1112–1116, 2004.
76. Hamadani, B.H. and Natelson, D., Temperature-dependent contact resistances in high-quality polymer field-effect transistors, *Appl. Phys. Lett.*, 84, 443–445, 2004.
77. Sele, C.W., von Werne, T., Friend, R.H. and Sirringhaus, H., Lithography-free, self-aligned inkjet printing with subhundred-nanometer resolution, *Adv. Mater.*, 17, 997–1001, 2005.
78. Halik, M., Klauk, H., Zschieschang, U., Schmid, G., Dehm, C., Schutz, M., Maisch, S., Effenberger, F., Brunnbauer, M. and Stellacci, F., Low-voltage organic transistors with an amorphous molecular gate dielectric, *Nature*, 431, 963–966, 2004.
79. Yoon, M.-H., Facchetti, A. and Marks, T.J., Molecular dielectric multilayers for low-voltage organic thin film transistors, *Proc. Nat. Acad. Sci.*, 102, 4679, 2005.
80. Park, Y.D., Kim, D.H., Jang, Y., Hwang, M., Lim, J.A. and Cho, K., Low-voltage polymer thin-film transistors with a self-assembled monolayer as the gate dielectric, *Appl. Phys. Lett.*, 87, 2 005.
81. Sakanoue, T., Fujiwara, E., Yamada, R. and Tada, H., Visible light emission from polymer-based field-effect transistors, *Appl. Phys. Lett.*, 84, 3037–3039, 2004.
82. Cicoira, F., Santato, C., Melucci, M., Favaretto, L., Gazzano, M., Muccini, M. and Barbarella, G., Organic light-emitting transistors based on solution-cast and vacuum-sublimed films of a rigid core thiophene oligomer, *Adv. Mater.*, 18, 169–172, 2006.
83. Santato, C., Capelli, R., Loi, M.A., Murgia, M., Cicoira, F., Roy, V.A.L., Stallinga, P., Zamboni, R., Rost, C., Karg, S.E. and Muccini, M., Tetracene-based organic light-emitting transistors: Optoelectronic properties and electron injection mechanism, *Syn. Met.*, 146, 329–334, 2004.
84. Ahles, M., Hepp, A., Schmechel, R. and von Seggern, H., Light emission from a polymer transistor, *Appl. Phys. Lett.*, 84, 428–430, 2004.
85. Rost, C., Karg, S., Riess, W., Loi, M.A., Murgia, M. and Muccini, M., Light-emitting ambipolar organic heterostructure field-effect transistor, *Syn. Met.*, 146, 237–241, 2004.
86. Zaumseil, J., Friend, R.H. and Sirringhaus, H., Spatial control of the recombination zone in an ambipolar light-emitting organic transistor, *Nat. Mater.*, 5, 69–74, 2006.
87. Swensen, J.S., Soci, C. and Heeger, A.J., Light emission from an ambipolar semiconducting polymer field-effect transistor, *Appl. Phys. Lett.*, 87, 2005.
88. van der Horst, J.W., Bobbert, P.A., Michels, M.A.J., Brocks, G. and Kelly, P.J., *Ab initio* calculation of the electronic and optical excitations in polythiophene: Effects of intra- and interchain screening, *Phys. Rev. Lett.*, 83, 4413–4416, 1999.
89. Bredas, J.L., Beljonne, D., Coropceanu, V. and Cornil, J., Charge-transfer and energy-transfer processes in pi-conjugated oligomers and polymers: A molecular picture, *Chem. Rev.*, 104, 4971–5003, 2004.

90. Brown, P.J., Sirringhaus, H., Harrison, M.G. and Friend, R.H., Optical spectroscopy of field-induced charge in self-organized high mobility poly(3-hexylthiophene), *Phys. Rev. B*, 63, 5204–5214, 2001.
91. Deng, Y. and Sirringhaus, H., Optical absorptions of polyfluorene transistors, *Phys. Rev. B*, 72, 045207, 2005.
92. Beljonne, D., Cornil, J., Sirringhaus, H., Brown, P.J., Shkunov, M., Friend, R.H. and Bredas, J.L., Optical signature of delocalized polarons in conjugated polymers, *Adv. Funct. Mater.*, 11, 229, 2001.
93. Osterbacka, R., An, C.P., Jiang, X.M. and Vardeny, Z.V., Two-dimensional electronic excitations in conjugated polymer nanocrystals, *Science*, 287, 839–843, 2000.
94. Marcus, R.A., Exchange reactions and electron transfer reactions including isotopic exchange. Theory of oxidation-reduction reactions involving electron transfer. Part 4 — A statistical-mechanical basis for treating contributions from solvent, ligands, and inert salt, *Discuss. Faraday Soc.*, 29, 21, 1960.
95. Bäessler, H., Charge transport in disordered organic photoconductors — A Monte Carlo simulation study, *Phys. Status Solidi B*, 175, 15, 1993.
96. Novikov, S.V., Dunlap, D.H., Kenkre, V.M., Parris, P.E. and Vannikov, A.V., Essential role of correlations in governing charge transport in disordered organic materials, *Phys. Rev. Lett.*, 81, 4472–4475, 1998.
97. Vissenberg, M.C.J.M. and Matters, M., Theory of the field-effect mobility in amorphous organic transistors, *Phys. Rev. B*, 57, 12964–12967, 1998.
98. Tanase, C., Meijer, E.J., Blom, P.W.M. and de Leeuw, D.M., Unification of the hole transport in polymeric field-effect transistors and light-emitting diodes, *Phys. Rev. Lett.*, 91, 216601, 2003.
99. Pasveer, W.F., Cottaar, J., Tanase, C., Coehoorn, R., Bobbert, P.A., Blom, P.W.M., de Leeuw, D.M. and Michels, M.A.J., Unified description of charge-carrier mobilities in disordered semiconducting polymers, *Phys. Rev. Lett.*, 94, 2005.
100. Shaked, S., Tal, S., Roichman, Y., Razin, A., Xiao, S., Eichen, Y. and Tessler, N., Charge density and film morphology dependence of charge mobility in polymer field-effect transistors, *Adv. Mater.*, 15, 913–917, 2003.
101. Salleo, A., Chen, T.W., Volkel, A.R., Wu, Y., Liu, P., Ong, B.S. and Street, R.A., Intrinsic hole mobility and trapping in a regioregular poly(thiophene), *Phys. Rev. B*, 70, art. no. 115311, 2004.
102. Street, R.A., Northrup, J.E. and Salleo, A., Transport in polycrystalline polymer thin-film transistors, *Phys. Rev. B*, 71, 2005.
103. Beljonne, D., Cornil, J., Sirringhaus, H., Brown, P.J., Shkunov, M., Friend, R.H. and Bredas, J.L., Optical signature of delocalized polarons in conjugated polymers, *Adv. Funct. Mater.*, 11, 229–234, 2001.
104. Tengstedt, C., Osikowicz, W., Salaneck, W.R., Parker, I.D., Hsu, C.H. and Fahlmann, M., Fermi-level pinning at conjugated polymer interfaces, *Appl. Phys. Lett.*, 88, 053502, 2006.
105. Pesavento, P.V., Chesterfield, R.J., Newman, C.R. and Frisbie, C.D., Gated four-probe measurements on pentacene thin-film transistors: Contact resistance as a function of gate voltage and temperature, *J. Appl. Phys.*, 96, 7312–7324, 2004.
106. Facchetti, A., Mushrush, M., Katz, H.E. and Marks, T.J., *n*-Type building blocks for organic electronics: A homologous family of fluorocarbon-substituted thiophene oligomers with high carrier mobility, *Adv. Mater.*, 15, 33–37, 2003.
107. Burgi, L., Richards, T.J., Friend, R.H. and Sirringhaus, H., Close look at charge carrier injection in polymer field-effect transistors, *J. Appl. Phys.*, 94, 6129–6137, 2003.

108. Puntambekar, K.P., Pesavento, P.V. and Frisbie, C.D., Surface potential profiling and contact resistance measurements on operating pentacene thin-film transistors by Kelvin probe force microscopy, *Appl. Phys. Lett.*, 83, 5539–5541, 2003.
109. Nichols, J.A., Gundlach, D.J. and Jackson, T.N., Potential imaging of pentacene organic thin-film transistors, *Appl. Phys. Lett.*, 83, 2366–2368, 2003.
110. Scott, J.C. and Malliaras, G.G., Charge injection and recombination at the metal–organic interface, *Chem. Phys. Lett.*, 299, 115–119, 1999.
111. Hamadani, B.H. and Natelson, D., Nonlinear charge injection in organic field-effect transistors, *J. Appl. Phys.*, 97, 2005.
112. Kanicki, J. In: *Thin film transistors*, ed. P.A.C.R. Kagan, Marcel Dekker, New York, 2003.
113. Matters, M., de Leeuw, D.M., Herwig, P.T. and Brown, A.R., Bias-stress induced instability of organic thin film transistors, *Syn. Met.*, 102, 998–999, 1999.
114. Street, R.A., Salleo, A. and Chabinyk, M.L., Bipolaron mechanism for bias-stress effects in polymer transistors, *Phys. Rev. B*, 68, art. no. 085316, 2003.
115. Schmechel, R. and von Seggern, H., Electronic traps in organic transport layers, *Phys. Status Solidi A — Appl. Res.*, 201, 1215–1235, 2004.
116. Lindner, T., Paasch, G. and Scheinert, S., Influence of distributed trap states on the characteristics of top and bottom contact organic field-effect transistors, *J. Mater. Res.*, 19, 2014–2027, 2004.
117. Salleo, A. and Street, R.A., Kinetics of bias stress and bipolaron formation in polythiophene, *Phys. Rev. B*, 70, art. no. 235324, 2004.
118. Salleo, A., Endicott, F. and Street, R.A., Reversible and irreversible trapping at room temperature in poly(thiophene) thin-film transistors, *Appl. Phys. Lett.*, 86, 2005.
119. Salleo, A. and Street, R.A., Light-induced bias stress reversal in polyfluorene thin-film transistors, *J. Appl. Phys.*, 94, 4231–4231, 2003.
120. Burgi, L., Richards, T., Chiesa, M., Friend, R.H. and Sirringhaus, H., A microscopic view of charge transport in polymer transistors, *Syn. Met.*, 146, 297–309, 2004.
121. Zilker, S.J., Detcheverry, C., Cantatore, E. and de Leeuw, D.M., Bias stress in organic thin-film transistors and logic gates, *Appl. Phys. Lett.*, 79, 1124–1126, 2001.
122. Rep, D.B.A., Morpurgo, A.F., Sloof, W.G. and Klapwijk, T.M., Mobile ionic impurities in organic semiconductors, *J. Appl. Phys.*, 93, 2082–2090, 2003.
123. Gomes, H.L., Stallinga, P., Colle, M., de Leeuw, D.M. and Biscarini, F., Electrical instabilities in organic semiconductors caused by trapped supercooled water, *Appl. Phys. Lett.*, 88, 2006.





2.4 Contact Effects in Organic Field-Effect Transistors

Matthew J. Panzer and C. Daniel Frisbie

CONTENTS

2.4.1	Introduction	139
2.4.2	Definition of an Ohmic Contact	140
2.4.3	Origins of Contact Resistance	140
2.4.3.1	Electronic Structure and Potential Barriers at Metal–Organic Interfaces	140
2.4.3.2	Charge Transport across Metal–Organic Interfaces	143
2.4.3.3	Influence of Channel Dimensions	144
2.4.3.4	Influence of Device Architecture	146
2.4.4	Measuring Contact Resistance.....	148
2.4.4.1	Extrapolation of Device Resistance to Zero Channel Length.....	148
2.4.4.2	Gated Four-Probe Measurements.....	149
2.4.4.3	Kelvin Probe Force Microscopy	150
2.4.4.4	Measured Contact Resistance Values.....	151
2.4.5	Contact Engineering	153
2.4.5.1	Chemical Modifications	153
2.4.5.2	Ambipolar and Light-Emitting OFETs.....	154
2.4.5.3	Channel Dimensions: How Small?.....	154
	References.....	155

2.4.1 INTRODUCTION

In an ideal organic field-effect transistor (OFET), the source and drain contacts are ohmic, meaning the value of the contact resistance is negligibly small in comparison with the electrical resistance of the semiconductor (i.e., the channel resistance). While this situation can be achieved in real devices, there are several practical considerations for fabricating OFETs that are not contact limited [1]. In this chapter, we begin by defining an ohmic contact and continue with a discussion of the origins of contact resistance. Subsequent sections cover techniques used to quantify contact



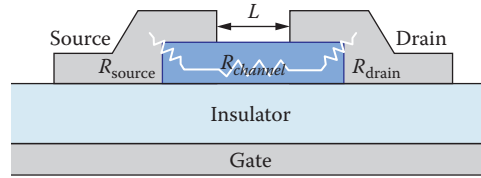


FIGURE 2.4.1

resistance in working OFETs, along with tables of contact resistance values for common OFET geometries based on typical organic semiconductors. We conclude with comments on contact engineering to improve OFET performance.

2.4.2 DEFINITION OF AN OHMIC CONTACT

In traversing an OFET channel from source to drain, charge carriers are (1) injected from the source contact into the semiconductor channel; (2) transported across the length of the channel; and (3) extracted from the channel into the drain. These processes can be roughly thought of as three resistors in series (Figure 2.4.1). The resistances associated with carrier injection and collection steps can be grouped into the *contact resistance* (R_c), while the resistance associated with crossing the channel length in the semiconductor is termed the *channel resistance* ($R_{channel}$). Keeping the contact resistance small compared to the channel resistance is crucial to the realization of “ohmic contacts” in OFETs (i.e., for an ohmic contact, $R_c \ll R_{channel}$).

If the contacts are ohmic, then they are not bottlenecks to current flow and they can source and sink all the current that can be transported by the channel under the given bias conditions. Importantly, nominally high-resistance contacts can still be ohmic as long as they are able to source or sink the current driven through an even more resistive channel. This definition also implies that contacts that function ohmically for a given channel length may in fact no longer be ohmic as the channel length shrinks. This is because $R_{channel}$ scales proportionally with length, so making smaller OFETs results in smaller channel resistances and puts a smaller upper bound on the acceptable value of contact resistance. An additional issue in FETs is that the channel resistance is continuously lowered with increasing gate voltage, and thus contact resistances must be low compared to the channel resistance at high gate voltage in order to be considered ohmic.

A key factor in determining contact resistance is the electronic structure or band lineup at the metal–organic interface. We will see later that contact resistance is also a function of contact geometry and fabrication procedures.

2.4.3 ORIGINS OF CONTACT RESISTANCE

2.4.3.1 ELECTRONIC STRUCTURE AND POTENTIAL BARRIERS AT METAL–ORGANIC INTERFACES

From conventional semiconductor electronics, it is known that creating a low-resistance ohmic contact requires alignment of the metal Fermi level (E_F) with the

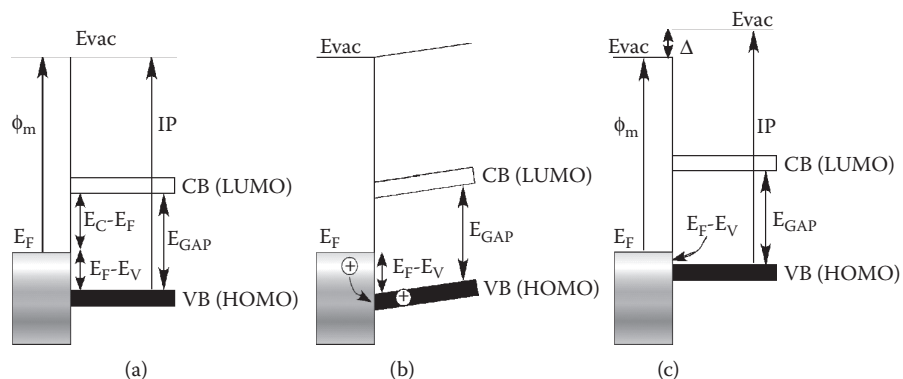


FIGURE 2.4.2

energy levels (bands) of the semiconductor. Figure 2.4.2(a) shows a simple diagram depicting energy level alignments at a metal–organic semiconductor junction. This diagram assumes that the Mott–Schottky rule holds: namely, that the vacuum levels of the metal and organic semiconductors are in registry. The outcome of this assumption is that one can easily estimate the conduction band and valence band offsets from the Fermi level. For example, the valence band offset, $E_F - E_V$, is the difference between the work function of the metal (ϕ_m) and the ionization potential (IP) of the organic semiconductor, or

$$E_F - E_V = \phi_m - IP. \quad (2.4.1)$$

This offset is in turn a good estimate of the potential barrier to hole injection from the metal to the semiconductor. As shown in Figure 2.4.2(b), applying a positive bias to the metal relative to the semiconductor can result in hole injection (so-called thermionic emission) into the valence band if the holes can surmount the barrier $E_F - E_V$. A similar discussion holds for electron injection into the conduction band, but in that case the metal is biased negative and the barrier is determined by $E_C - E_F$. Thus, the electronic structure of metal–organic semiconductor interfaces plays a crucial role in determining the charge transport characteristics of the contact.

In reality, however, many metal–organic semiconductor interfaces do not follow the Mott–Schottky rule and the electronic structure is significantly more complicated than depicted in Figure 2.4.2(a) [2]. Often, an interface dipole is present that shifts the vacuum level of the semiconductor with respect to the metal, as shown in Figure 2.4.2(c). Interface dipoles have several possible origins, including charge transfer between the semiconductor molecules and the metal, reduction of the metal work function by adsorption of the organic layer (even absorption of a noble gas on a metal modifies the metal work function by pushing back the metal surface electrons), and population of metal-induced mid-gap states (new energy levels) at the interface. Sometimes, simple chemical notions (e.g., high or low electron affinities) can be used to predict the sign of the dipole (i.e., whether it points to the metal or to the semiconductor), but it is a difficult computational problem to predict its magnitude.

The magnitude of the potential change due to the dipole (Δ) must be included in the calculation of the valence band offset,

$$E_F - E_V = \phi_m - IP \pm \Delta, \quad (2.4.2)$$

where the mathematical sign in front of Δ is chosen to reflect the direction of the interfacial dipole.

Currently, the only way to be sure of the magnitude of Δ and thus of the energy level offsets is to measure them. Most of our quantitative knowledge of electronic structure of metal–organic interfaces comes from ultraviolet photoemission spectroscopy (UPS) and inverse photoemission spectroscopy (IPES), which probe filled and empty electronic states, respectively. These techniques allow measurement of valence band and conduction band (HOMO and LUMO) positions with respect to the metal Fermi level and the presence of any interfacial dipoles. Several research groups worldwide have undertaken measurements of the electronic structure of a variety of metal–organic semiconductor combinations; work in this area is still ongoing and current understanding is consequently somewhat fluid, though great progress has been made [3–6].

Figure 2.4.3 shows the band line-up diagram for the gold–pentacene interface determined by UPS and IPES measurements. As has been discussed elsewhere, pentacene is a widely used *p*-channel (hole-conducting) organic semiconductor and gold is generally used to make ohmic contacts in pentacene OFETs [7]. The diagram shows a strong dipole at the interface pointed toward the gold (shifting up the gold vacuum level). In addition, there is a surprising 0.5 eV barrier for hole injection at this contact ($E_F - E_V = 0.47$ eV) [8]. Such a large barrier does not seem consistent with low contact resistance. However, as we will point out in the next subsection, the nature of real metal–organic interfaces is complicated and the transport properties

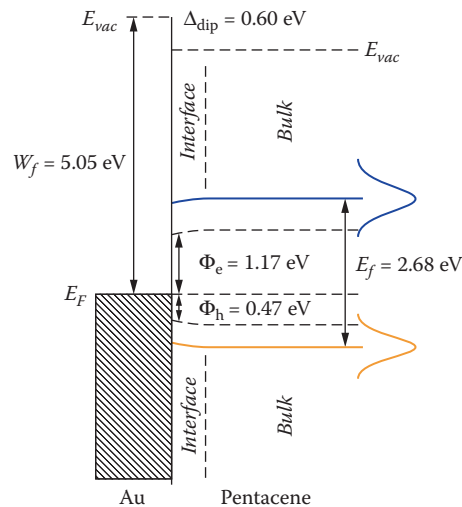


FIGURE 2.4.3

of the source and drain contacts are only partially determined by the presence of potential barriers; other factors, such as structural disorder near the contact, also play a role.

One final point concerning interfacial electronic structure is that it has been found that slightly contaminated surfaces can sometimes lead to better charge injection properties [9]. The reasoning is that the contamination layer (either adventitious adsorbates or intentionally deposited interlayers) can prevent interactions between the organic semiconductor and the metal that produce unfavorable dipoles or that tend to pin the Fermi level in the gap. For example, it has been found that gold electrodes coated with a thin layer of the organic metal PEDOT:PSS are better hole injectors into polythiophene than bare-gold electrodes, even though PEDOT:PSS has a lower work function than gold.

2.4.3.2 CHARGE TRANSPORT ACROSS METAL–ORGANIC INTERFACES

Despite the fact that significant potential barriers (>0.3 eV) exist at many metal–organic semiconductor interfaces, it is possible to make ohmic source and drain contacts in OFETs. A likely reason for this is that the charge injection mechanism is probably not simple thermionic emission in which carriers must surmount the full potential barrier, as originally indicated in Figure 2.4.2(b). Instead, at large interfacial electric field strength, field emission (tunneling) through the barrier can become possible; this is a process that effectively lowers the potential barrier. Another possible injection mechanism involves defect-assisted transport in which carriers bypass the barrier by hopping through midgap states. Figure 2.4.4 shows a simple comparison of these different charge injection mechanisms.

There is mounting experimental evidence that the charge injection process at the source electrode in OFETs is not simple thermionic emission [10–13]. First, measurements of the source contact resistance as a function of temperature reveal that the injection process is indeed thermally activated (which is consistent

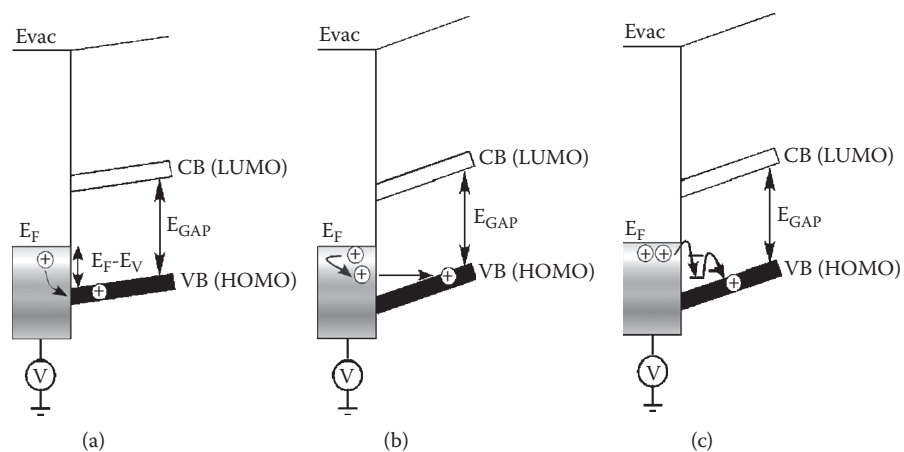


FIGURE 2.4.4

with thermionic emission), but the activation energies are generally much smaller than the estimated potential barriers determined by photoemission spectroscopy. In some cases, the activation energy associated with the source contact resistance is very comparable to the activation energy associated with the carrier field effect mobility, suggesting that transport of charge in the semiconductor near the contact is the limiting bottleneck, not the actual metal-to-semiconductor emission process.

Second, channel potential measurements by Kelvin probe force microscopy and the four-probe method, which are described later in this chapter, indicate that the contact resistances and temperature dependences associated with the individual source and drain electrodes are nearly identical. From a thermionic emission viewpoint, one would expect the resistance at the source electrode (the injecting contact) to be much larger than the resistance at the drain (the collecting contact). The fact that the source and drain contact resistance behaviors are very similar in most devices also indicates that the bottleneck at the contacts is related to charge transport in the (disordered) organic semiconductor near the contacts and not simply due to an injection barrier at the metal–organic interface.

An additional point is that, in general, the source and drain contact resistances are gate voltage dependent; specifically, they decrease with increasing gate voltage. The variation of the contact resistance with gate voltage is essentially identical for both the source and drain and it is also similar to the variation of the channel resistance. The close tracking of the gate voltage dependence on the source, drain, and channel resistances also indicates that contact resistance depends on film transport properties near the contact.

The simplest picture that can explain these collective observations is that the source contact resistance is the sum of (1) resistance arising from charge injection over or through the potential barrier; and (2) resistance due to transport in the disordered depletion region near the contact. The drain resistance would simply be due to the latter part. Perhaps because the presence of a strong gate field facilitates field emission through the barrier, resistance (1) is often not limiting for the source; instead, resistance (2) dominates, and thus the source and drain resistances are comparable. This description provides a useful physical picture, but quantitative modeling of the injection and collection processes is complicated by details of the device geometry and the fabrication process, such as the evaporation of hot metal onto the organic semiconductor, which might produce many defects. Work on detailed understanding of transport at OFET contacts is ongoing.

2.4.3.3 INFLUENCE OF CHANNEL DIMENSIONS

As mentioned earlier, channel dimensions are also critical in determining the importance of contact effects in OFETs. Figure 2.4.5 shows the top view of a typical OFET with channel length (L) and channel width (W). It is useful for comparison purposes to report the normalized or specific contact resistance (R_c') as a “raw” resistance value multiplied by the width (W) of the channel. Thus, the units of R_c' are Ωcm . Physically, the reciprocal of this value is the contact conductance per unit width of contact.

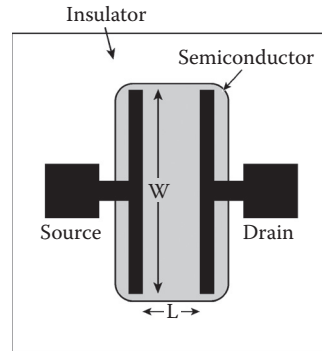


FIGURE 2.4.5

The total device resistance can be expressed as

$$R_{TOT} = R_{channel} + R_c \quad (2.4.3)$$

In terms of the channel sheet resistance (r_s , units of Ω/square , and V_G dependent) and the specific contact resistance (R_c' , units of Ωcm and also V_G dependent), this equation becomes:

$$R_{TOT} = r_s \frac{L}{W} + 2R_c' \quad (2.4.4)$$

This equation facilitates understanding of how the channel dimensions (L and W) affect the relative magnitudes of the contact resistance and the channel resistance. Note that the channel resistance scales as L/W but the contact resistance scales as $1/W$; it does not depend on L . Consider two different OFET devices on the same semiconductor/insulator/gate substrate: both have the same channel width (equal W), but the length of the channel of the second device is 10 times smaller than that of the first ($L_2 = L_1/10$), as depicted in Figure 2.4.6(a). Both devices have equal contact resistances R_c because W is the same. But because the channel resistance scales with L/W (the source-drain current scales with W/L), the channel resistance of the second device is 10 times smaller than that of the first device. This means that contact resistance is potentially much more important in the shorter channel device because it contributes a larger fraction of the total resistance.

A second hypothetical pair of OFET devices is shown in Figure 2.4.6(b). In this case, both contact patterns share the same W/L ratio, but both W and L are twice as large for the second device of this duo. While the channel resistances are now equivalent, the contact resistance of the larger device is half that of the smaller one. The larger device in this case is less likely to be contact limited. In general, one must pay attention to the magnitude of the contact resistance when scaling OFETs to very small lengths (L) because the contact resistance of short-channel devices can quickly become the dominating resistance. As a final note, to avoid nonidealities in transistor output curves, W/L should always be ≥ 10 in order to avoid fringing field effects at the edges of the channel.

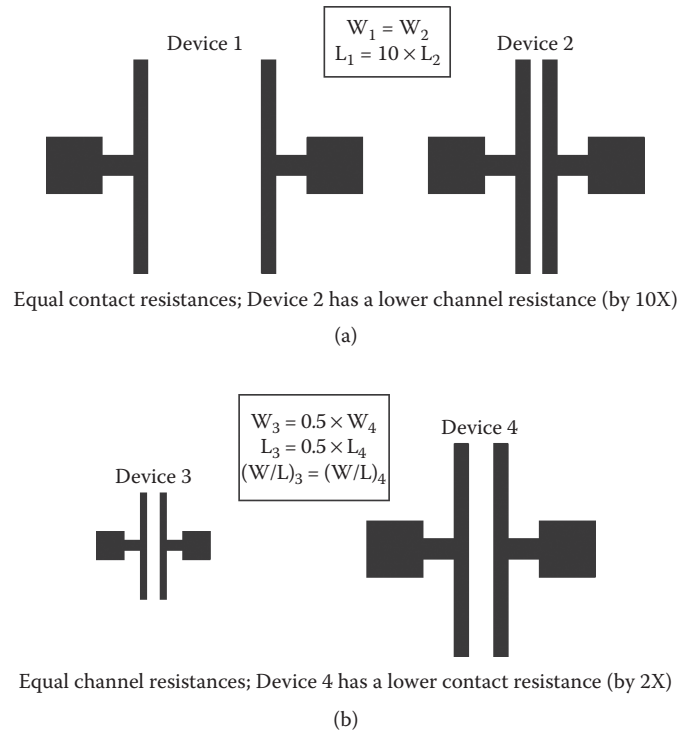


FIGURE 2.4.6

2.4.3.4 INFLUENCE OF DEVICE ARCHITECTURE

There are two main architectures to choose from in OFET fabrication: the *top contact* (or *staggered*) and the *bottom contact* (or *coplanar*) configurations. The physical difference between the two is the order of fabrication steps. That is, the source/drain contacts are either deposited before or after the semiconductor layer is deposited to create a bottom contact or top contact device, respectively. One can also build the entire transistor on top of the semiconductor layer (the so-called top gate architectures), in which the insulator and gate contact are sequentially deposited on top of either of the two contact configurations. All four of these OFET architectures are shown schematically in Figure 2.4.7.

Top contact OFETs (Figure 2.4.7a) generally exhibit the lowest contact resistances. This is likely because of the increased metal–semiconductor contact area in this configuration. A major contribution to contact resistance in the top contact configuration is *access resistance* (see Figure 2.4.8a). Access resistance results from the requirement that charge carriers must travel from the source contact on top of the film down to the accumulation layer (the channel) at the semiconductor–insulator interface and then back up to the drain contact to be extracted.

In order to minimize access resistance, the thickness of the organic semiconductor layer should not be too large. However, some researchers have proposed that

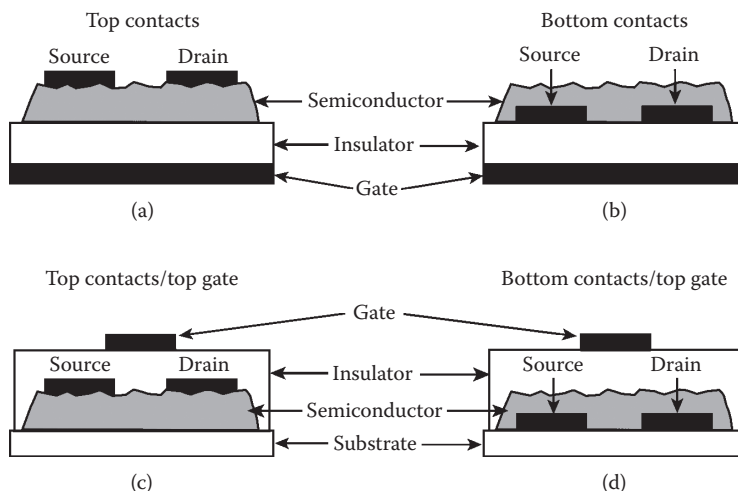


FIGURE 2.4.7

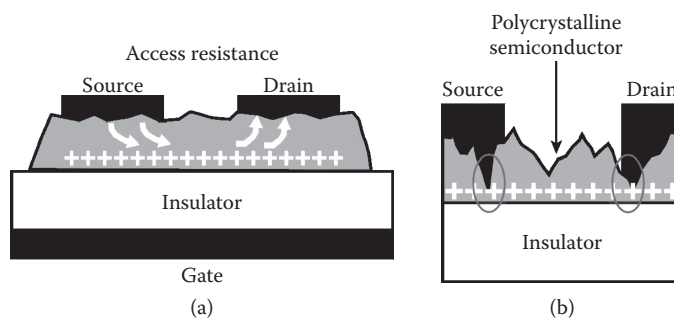


FIGURE 2.4.8

access resistance is less than might be expected for top contact OFETs because the contact metal penetrates the film down to the accumulation layer (perhaps due to large peak-to-valley roughness of the semiconductor film or the nature of the metal deposition process) [11]. This scenario is shown in Figure 2.4.8(b).

With the bottom contact architecture (Figure 2.4.7b), access resistance is not an issue because the contacts are in the same plane as the OFET channel. In addition, very small channel dimensions ($W, L < 10 \mu\text{m}$) can be prepatterned on the insulator using conventional photolithography. A limitation to the bottom contact configuration, however, is that film morphology in the vicinity of the contacts is often nonideal. A number of researchers have demonstrated that the organic semiconductor grain sizes are very small near the contacts, presumably due to heterogeneous nucleation phenomena [14]. Pentacene molecules, for example, prefer to “stand up” with the long axis of the molecule perpendicular to the plane of the substrate when deposited on the commonly used insulator SiO_2 [15]. When deposited on top of gold contacts,

however, strong interactions between the pentacene π -clouds and the metal surface lead to tiny grains at the contact and, in some cases, voids are observed [14]. Semiconductor growth at the complex triple interface (contact-semiconductor-insulator) is not very well understood, although it is clear that the bottom contact configuration almost always creates greater contact resistance than in the case of top contacts.

Of the two top-gate OFET architectures (Figure 2.4.7c and 2.4.7d), the top contact/top gate configuration (Figure 2.4.7c) is the more favorable of the two because bottom contact/top gate devices suffer from access resistance. However, it should be noted that both top gate architectures face the additional concerns of semiconductor top surface roughness (since this is where the channel will form) and forming a stable interface between the insulator and the top of the semiconductor film. Solution deposition of the top insulator material, for example, may damage the underlying semiconductor film. Finally, regarding the alignment of the top gate contact to the OFET channel in top gate devices, care must also be taken to ensure that the gate reaches completely across the entire length (L) of the device. If the length of the gate electrode is less than the channel length or if the gate is simply misaligned, additional contact resistance will be introduced as a result of ungated semiconductor regions at one or both of the contacts.

2.4.4 MEASURING CONTACT RESISTANCE

2.4.4.1 EXTRAPOLATION OF DEVICE RESISTANCE TO ZERO CHANNEL LENGTH

Since the total resistance a charge carrier experiences during its journey from source to drain (i.e., V_D/I_D) is the sum of the contact resistance and the channel resistance as discussed earlier, one of the simplest ways to quantitatively measure OFET contact resistance involves isolating these two resistances by extrapolation. By fabricating several pairs of source and drain contacts with different channel lengths (but constant W) on the same semiconductor film, one measures the total OFET resistance and makes a plot of resistance versus channel length. Linear extrapolation of the plot to $L = 0$ effectively eliminates the channel resistance and yields the contact resistance as the y-intercept. This method of measuring contact resistance is known as the *transmission line method* or R vs. L technique. Figure 2.4.9 shows an example of a resistance ($R_{TOT}W$) versus channel length plot with extrapolation used to determine the specific contact resistance, R_c' .

Because both the channel and contact resistances are affected by the charge density in the channel, the resistance measurements are made at a single gate voltage (usually in the linear operation regime). The drain voltage could also be scaled to L in order to obtain the same source-to-drain lateral electric field for each device. While this technique is straightforward to perform and understand, it has two disadvantages. First, it can be tedious to fabricate and test several devices in order to obtain the resistance versus channel length plot. In addition, the contact resistance obtained by the transmission line technique lumps the individual source and drain resistances together.

Contact Effects in Organic Field-Effect Transistors

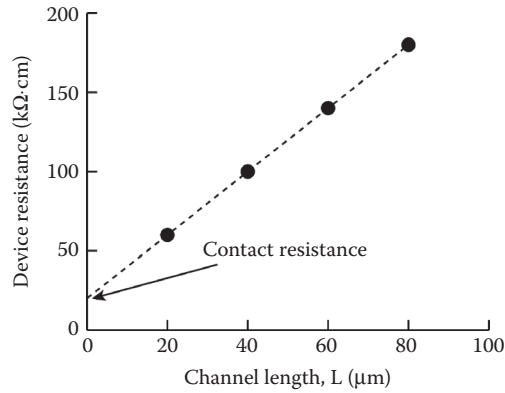


FIGURE 2.4.9

2.4.4.2 GATED FOUR-PROBE MEASUREMENTS

In order to separate the individual contributions of the source and drain contacts to the total contact resistance, a more sophisticated measurement technique is required. The *gated four-probe technique* utilizes two narrow, voltage-sensing electrodes situated between the source and drain electrodes and slightly protruding into the channel, as shown in Figure 2.4.10(a). During the course of normal OFET electrical characterization, these voltage-sensing probes are connected to high-input impedance electrometers that sense the channel potential at the two probe positions (V_1 , V_2) without passing any current. In the linear regime of OFET operation ($V_G \gg V_D$), the channel should be uniform in charge carrier density with a linear drop in electrostatic potential along L from source to drain. Therefore, any drops in electrostatic potential that occur at the contacts (due to contact resistance) will be manifested upon extrapolation of the channel potential profile based on the voltage-sensing probe measurements.

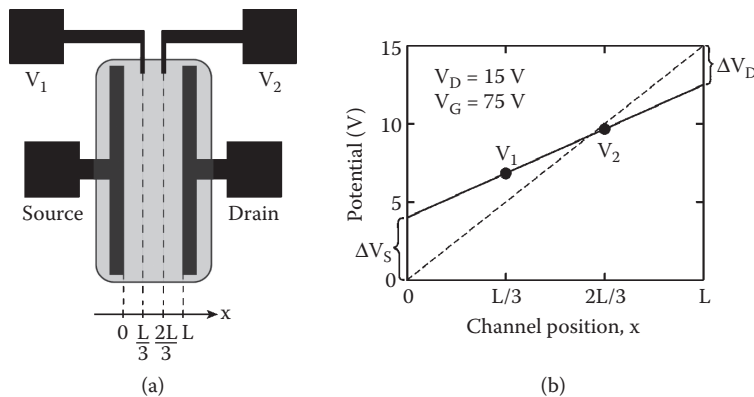


FIGURE 2.4.10

As depicted in Figure 2.4.10(b), contact resistance at the source and drain electrodes results in a smaller than expected slope of the potential versus channel position profile. The profile is estimated by linear extrapolation between V_1 and V_2 . Individual source and drain contact resistances are calculated by dividing the voltage drops ΔV_S and ΔV_D by the source-drain current, respectively. By isolating the source and drain contact contributions to the total contact resistance, the gated four-probe technique provides more information than the transmission line technique, and it is possible to determine R_c in one device (vs. several). An important caveat for the gated four-probe technique is that the extrapolated channel potential profile will only be valid for strict linear regime OFET operation ($V_G \gg V_D$), where the channel potential profile can be expected to be linear and uniform.

2.4.4.3 KELVIN PROBE FORCE MICROSCOPY

While the previously described techniques both require extrapolation of measured data in order to calculate the contact resistance, *Kelvin probe force microscopy* (KFM, also known as scanning surface potential microscopy or scanning potentiometry) can be used to determine the source and drain contributions to the contact resistance directly. In KFM, a conductive atomic force microscope (AFM) tip is scanned over the operational OFET channel twice. On the first pass, the topography of the device is recorded; then, the tip is lifted a small distance (~ 10 nm) off the device and the second pass retraces the channel topology in the air (or better yet, vacuum) above the sample while the electrostatic potential is recorded (see Figure 2.4.11a). The electrostatic potential data are converted into the OFET surface potential profile by subtracting an appropriate background trace. Thus, KFM measures the full channel potential profile.

Since ΔV_S and ΔV_D are measured directly, calculating the source and drain contributions to the contact resistance can be done without any extrapolation. Figure 2.4.11(b) shows a hypothetical channel potential profile measured by KFM. A clear advantage of KFM over the gated four-probe technique is that the entire channel potential profile is measured experimentally instead of using only two points to extrapolate a linear profile (compare figs. 2.4.10b and 2.4.11b). Thus, other bottle-

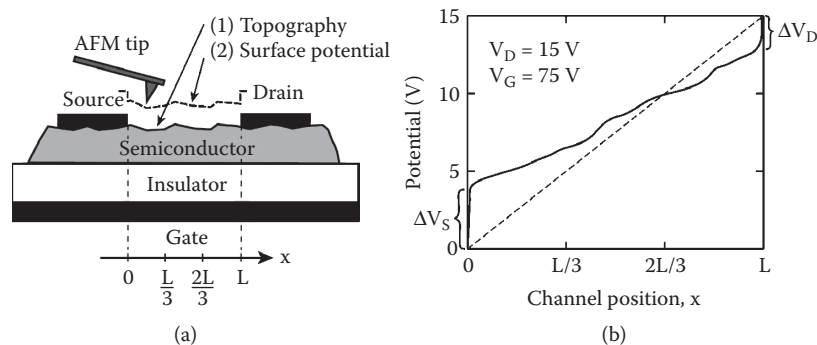


FIGURE 2.4.11

necks to charge transport (e.g., potential drops at grain boundaries in the channel) can also be visualized using this technique.

2.4.4.4 MEASURED CONTACT RESISTANCE VALUES

A collection of experimental OFET contact resistance values is provided in Tables 2.4.1 and 2.4.2. Table 2.4.1 presents contact resistance values for seven different polycrystalline oligomeric semiconductors, including the current benchmark material, pentacene. One must be careful, however, in making comparisons between contact resistance values reported by different groups. It has been proposed that contact resistance is caused by a combination of thermionic emission and carrier diffusion through a depletion region, with the latter dominating in some cases. As a result, contact resistance depends on the level of accumulated charge in the OFET channel, and many experiments have shown that contact resistance is inversely

TABLE 2.4.1
OFET Contact Resistance Values: Evaporated Oligomer Films

Semiconductor	Contact metal	TC/BC ^a	R_C (Ωcm) ^b	Method	Ref.
Linear acenes (p-channel)					
Pentacene	Au	TC	3×10^4	R vs. L	17
	Au	TC	1×10^3	Four probe	11
	Au	TC	$R_S = 3 \times 10^2$ $R_D = 1 \times 10^3$	KFM	19
	Au	BC	$R_S = 4 \times 10^4$ $R_D = 2 \times 10^4$	KFM	19
	Ag	TC	1×10^3	Four probe	11
	Ag	TC	2×10^3	Four probe	16
	Pt	TC	4×10^3	Four probe	11
	Ca	TC	4×10^4	Four probe	11
	Hg _(liq)	TC	$<2 \times 10^4$	R vs. L	20
Perylene diimides (n-channel)					
PTCDI-C ₅	Au	TC	4×10^4	Four probe	21
	Ag	TC	4×10^4	Four probe	21
	Ag	TC	1×10^5	Four probe	22
	Ca	TC	6×10^4	Four probe	21
PTCDI-C ₈	Ag	TC	2×10^4	Four probe	22
PTCDI-C ₁₂	Ag	TC	3×10^4	Four probe	22
PTCDI-C ₁₃	LiF/Al	TC	1×10^5	Four probe	23
Acene-capped bithiophenes (p-channel)					
Ant-2T-Ant	Au	TC	3×10^4	Four probe	24
Tet-2T-Tet	Au	TC	2×10^4	Four probe	24

^a OFET architecture: top contact (TC) or bottom contact (BC).

^b Total (source resistance, R_S + drain resistance, R_D) contact resistance, R_C , unless individual values are shown.

TABLE 2.4.2
OFET Contact Resistance Values: Solution-Deposited Polymers and Oligomers

Semiconductor	Contact metal	TC/BC ^a	R_C (Ωcm) ^b	Method	Ref.
Polymer films (p-channel)					
P3HT	Au	TC	$R_S = 2 \times 10^5$ $R_D = 5 \times 10^4$	Four probe	26
	Au	BC	1×10^4	R vs. L	13
	Au	BC	$\sim 5 \times 10^5$	R vs. L	18
	Au	BC	$R_S < 5 \times 10^3$	KFM	10
	Ag	BC	$R_S = 2 \times 10^4$	KFM	10
	Cr/Au	BC	$R_S = 2 \times 10^4$	KFM	10
	Cu	BC	3×10^6	R vs. L	13
	Cu	BC	$R_S = 3 \times 10^5$	KFM	10
	Cr	BC	1×10^5	R vs. L	13
	Cr	BC	$R_S = 5 \times 10^6$	KFM	10
	F8T2	Au	BC	$R_S = 1 \times 10^7$	KFM
Cr/Au		BC	$R_S > 7 \times 10^7$	KFM	10
Soluble oligomer (n-channel)					
C ₇₀ -PCBM	Au	BC	$\sim 1 \times 10^6$	R vs. L	27

^a OFET architecture: top contact (TC) or bottom contact (BC).

^b Total (source resistance, R_S + drain resistance, R_D) contact resistance, R_C , unless individual values are shown.

proportional to V_G [16,17]. Figure 2.4.12 shows the typical decrease of the source, drain and channel resistances with increasing gate voltage (carrier density) for a pentacene OFET with gold contacts.

Thus, while the contact resistance values summarized in Tables 2.4.1 and 2.4.2 are generally reported at large values of V_G in the linear operating regime, not all of the measurements have been made at the same induced charge density in the channel. Additionally, there has been some evidence that, even with “good” contacts, contact resistance is also inversely proportional to the semiconductor mobility [9,12,17].

Again, it is not necessarily the value of the contact resistance of an OFET that is significant, but rather its value *in comparison to* the channel resistance. In the linear regime, the scaled OFET channel resistance ($R_{channel}\Sigma W$) is given by:

$$(2.4.5)$$

where μ is the semiconductor mobility and Q' is the accumulated charge per unit area in the channel. Inserting typical values for L (100 μm), μ (0.1 cm^2/Vs), and Q' (1 $\mu\text{C}/\text{cm}^2$) yields a channel resistance of $1 \times 10^5 \Omega\text{cm}$, which can be compared to the numbers in the tables.

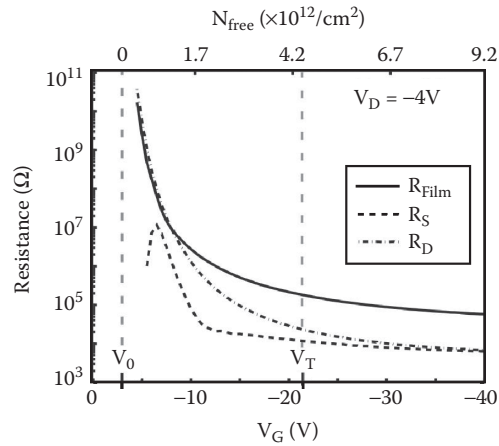


FIGURE 2.4.12

Table 2.4.2 presents a collection of contact resistance values measured for a few solution-deposited polymeric and oligomeric semiconductors. These values tend to be higher than in the case of evaporated oligomeric films due to lower mobilities. It has also been observed that, in certain instances, the source contact can constitute a majority of the total contact resistance in polymeric films [10,25].

2.4.5 CONTACT ENGINEERING

2.4.5.1 CHEMICAL MODIFICATIONS

As discussed previously, the fundamental reason why contact resistance is generally greater for the bottom contact OFET architecture is the poor semiconductor morphology on top of or near the source and drain contacts that hinders charge injection/extraction. Thus, one of the simplest ways to improve the quality of the semiconductor film on top of bottom contacts is to pretreat the contacts chemically before depositing the semiconductor. In the simplest case, one can use thiol-terminated hydrocarbon molecules to form a self-assembled monolayer (SAM) on top of metallic contacts [14]. The affinity of the thiol group for metal surfaces and SAM formation with such molecules have been well-studied. By forming a CH_3 -terminated SAM on top of the contacts, the semiconductor layer will no longer “see” the metal, but rather a hydrophobic surface with a different surface energy. As a result, the semiconductor morphology will be modified on top of the contacts — hopefully, in such a way as to improve charge injection/extraction and reduce contact resistance.

Taking the idea of SAM formation one step further, one can also use molecules with various chemical functionalities (not only hydrocarbons) for pretreating the contacts. SAMs featuring both electron-withdrawing and electron-donating end groups opposite the thiol linking ends have been used to alter the charge injection properties of bottom contact OFETs [28,29]. This strategy has the advantage of tuning the energy band line-up at the contact–semiconductor interface in addition

to improving semiconductor morphology. Although not as common, there have also been attempts to improve the properties of top contacts by depositing chemical moieties through a shadow mask on top of the semiconductor, immediately prior to contact metal deposition [30].

Two additional examples of manipulating the contact chemistry to achieve lower contact resistance are noteworthy. In the case of the nonmetal contact material poly(3,4-ethylenedioxythiophene) doped with poly(styrenesulfonate), PEDOT:PSS, one group found that low contact resistances were achieved between PEDOT:PSS and the polymer semiconductor F8T2 in a bottom contact OFET [31]. It was posited that the PEDOT:PSS contacts had doped the semiconductor in the vicinity of the contacts, leading to more efficient charge injection/extraction. A second group of researchers found a clever way to make better top contacts to the single-crystal charge-transfer semiconductor DBTTF-TCNQ than with either gold or silver. They used the related *metallic* charge-transfer material TTF-TCNQ to form top contacts to the semiconductor with success in realizing more efficient charge injection [32]. These are only a few examples that show how judicious chemical modifications to the contact–semiconductor interface can often be used to improve contact quality in OFETs.

2.4.5.2 AMBIPOLAR AND LIGHT-EMITTING OFETs

While the development of ambipolar (both hole- and electron-transporting) OFETs is still in the early stages, it is certainly an exciting subject within the OFET community. These devices offer not only new possibilities for complementary logic circuit design, but also the potential to control electron–hole recombination within the semiconductor channel to afford light emission. Light-emitting organic field-effect transistors (LEOFETs) are particularly intriguing because they possess charge carrier densities in the channel in the transverse (source-drain) direction that are orders of magnitude higher than those found in organic light-emitting diodes (OLEDs) [33].

While it is simpler from a fabrication standpoint to deposit the same contact material for both the source and drain contacts (*symmetric contacts*), one may also consider choosing two different materials for each contact (*asymmetric contacts*). Based on energy band line-up considerations with the semiconductor HOMO and LUMO levels, depositing two different contact materials at either end of the transistor channel may facilitate more efficient hole and electron injection, respectively. At this point, it is unclear whether separately engineering distinct contacts for hole/electron injection in ambipolar OFETs will prevail over opting for symmetric contacts. However, there will certainly be more reports on this exciting OFET subclass in the next few years.

2.4.5.3 CHANNEL DIMENSIONS: HOW SMALL?

At the laboratory scale, OFET channel lengths are typically on the order of 10–100 μm , with W/L ratios ranging from ~ 10 to over 1,000. Commercialization of organic electronics will lead to a push to make OFET dimensions as small as possible, since

the switching speed (cut-off frequency) of an ideal transistor is inversely proportional to L^2 . As discussed previously, however, one must be careful to avoid becoming contact resistance-limited when shrinking L . For example, from Table 2.4.1, the specific contact resistance for gold top contacts on pentacene can be as low as 1 k Ω -cm. The channel sheet resistance for pentacene devices at high gate voltage ($\sim 5 \times 10^{12}$ carriers/cm 2) is about 1 M Ω /sq, assuming a mobility of 1 cm 2 /Vs. Thus, for a 10- μ m channel length pentacene device, the contact resistance is 50% of the total device resistance in the ON state! Clearly, driving the channel lengths smaller will only exacerbate this problem. Thus, ongoing contact engineering efforts to make lower resistance contacts to organic semiconductors will remain important to OFET development and the advancement of organic electronics.

REFERENCES

1. Shen, Y. et al., How to make ohmic contacts to organic semiconductors, *Chem. Phys. Chem.*, 5, 16, 2004.
2. Kahn, A., Koch, N. and Gao, W., Electronic structure and electrical properties of interfaces between metals and π -conjugated molecular films, *J. Polym. Sci. B: Polym. Phys.*, 41, 2529, 2003.
3. Hill, I.G. et al., Organic semiconductor interfaces: Electronic structure and transport properties, *Appl. Surf. Sci.*, 166, 354, 2000.
4. Seki, K. and Ishii, H., Photoemission studies of functional organic materials and their interfaces. *J. Electron Spectroscopy Related Phenomena*, 88–91, 821, 1998.
5. Salaneck, W.R. and Fahlman, M., Hybrid interfaces of conjugate polymers: Band edge alignment studied by ultraviolet photoelectron spectroscopy, *J. Mater. Res.*, 19, 1917, 2004.
6. Kera, S. et al., Impact of an interface dipole layer on molecular level alignment at an organic-conductor interface studied by ultraviolet photoemission spectroscopy, *Phys. Rev. B*, 70, 085304, 2004.
7. Necliudov, P.V. et al., Contact resistance extraction in pentacene thin film transistors, *Solid-State Electronics*, 47, 259, 2002.
8. Amy, F., Chan, C., and Kahn, A., Polarization at the gold/pentacene interface, *Org. Elec.*, 6, 85, 2005.
9. Wan, A. et al., Impact of electrode contamination on the α -NPD/Au hole injection barrier, *Org. Elec.*, 6, 47, 2005.
10. Pesavento, P.V. et al., Gated four-probe measurements on pentacene thin-film transistors: Contact resistance as a function of gate voltage and temperature, *J. Appl. Phys.*, 96, 7312, 2004.
11. Pesavento, P.V. et al., Film and contact resistance in pentacene thin-film transistors: Dependence on film thickness, electrode geometry, and correlation with hole mobility, *J. Appl. Phys.*, 99, 094504, 2006.
12. Kymissis, I., Dimitrakopoulos, C.D., and Purushothaman, S., High-performance bottom electrode organic thin-film transistors, *IEEE Trans. Elec. Dev.*, 48, 1060, 2001.
13. Dimitrakopoulos, C.D., Brown, A.R., and Pomp, A., Molecular beam deposited thin films of pentacene for organic field effect transistor applications, *J. Appl. Phys.*, 80, 2501, 1996.
14. Newman, C. R. et al., High mobility top-gated pentacene thin-film transistors, *J. Appl. Phys.*, 98, 084506, 2005.

15. Zaumseil, J., Baldwin, K.W., and Rogers, J.A., Contact resistance in organic transistors that use source and drain electrodes formed by soft contact lamination, *J. Appl. Phys.*, 93, 6117, 2003.
16. Meijer, E.J. et al., Scaling behavior and parasitic series resistance in disordered organic field-effect transistors, *Appl. Phys. Lett.*, 82, 4576, 2003.
17. Puntambekar, K.P., Pesavento, P.V., and Frisbie, C.D., Surface potential profiling and contact resistance measurements on operating pentacene thin-film transistors by Kelvin probe force microscopy, *Appl. Phys. Lett.*, 83, 5539, 2003.
18. Maltezos, G. et al., Tunable organic transistors that use microfluidic source and drain electrodes, *Appl. Phys. Lett.*, 83, 2067, 2003.
19. Chesterfield, R.J. et al., Variable temperature film and contact resistance measurements on operating n-channel organic thin film transistors, *J. Appl. Phys.*, 95, 6396, 2004.
20. Chesterfield, R.J. et al., Organic thin film transistors based on n-alkyl perylene diimides: Charge transport kinetics as a function of gate voltage and temperature, *J. Phys. Chem. B*, 108, 19281, 2004.
21. Gundlach, D.J. et al., High mobility n-channel organic thin-film transistors and complementary inverters, *J. Appl. Phys.*, 98, 064502, 2005.
22. Merlo, J.A. et al., P-channel organic semiconductors based on hybrid acene-thiophene molecules for thin-film transistor applications, *J. Am. Chem. Soc.*, 127, 3997, 2005.
23. Street, R.A. and Salleo, A., Contact effects in polymer transistors, *Appl. Phys. Lett.*, 81, 2887, 2002.
24. Panzer, M.J. and Frisbie, C.D., Unpublished results.
25. Anthopoulos, T.D. et al., Solution processible organic transistors and circuits based on a C₇₀ methanofullerene, *J. Appl. Phys.*, 98, 054503, 2005.
26. Campbell, I.H. et al., Controlling Schottky energy barriers in organic electronic devices using self-assembled monolayers, *Phys. Rev. B*, 54, 14321, 1996.
27. Gundlach, D.J., Jia, L., and Jackson, T.N., Pentacene TFT with improved linear region characteristics using chemically modified source and drain electrodes, *IEEE Elec. Dev. Lett.*, 22, 571, 2001.
28. Schroeder, R., Majewski, L.A., and Grell, M., Improving organic transistor performance with Schottky contacts, *Appl. Phys. Lett.*, 84, 1004, 2004.
29. Wang, J.Z., Chang, J.F., and Sirringhaus, H., Contact effects of solution-processed polymer electrodes: Limited conductivity and interfacial doping, *Appl. Phys. Lett.*, 87, 083503, 2005.
30. Takahashi, Y. et al., Tuning of electron injections for n-type organic transistor based on charge-transfer compounds, *Appl. Phys. Lett.*, 86, 063504, 2005.
31. Zaumseil, J., Friend, R.H., and Sirringhaus, H., Spatial control of the recombination zone in an ambipolar light-emitting organic transistor, *Nat. Mater.*, 5, 69, 2006.